Order Number 9432334

Thermocapillary migration of fluid particles in tubes

Chen, Jinnan, Ph.D.

City University of New York, 1994

U·M·I
300 N. Zeeb Rd.
Ann Arbor, MI 48106

A

THERMOCAPILLARY MIGRATION OF FLUID PARTICLES IN TUBES

by

Jinnan Chen

A Dissertation Submitted to the Graduate Faculty in Engineering
in Partial Fulfillment of the Requirements for the Degree of
Doctor of Philosophy, ***THE CITY UNIVERSITY OF NEW YORK***

1994

This manuscript has been read and accepted for the Graduate Faculty in Engineering in satisfaction of the dissertation requirement for the degree of Doctor of Philosophy.

2/4/94
Date

Professor Charles Maldarelli
Chair of Examining Committee

2/4/94
Date

Professor Gerard G. Lowen
Executive Officer

Prof. Charles maldarelli, Chairman

Prof. Zeev Dagan, Co-Chairma

Prof. Peter Ganatos

Prof. David Rumschitzki

Prof. Dimitri Papageorgiou
Department of Mathematics
New Jersey Institute of Technology
Supervisory Committee

The City University of New York

ABSTRACT

THERMOCAPILLARY MIGRATION OF FLUID PARTICLES IN TUBES

by

Jinnan Chen

Adviser: Professor Charles maldarelli (Mentor)

Professor Zeev Dagan (Co-Mentor)

This thesis studies the axial, thermocapillary-driven migration of fluid particles (drops and bubbles) through a continuous and otherwise quiescent liquid phase which fills a cylindrical tube. The hydrodynamic flows accompanying the thermocapillary migrations studied in this thesis are axisymmetric and creeping; the heat transfer is conductive with the tube wall insulated and the surface tension is expanded linearly in the temperature. Compact particles are examined, i.e. ones for which the equivalent spherical radius a' is smaller than the tube radius, b'. Numerical solutions of the hydrodynamic and conduction equations are obtained in order to determine the ratio of the quasisteady velocity in the tube (U'), relative to that in an infinite medium ($U_o^{'}$). The relative velocity is obtained as a function of a'/b', the conductivity (k) and viscosity (κ) ratio of the particle to the suspending phase, and the capillary number Ca ($=\mu'^{(2)} U_o^{'} / \sigma'$, where σ' is the surface tension and $\mu'^{(2)}$ is the suspending phase viscosity).

In the case of dominant interfacial tension forces (Ca=0) for which the drop translates as a sphere, solutions using a collocation technique indicate that for a fixed ratio of a'/b', as k decreases, a greater proportion of energy is conducted through the gap between the insulated tube wall and the particle. This conduction pattern creates a larger surface temperature gradient, and causes the relative migration velocity to increase. The enhancement in migration for decreasing k becomes more pronounced as a'/b' increases and the surface gradient intensifies. However, as the gap distance between the sphere and the tube decreases, hydrodynamic retarding forces develop, and these forces are overriding in the sense that the migration velocity in the tube never exceeds the value in an infinite medium.

In the case of deformable compact particles, capillary numbers must be restricted to values smaller($Ca \neq 0$) than one to be consistent with the assumption that the tension is expanded linearly in the temperature. Calculations, by a boundary integral technique, for Ca=0.05 and κ=1, k=0 and k=1 demonstrate that for $a'/b' \leq 0.8$. the particle is squeezed into the tube center by the hydrodynamic force due to the flow. This deformation reduces the hydrodynamic interaction of the particle with the wall causing an increase in the velocity.

ACKNOWLEDGEMENTS

I would like to thank Professor Charles Maldarelli and Professor Zeev Dagan for their continuous guidance and many contributions in directing this research. I would also like to express my gratitude to all the members of the Supervisory Committee for their help and encouragement.

Special thanks are due to Professor C. Pozrikidis for his help and good advice on my second problem.

Finally, I would like to thank my parents & my daughter for their sacrifices and my support. They have been a constant source of encouragement.

This research was supported in part by a grant from the Department of Energy, Office of Basic Energy Sciences (No. DE-FG02-88ER13820) and a grant from the National Science Foundation (No. 8404261). Their support is gratefully acknowledged.

TABLE OF CONTENTS

LIST OF TABLES

Chapter III

Chapter IV

LIST OF FIGURES

Chapter IV

Chapter I

INTRODUCTION

In this thesis, we study the hydrodynamic movement of gas bubbles and fluid droplets through a continuous liquid phase which are driven by a surface tension difference created on the fluid particle surface by subjecting the continuous phase to a temperature gradient. This type of motion is referred to as thermocapillary migration, and Fig.1 illustrates the fluid mechanics which underlies thermocapillary translation. As the fluid particle contacts the imposed thermal gradient the continuous phase, one end of its surface becomes warmer than the opposite end. The surface tension is a decreasing function of temperature. Therefore, the surface tension at the warmer end is reduced relative to that at the cooler end, and an interfacial tension gradient or Marangoni force is created which tugs the interface in the direction of the cooler pole. This action creates in the exterior phase an opposing tangential viscous shear traction as it forces a streaming of the continuous phase liquid immediately adjacent to the interface in the direction of the cooler end of the particle. The fluid streaming causes a higher pressure to develop just beyond the cooler end (relative to the pressure at the warmer end) to oppose the flow and preserve an undisturbed state at extended regions away from the particle. The action of the opposing tangential shear and the higher pressure at the cooler end provide a lift force which drives the particle through the continuous liquid in the direction of the higher temperature. At steady state, the lift forces

balanced by the pressure and viscous shear forces acting on the particle which retard the forward motion.

The solution for the thermocapillary migration of a (Newtonian) fluid particle in an infinite (Newtonian) medium to which a linear temperature gradient is applied can be solved exactly in the limit of negligible fluid inertia and heat convection and under the assumption that along the surface the surface tension is a linear function of temperature. With these assumptions, the exact shape of the fluid particle is a sphere, and the terminal velocity is given by Young et al. (1959) as:

$$U_o' = -\frac{a'(\partial\sigma'/\partial T')(\nabla' T')_\infty}{\mu'^{(2)}(1+3\kappa/2)(2+k)}$$

where $\mu'^{(2)}$ is the viscosity of the suspending phase, κ and k are, respectively, the ratio of the particle viscosity and conductivity to that of the suspending phase, a' is the particle radius, $(\nabla' T')_\infty$ is the imposed linear temperature gradient and $\partial\sigma'/\partial T'$ is the constant derivative of the surface tension with respect to temperature.

In terrestrial environments, fluid movement due to thermocapillary migration is usually not important when compared to motions driven by buoyancy. However, thermocapillary forces can become dominant in micro gravity environments where buoyancy effects would not be expected to be important. This past decade has witnessed the emergence of the possibility of processing materials (particularly fluid materials) in the reduced gravity environment of an orbiting spacecraft. By processing in space, novel

processing strategies can be developed which can result in materials whose properties are superior to those fabricated on earth. From an economic point of view, it is anticipated that the high value of these superior space processed materials can offset the cost of their production in space. In some of the suggested micro gravity fluids processing strategies involving bubbles or drops, thermocapillary migration either plays an important role in the process or has been suggested as a means for the management of bubbles and drops. These envisioned applications have provided the major impetus for the growing research activity in thermocapillary migration.

Our research has been motivated by two particular micro gravity processing strategies, the manufacture of high technology glass (Weinberg 1978) and miscibility gap alloy solidification (Bergman, et al. 1982). As described by Weinberg (1978), high technology glass is most favorably manufactured from its melt in a containerless cooling process where impurities cannot leach from the bounding container, and the container cannot serve as a site for heterogeneous nucleation. However, although a micro gravity environment easily allows for such processing, bubbles created in the glass melt in the absence of buoyancy remain suspended and are incorporated in the final product. Thermocapillary migration has been suggested as a means for removal of these bubbles. In miscibility gap solidification, equilibrium liquid alloy mixtures consisting of droplets of one composition dispersed in a continuous phase of another can be formed because of the miscibility gap in the phase diagram. In the absence of buoyancy effects, cooling of this mixture can ultimately result in the

formation of a composite solid material consisting of grains of one composition uniformly interspersed in a solid of another composition. However the quality of the product will be affected by thermocapiillary induced migrations which may reduce the uniformity of the grain structure.

To understand the behavior of thermocapillary migrations in the more complex space processing applications where particle swarms move in the vicinity of fluid or solid boundaries, it is necessary to begin to study and calculate in a fundamental way migration velocities of particles in the presence of the boundaries of other particles or walls. This is an involved subject because the migration velocity of a particle in the presence of a boundary is determined not only by the hydrodynamic resistance the boundary offers to the forward motion of the particle, but also the corresponding thermal interactions between these bodies since these determine the temperature distribution on the fluid particle surface which drives the migration.

Fluid particle-fluid particle, and fluid particle-wall boundary interactions in the context of thermocapillary migration have been studied for several geometries, and we will review this research in the literature review section of this thesis (Chapter II). The review of the literature indicates that while boundary interactions in which the boundary is placed normal to the direction of motion of the bubble (as for example a drop approaching a wall, or two drops approaching each other) have been studied fairly extensively. However, lateral interactions in which bubbles move parallel to boundaries have not been as well investigated. In the thesis research, we study a model problem for lateral interactions. The problem consists of a bubble or

drop which is placed in a tube, and which moves axisymmetrically along the tube centerline by virtue of an imposed temperature gradient. The motion is assumed to be slow enough that the fluid inertia can be neglected (creeping or low Reynolds number slow). We study compact fluid particles in which the spherical radius of the particle (i.e. the particle radius when it assumes a spherical configuration) is smaller than the tube radius. Strong hydrodynamic interactions occur for ratios of the (characteristic) particle radius to that of the tube which approach and exceed one. For this range, the particle interface approaches the tube wall, and a small gap develops between the particle and the wall. In order to study strong thermal interactions, the tube wall is taken to be insulated. When the drop conductivity becomes much less than that of the continuous face, energy must be conducted through the gap and this gives rise to large temperature gradients on the particle surface which enhance the thermocapillary migration. The objective of the research is to resolve, in this model problem, the competition between retarding hydrodynamic and enhancing thermal interactions as the characteristic particle radius approaches that of the wall.

The research is divided into two parts. In the first part we study compact fluid particles for which surface tension forces are assumed to be dominant, and the drop remains spherical. A boundary collocation method (applicable to spherical drop geometry) is used to solve for the temperature distribution and the hydrodynamics. In the second part of the study, the large surface tension restriction is relaxed, and drop motion, including deformation is studied by using a boundary integral method for compact particles.

An outline of this research thesis is as follows. The thesis is divided into four chapters. In the first (Chapter II), a literature review which outlines previous studies in thermocapillary migration is given. In the second (Chapter III), the research on the movement of compact spherical fluid particles is detailed. These results have already been published in the Journal of Fluid Mechanics (233, 405-437 (1991)). The research on deformation is described in Chapter IV. There we outline the implementation of the boundary integral technique for the thermocapillary problem, and provide some results on how compact particles deform, and the influence of deformation on their velocity.

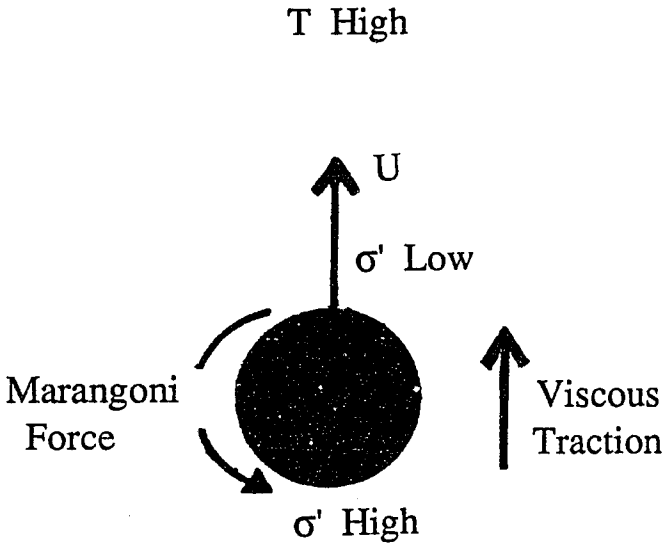

Fig.1

Chapter II

LITERATURE REVIEW

This literature review is divided into two major sections. In the first, we review the theoretical research on the thermocapillary movement of fluid particles, including the effects of interaction between particles and the influence of bounding geometry. In the second section, we review those numerical techniques which have been used to study, in general, the motion of fluid particles in tubes.

II.1. Thermocapillary Studies

The first theoretical study of the thermocapillary migration of a fluid particle was undertaken by Young, Goldstein & Block (1959) who studied the motion of a single gas bubble in an unbounded continuous phase, neglecting fluid inertia (low Reynolds number, Re) and the convective transport of energy (low Peclet number, Pe). In these limits the spherical shape is an exact solution of the governing equations, and thus no restriction on the capillary number (Ca), the ratio of the magnitudes of viscous distending traction to the surface tension force, need be imposed. This fundamental solution has been corrected to examine the influences of finite inertia and the convective transport of heat. Inclusion of these effects leads to deformation, and this subject has been studied generally for bubbles and drops asymptotically in small Ca, Re and Pe by Bratukhin

(1976), Thompson, DeWitt & Labus (1980), Balasubramanian and Chai (1987) and Haj-Hariri, Nadim & Borhan (1990). The effect of the convective transport of energy for the single fluid particle problem was studied for a spherical geometry (zero capillary number) and negligible inertia asymptotically for small Pe by Subramanian (1981, 1983) and numerically for order one Pe by Shankar and Subramanian (1988) and for order one Pe and Re by Balasubramanian and lavery (1989). These latter results established that the convective transport of energy reduces the surface temperature gradient on the particle surface and thereby reduces the migration velocity. Recent advances on the single fluid particle problem have examined the retardation in thermocapillary migration owing to the adsorption of an insoluble surfactant monolayer on the drop surface (Kim and Subramanian 1989a, b, and Nadim and Borhan 1989).

Fluid particle-particle, and fluid particle-wall boundary interactions in the context of thermocapillary migration have been studied for several geometry. Meyyappan, Wilcox and Subramanian (1981) examined the quasi static movement of a spherical gas bubble perpendicular to an isothermal fluid or solid plane for zero Pe and Re. Solutions for the temperature isotherms demonstrated that the temperature gradient along the bubble surface decreases as the fluid particle approaches the wall. This behavior, taken together with the increasing hydrodynamic retardation as the fluid particle approaches the wall, causes the migration velocity to decrease from the value in an infinite medium. Ascoli and Leal (1990) reexamined this problem for the case of order one capillary numbers and a solid surface, and found that bubble flattening as the fluid particle comes within a

diameter or so of the wall causes the terminal velocity to be greater than the spherical value, but still less than one. The corresponding problem of a liquid drop of finite conductivity moving normal to a plane surface was studied by Barton and Subramanian (1990) and Chen and Keh (1990) for spherical drops and negligible inertia and thermal convection, and Ascoli and Leal (1990) under the same assumptions except allowing deformation. The results for the migration velocities can be significantly different from those for the migration of a bubble, and these differences illustrate the important role played by the thermal interaction. Both Barton and Subramanian and Chen and Keh determined that when the conductivity of the surrounding medium is less than the drop phase, the temperature gradient on the drop surface increases as the fluid particle approaches the wall. Both studies found that for the case of a fluid wall, as the droplet approaches the wall, the increase in the temperature gradient offsets the increasing hydrodynamic retardation, and the particle velocity increases from its value in an unbounded region.

Other studies have examined problems similar to those above in which the hydrodynamic and thermal interactions occur normal to the direction of motion. Meyyappan, Wilcox and Subramanian (1983) investigated numerically the rectilinear, quasi-static movement of two unequal sized spherical bubbles along their line of centers, again for negligible inertia and thermal convection. From the results, Meyyappan et al. developed a useful rule for approximately predicting the migration velocities for separation distances that are not very small compared to the fluid particle diameters, and this rule allows for a qualitative understanding of the thermal and

hydrodynamic interaction for the two fluid particle case. For each sphere, the migration velocity may be approximately obtained by summing two terms. Consider the calculation for sphere "a" separated by a center-to-center distance "d'" from sphere "b", with both spheres subject to a far-field temperature gradient $(\nabla' T')_\infty$ The first term in the approximation is the velocity of "a" due to the streaming motion induced by the isolated migration velocity of "b" . The second is the thermocapillary migration velocity of "a" in an infinite medium subject to a far field temperature gradient equal to the local gradient which exists a distance "d" from "b", when "b" is isolated and subject to $(\nabla' T')_\infty$ Since, for a bubble, this local gradient is smaller than $(\nabla' T')_\infty$ owing to the distortion in the isotherm field caused by "b", this elementary approximation for the thermal interaction reduces the motion of "a" relative to its value in an infinite medium. Meyyappan et al. found that for the smaller particle, the streaming of the larger particle acting on the smaller one overcompensates for the reduction in the terminal velocity owing to the thermal interaction, and the fluid particle moves faster then when isolated. For the larger fluid particle, since the streaming motion due to the smaller fluid particle is not as large, the thermal interaction dominates and slows the particle down from the infinite medium value. For equal sized spheres, these effects cancel in this approximation, and the particles move with isolated velocities, a result confirmed for all separation distances numerically by Meyyappan et al. and analytically by Feuillebois (1989). This heuristic approximation has also been used in studying the normal interaction problem of the eccentric thermocapillary migration of a bubble moving in a spherical drop along

whose surface a temperature gradient is imposed (Shankar, Cole and Subramanian 1981, Annamalai, *et al.* 1982, and Shankar and Subramanian 1983). This eccentric motion was reconsidered by Morton, Subramanian & BalaSubramaniam (1990) for the more general case in which the inside fluid particle is a drop, and the outside drop is placed in a temperature gradient and its surface temperature is determined by solving the conduction problem of one drop embedded inside another. The problem of two gas bubbles moving rectilinearly along their line of centers has been generalized to include the influence of droplet viscosity by Keh and Chen (1990). Meyyappan & Subramanian (1984), using a far-field technique, and satraps using a multiple expansion technique constructed approximate solutions for the thermocapillary motion of two bubbles moving with an arbitrary orientation with respect to each other. Anderson (1985) studied the thermocapillary motion of two droplets moving with an arbitrary orientation with respect to each other by the method of reflections. Finally, Wei and Subramanian (1993) and Keh and Chen (1992) used a boundary collocation technique to solve for the thermocapillary movement of a small chain of two or three spherical bubbles.

For lateral motion, this question of competition between thermal and hydrodynamic interaction has not been fully examined. Meyyappan and Subramanian (1987) studied the motion of a spherical bubble parallel to a plane solid wall for negligible inertia and thermal convection, and found that the velocity decreased relative to the isolated value for parallel motions close to the wall. In this case resistance to heat transfer through the particle-surface gap should enhance the migration velocity. Nevertheless,

the result indicates that the hydrodynamic resistance is overriding. It should be noted, however, that the wall was assumed isothermal in the study of Meyyappan and Subramanian, not insulated, and therefore heat can be conducted through the wall. In addition much of the energy can be conducted around the side of the particle away from the wall rather than through the gap. Both of these factors act to reduce the surface temperature gradient and explain the dominance of hydrodynamic resistance. The tube geometry adopted in this study, because it does not have these mitigating factors, is a more appropriate model for assessing strong thermal interaction. The only study undertaken for thermocapillary migration in a cylindrical geometry was that of Hasan and Balasubramaniam (1989), who studied the motion of a long gas slug in an isothermal tube owing to an axial temperature gradient. An approximate solution for the migration velocity was obtained based on a lubrication solution of the hydrodynamic equations in the thin film region surrounding the cylindrical portion of the bubble, and an overall force balance to calculate the pressure gradient in the film. The approximate result for the migration velocity decreases as the gap thickness between the slug and the tube wall decreases, again indicating the dominance of hydrodynamic interaction for the isothermal wall case.

II.2 Numerical Solutions for the Hydrodynamic Motion of Bubbles and Drops in Tubes

In this section, we review the various techniques which have been used to develop numerical solutions for the hydrodynamic movement of fluid

particles in cylindrical tubes. We focus our review on studies in which both the bounding and droplet phases are Newtonian, and the flow is described by the Navier Stokes equations. Most studies have used one of four techniques. These are (i) finite difference methods, (ii) finite element techniques, (iii) boundary collocation techniques and (iv) boundary integral methods. These are reviewed separately below.

The finite difference method requires the construction of a mesh in the domain bounded by the tube surface and the fluid particle interface (and also the inside of the particle if the particle interior is not a passive gas phase), and the discretization of the hydrodynamic equations and interfacial and tube wall boundary conditions into a set of difference equations for the values of the components of the velocity vector at the vertices of the mesh. These equations are then solved subject to the interfacial and wall boundary conditions to obtain a numerical representation of the velocity field. The finite difference method was used to study the steady, creeping, axisymmetric motion of an infinite gas finger in a tube (and channel) by Reinelt and Saffman (1985) and Reinelt (1987) and of finite sized gas slugs in a tube by Westborg and Hassager (1989). Reinelt and Saffman (1985) and Westborg and Hassager (1987) were able to obtain converged solutions for values of the capillary number (the quotient of the product of the slug or finger velocity multiplied by the suspending phase viscosity and divided by the surface tension) in the range of 0.01 - 1. As the capillary number became smaller than 0.01, the film thickness around the finger or slug becomes small, and it becomes difficult to construct a mesh size fine enough in the thin film region to obtain converged solutions. However,

Reinelt (1987) was able to obtain converged solutions for Ca as low as 10^{-4} by using a very fine mesh.

The finite element method also requires a discretization of the domain bounding the interior and exterior of the particle. The hydrodynamic variables are approximated by expansion in a set of basis functions in each element, and a weighted residual technique is used to compute the constants in the expansion. This method was used by Shen and Udell (1985) to solve the problem treated by Reinelt and Saffman of the axisymmetric, creeping movement of an infinite gas finger in a tube. Skalak and coworkers (T$\ddot{o}$zeren and Skalak (1977)) also used the finite element method to solve for the movement in a circular tube of a periodic array of liquid drops encapsulated by an elastic membrane, as a model for the motion of red blood cells in blood vessels.

Although they have only been used to describe creeping motions, the finite difference and finite element techniques are not restricted to these slow flows. The last two techniques, the boundary collocation and boundary integral (or element) techniques develop general solutions for the linear Stokes equations, and these allow the implementation of numerical schemes in which the only unknown quantities are at the system boundaries. As these solutions are only valid for the Stokes equations, the numerical schemes which follow can only describe creeping motions.

In the collocation method, general solutions to the axisymmetric Stokes equations are developed which are a sum of Fourier transform (for a single particle) or series (for an infinite train of particles) solutions which are bounded at the tube center, and a Legendre expansion singular at the

center of the sphere. Wall conditions are satisfied identically using an inverse transform or orthogonal series calculation, and interfacial boundary conditions are satisfied at discrete points on the sphere surface. The collocation method has been used primarily to study the motion of spheres in tubes, where it has been found to give very accurate results for ratios of the particle to the tube radius as large as 0.9. With this method, Wang and Skalak (1969) and Hyman and Skalak (1972a) examined the motion of a periodic train of solid and fluid spheres, Leichtberg, Pfeffer and Weinbaum (1976) studied the motion of clusters of a few solid spheres in a tube, and He, Dagan & Maldarelli (1991) treated the motion of single bubbles and drops with adsorbed monolayers of surfactant. The method was also applied to the motion of a train of deformable spheres in tubes by Hyman and Skalak (1972).

The starting point of the boundary integral method is an integral solution (a Green's formulae for the Stokes equations) for the velocity at a point on the fluid particle surface in terms of the velocity and stress along the particle surface, and the stress along the wall surface. This technique was first applied to tube flows by Tözeren (1984) who studied the motion of single solid spheres in tubes. The method was utilized to study the deformation of single compact fluid particle by Martinez and Udell (1990), for gas slugs by Martinez and Udell (1989) and for compact and elongated particles with insoluble surfactant monolayer by Borhan and Mao (1992). Like the finite difference method, the boundary integral technique also has problems with convergence when the interface of the fluid particle comes close to the wall.

Chapter III

AXISYMMETRIC THERMOCAPILLARY MOTION OF FLUID SPHERES IN A TUBE*

III.1. Introduction

In this chapter we study the thermocapillary motion of a fluid sphere moving axially in a tube. The chapter is divided into three major sections. in the first (Section 2), the fluid mechanical and thermal field and boundary equations are detailed Section 2.1, and the numerical solution technique is described (Sections 2.2 and 2.3). Numerical solutions are obtained by a boundary collocation procedure (Leichtberg, Pfeffer and Weinbaum (1976)) in which general analytical solutions to the Stokes and Laplace equations which satisfy the tube wall conditions exactly are developed, and made to satisfy the particle surface conditions at discrete points on the surface. The results are detailed in Section 3 in three parts. The first section 3.1 presents the solutions for the conduction problem in terms of temperature isotherms, and graphs of the surface temperature distribution and pole temperature difference. The second section describes hydrodynamic results. This linear Stokes flow problem is separable into two fixed-fluid particle flow idealizations, one in which a uniform flow from infinity streams over the fluid particle in the absence of a thermocapillary force, and a second in which the thermocapillary stress causes fluid streaming in closed

* Reprinted by Journal Fluid Mechanics, Chen et al. 1991, vol.233, pp 405-437

convection cells with no flow far away from the particle. Each idealization contributes a force on the particle, and in Section 3.2, these forces are described as a function of force coefficients which are presented graphically in terms of the conductivity and viscosity particle-continuous phase ratios, and the sphere to tube diameter quotient. The terminal velocity relative to that of an isolated particle is determined by the ratio of the force coefficients, and in Section 3.3 the relative velocity is detailed as a function of the particle to tube diameter ratio and conductivity and viscosity ratios. From these results, conclusions are drawn as to whether thermal or hydrodynamic effects become overriding as the gap thickness decreases. A summary concludes this chapter Section 4.

III.2. Formulation and Solution Procedure

III.2.1 *Thermal and Hydrodynamic Field Equations and Boundary Conditions*

The problem is formulated in a reference frame which is fixed to the particle, and which is therefore moving with a uniform velocity U' relative to the stationary laboratory frame. In this paper, dimensional quantities are marked by a prime, and dimensionless quantities are unprimed. In the moving frame, cylindrical (ρ',ω,z') and spherical coordinates (r',θ,ϕ) are located with the origins of both systems taken to be at the fluid particle center, and the z'-axis of the cylindrical system coincident with the tube centerline (see Fig.1). Note that in this fluid particle fixed frame the wall is moving in the z'-direction with velocity -U'. The radius of the fluid particle

and of the tube are denoted, respectively, by a' and b'. Droplet and continuous phase variables are denoted by superscripts (1) and (2) respectively. Finally, viscosities and thermal conductivities are denoted by $\mu'^{(i)}$ and $k'^{(i)}$, and the ratios of the droplet to the continuous phase viscosity and conductivities are denoted by κ and k respectively. The temperature gradient is imposed in the laboratory frame. Far from the drop, in the lab frame, the temperature field is of the form $T'(\zeta') = (\nabla' T')_\infty \zeta' + T'_o$ where T' denotes the temperature, $(\nabla' T')_\infty$ denotes the imposed gradient, and ζ' is the lab frame cylindrical axial coordinate. This coordinate is related to the fluid particle fixed axis coordinate z' by $z'=\zeta'-U't'$. Thus in the moving frame the temperature field far from the drop is given by $T'(z') = (\nabla' T')_\infty z' + (\nabla' T')U' t' + T'_o$. The dependence of the surface tension σ' on the temperature is assumed to be linear, and the constant gradient is denoted by $\partial\sigma'/\partial T'$. Non-dimensionalizations are formulated using the following scaling: spatial coordinate variables r', z' and ρ' are scaled by the particle radius a'. Velocities are scaled by U'_o, the terminal velocity for the case in which the walls are infinitely far away and the fluid particle therefore translates in an infinite medium. This velocity is given by Young *et al.* (1959) as

$$U'_o = -\frac{a'(\partial\sigma'/\partial T')(\nabla' T')_\infty}{\mu'^{(2)}(1+3\kappa/2)(2+k)} \qquad (1)$$

A non-dimensional temperature field $\Theta^{(i)}(z,\rho)$ measured in the moving system is defined as:

$$\Theta^{(i)}(z,\rho)=(T'^{(i)}(z,\rho)-(\nabla' T')_\infty U' t'-T_o')/(a'(\nabla' T')_\infty)$$

Note that this field must tend to $\pm$ z as $z \to \pm\infty$. When the thermal equations are cast in non-dimensional form using $\Theta^{(i)}(z,\rho)$, it can easily be shown that $\Theta^{(i)}(z,\rho)$ is antisymmetric with respect to z for all ρ. Therefore $\Theta^{(i)}(z=0, \rho)=0$ and the dimensional temperature along the equatorial plane is equal to $(\nabla' T')_\infty U' t'+T_o'$. Since the non-dimensional temperature field is antisymmetric with respect to z, the Marangoni force, which is proportional to $(\partial\Theta^{(i)}/\partial\theta)(r=1)=\cos\theta(\partial\Theta^{(i)}/\partial\rho)(r=1)-\sin\theta(\partial\Theta^{(i)}/\partial z)(r=1)$ is an even function of z. Hence the velocity field is symmetric with respect to the sphere equator: $V_\rho^{(i)}(\rho,z)=-V_\rho^{(i)}(\rho,-z)$, and $V_z^{(i)}(\rho,z)=V_z^{(i)}(\rho,-z)$.

In formulating the energy conservation equations, thermal convection is neglected under the assumption of small Peclet number, and Laplace's equation describes the temperature field at steady state:

$$\nabla^2\Theta^{(i)}=0 \tag{2}$$

The boundary conditions on the temperature fields are as follows:

(1) The tube wall, ρ= b'/a', is insulated:

$$\frac{\partial\Theta^{(2)}}{\partial\rho}=0 \tag{3}$$

(2) At the bubble surface, r=1, the heat flux and temperature are continuous across the interface:

$$k\frac{\partial\Theta^{(1)}}{\partial r}=\frac{\partial\Theta^{(2)}}{\partial r} \tag{4}$$

$$\Theta^{(1)}=\Theta^{(2)} \tag{5}$$

(3) Far from the bubble, the temperature field in the continuous phase is linear in z:

$$\lim_{|z|\to\infty}\Theta^{(2)}=z \tag{6}$$

(4) At the center of the sphere (r=0), the temperature is finite.

Since the hydrodynamic flow is axisymmetric and the fluids incompressible, non-dimensional velocities may be expressed in terms of a non-dimensional stream function $\psi^{(i)}(\psi^{(i)}=\Psi'^{(i)}/(a'^2U'_o))$. Two representations of $\psi^{(i)}$ are used, one in terms of cylindrical coordinates (ρ,z) and one in terms of spherical coordinates (r,θ). These representations are related to the velocity fields as expressed in the respective systems by the following relations:

$$V_r^{(i)}=-\frac{1}{r^2\sin\theta}\frac{\partial\Psi^{(i)}}{\partial\theta},\qquad V_\theta^{(i)}=\frac{1}{r\sin\theta}\frac{\partial\Psi^{(i)}}{\partial r} \tag{7}$$

$$V_z^{(i)}=-\frac{1}{\rho}\frac{\partial\Psi^{(i)}}{\partial\rho},\qquad V_\rho^{(i)}=\frac{1}{\rho}\frac{\partial\Psi^{(i)}}{\partial z} \tag{8}$$

For steady, creeping flows the Navier-Stokes equations in terms of the stream function is of the form

$$E^2(E^2\Psi^{(i)}) = 0 \tag{9}$$

where E^2 is the axisymmetric stream function operator. The definitions of this operator in cylindrical and spherical coordinates is given by Happell & Brenner (1973) as:

$$E^2\Psi = \frac{\partial^2\Psi}{\partial r^2} + \frac{\sin\theta}{r^2}\frac{\partial}{\partial\theta}\left(\frac{1}{\sin\theta}\frac{\partial\Psi}{\partial\theta}\right) \tag{10}$$

$$E^2\Psi = \frac{\partial^2\Psi}{\partial z^2} + \frac{\partial^2\Psi}{\partial\rho^2} - \frac{1}{\rho}\frac{\partial\Psi}{\partial\rho} \tag{11}$$

For the velocity field the boundary conditions are:

(1) At the bubble center $\lim_{r\to 0} = V_r^{(1)}$ and $\lim_{r\to 0} V_\theta^{(1)}$ exist.

(2) Far from the bubble, the velocity field is uniform

$$\lim_{|z|\to\infty} V_z^{(2)} = -U \tag{12}$$

where U is the nondimensional velocity of the particle ($U=U'/U'_0$).

(3) At the tube wall, $\rho=b'/a'$, the velocity is equal to the wall velocity:

$$V_z^{(2)} = -U, \qquad V_\rho^{(2)} = 0 \tag{13a,b}$$

(4) At the surface of the bubble (r=1) velocities are continuous, the normal velocity is equal to zero and the difference in tangential shear stresses is balanced by the Marangoni force:

$$V_\theta^{(1)} = V_\theta^{(2)} \tag{14}$$

$$V_r^{(1)} = V_r^{(2)} = 0 \tag{15}$$

$$\left(\frac{\partial V_\theta^{(2)}}{\partial r} - \frac{V_\theta^{(2)}}{r}\right) - \kappa\left(\frac{\partial V_\theta^{(1)}}{\partial r} - \frac{V_\theta^{(1)}}{r}\right) = (1+3\kappa/2)(2+k)\frac{\partial \Theta^{(2)}}{\partial \theta} \tag{16}$$

It is important to note that since the tangential stress balance equation (16) has been non-dimensionalized using the infinite medium migration velocity (equation (1)), which itself is proportional to the constant surface tension gradient $\partial\sigma'/\partial T'$, the non-dimensional tangential stress balance becomes independent of this gradient.

III.2.2 *Solution for the Temperature Field*

Owing to the neglect of convection, the energy equations (2)-(6) are independent of the velocity field, and may therefore be solved independently. In the fluid particle interior, the general solution to Laplace's equation which is bounded at the origin (cf. consideration Eq.(4) after Eq.(6)) may be formulated as an infinite series in Legendre polynomials. Since the temperature field is antisymmetric with respect to z, only odd Legendre polynomial are included in the series summation. Therefore:

$$\Theta^{(1)}(r,\theta) = \sum_{n=1}^{\infty} A_n P_n(\cos\theta) r^n \qquad \text{(n=odd)} \tag{17}$$

where $P_n(\cos\theta)$ denote the Legendre functions.

For the continuous phase, a general solution to Laplace's equation for $\theta^{(2)} - z$ can be constructed by the addition of the general integral solution in cylindrical coordinates which is bounded as $\rho \to 0$, tends to zero as $z \to \pm\infty$ and is odd in z, and the spherical coordinate solution which also disappears as $r \to \infty$ and is antisymmetric in θ with respect to $\pi/2$:

$$\Theta^{(2)}(\rho, z, r, \theta) = \int_o^\infty C(t) I_0(t\rho) \sin tz dt + \sum_{n=1}^{\infty} B_n P_n(\cos\theta) r^{-(n+1)} + z$$

(n=odd) (18)

where I_0 is the modified Bessel functions of the first kind, and the restriction to odd indices in the Legendre expansion is due to the antisymmetry of the temperature field. Note that this construction satisfies the boundary condition at infinity (Eq.(6)).

The technique used to obtain, from the boundary conditions (3)-(5), the constants A_n and B_n in the Legendre expansions and the function C(t) in the integral solution is described as follows. First, the zero flux boundary condition on the tube wall is satisfied exactly by using a Fourier sine inversion to solve for the unknown function C(t) in terms of a Legendre expansion of the B_n constants. Secondly, a multipole collocation technique is used to satisfy the boundary conditions on the surface of the drop.

The spherical coordinates in the exterior phase solution may be rewritten in terms of cylindrical coordinates by using the transformations $\theta(\rho,z)=\text{Arctan}(\rho/z)$ $(0 \leq \theta < \pi)$, $\cos\theta = z/(\rho^2 + z^2)^{1/2}$ and $r = (\rho^2 + z^2)^{1/2}$. By using this

transformation in Eq.(18), the zero-flux boundary condition may be written in the form:

$$0 = \frac{\partial \Theta^{(2)}}{\partial \rho}(\rho = R) = \int_o^\infty tC(t) I_1(tR) \sin tz dt$$
$$+ \sum_{n=0}^{\infty} B_n \frac{\partial}{\partial \rho}\left[P_n\left(\frac{z}{\sqrt{\rho^2 + z^2}}\right)(\rho^2 + z^2)^{-(n+1)/2} \right]_{|\rho=R} \qquad \text{(n=odd)} \qquad (19)$$

In the above, the ratio b'/a' is denoted by R. The function C(t) may be obtained from Eq.(19) by inverting and then integrating the inverse integral. The result is:

$$C(t) t I_1(Rt) = -\sum_{n=0}^{\infty} B_n \frac{\partial}{\partial \rho}[Q_n(\rho, t)]_{|\rho=R} \qquad (20)$$

where

$$Q_n = \frac{2}{\pi}\int_o^\infty P_n\left(\frac{z}{\sqrt{\rho^2 + z^2}}\right)(\rho^2 + z^2)^{-(n+1)/2} \sin tz dz$$

Integrating the above (Leichtberg *et al.* 1976) yields:

$$Q_n = (-1)^{(n-1)/2} \frac{2}{\pi n!} t^n K_0(\rho t)$$

and K_0 is a modified Bessel function of the second kind. By differentiating Q_n with respect to ρ a final expression for C(t) may be obtained:

$$C(t) = \sum_{n=1}^{\infty} B_n T_n(Rt)$$

where $T_n = (-1)^{(n-1)/2}(2/\pi n!)t^n K_1(Rt)/I_1(Rt)$. For a fixed t, the above series for C(t) rapidly converges because of the n! in the denominator.

Substituting this solution for C(t) into equation Eq.(18) allows for the representation of the exterior phase solution to be written in the form:

$$\Theta^{(2)}(r,\theta) = \sum_{n=1}^{\infty} B_n \int_o^{\infty} T_n(Rt) I_0(tr\sin\theta)\sin(tr\cos\theta)dt + \sum_{n=1}^{\infty} B_n P_n(\cos\theta) r^{-(n+1)} + r\cos\theta \qquad \text{(n=odd)} \qquad (21)$$

The thermal boundary conditions at the sphere surface r=1 (Eqs. (4) and (5) can be applied directly to the solution forms given by Eqs.(17) and (21):

$$k\sum_{m=1}^{\infty} A_m m P_m(\cos\theta) = \cos\theta - \sum_{m=1}^{\infty} B_m (m+1) P_m(\cos\theta) + \sum_{m=1}^{\infty} B_m \int_o^{\infty} T_m(Rt) t I_1(t\sin\theta)\sin(t\cos\theta)\sin\theta dt + \sum_{m=1}^{\infty} B_m \int_o^{\infty} T_m(Rt) t I_0(t\sin\theta)\cos(t\cos\theta)\cos\theta dt \qquad (22)$$

$$\sum_{m=1}^{\infty} A_m P_m(\cos\theta) = \cos\theta + \sum_{m=1}^{\infty} B_m P_m(\cos\theta) + \sum_{m=1}^{\infty} B_m \int_0^{\infty} T_m(Rt) I_0(t\sin\theta)\sin(t\cos\theta)dt \qquad (23)$$

The above two equations are in terms of the remaining unknown infinite sets of constants, A_m and B_m. It is important to note that when the expression for $T_m(Rt)$ is inserted into the improper integrals appearing in the above two equations, the resulting integrands can easily be shown to be of order $t^{m+1/2}e^{t(\sin\theta-2R)}$ (for Eq.(22)) or $t^{m-1/2}e^{t(\sin\theta-2R)}$ (for Eq.(23)) as $t\to\infty$ and are bounded as $t\to 0$. Because of these properties, the improper integrals are readily seen to be convergent. Numerical integration was undertaken by using the integration package DQDAG from the IMSL Math Library. This routine only accepts numerical values for the upper and lower limits. The lower limit was set equal to a value of 10^{-8}. A sufficiently large value of the upper limit was found so that for values larger than this one, the change in the value of the integral was negligible. The contribution from 0 to the lower limit was then estimated using asymptotic formulae for the integrand as $t\to 0$, and this estimate was then checked against the value of the integral to confirm that it was a small contribution.

The constants A_m and B_m are determined from Eqs.(22) and (23) by a multipole collocation technique in which these equations are satisfied at M discrete points on the sphere surface, and the summations in the equations are truncated so as to include terms up to B_{2M-1} and A_{2M-1}. The result is a set of 2M linear equations in terms of 2M constants which can be cast in the following way:

$$k\sum_{m=1}^{2M-1}\{A_m mP_m(\cos\theta_i)+B_m[(m+1)P_m(\cos\theta_i)$$
$$-\int_o^\infty T_m(Rt)tI_1(t\sin\theta_i)\sin(t\cos\theta_i)\sin\theta_i dt$$

$$-\int_o^\infty T_m(Rt)tI_0(t\sin\theta_i)\cos(t\cos\theta_i)\cos\theta_i dt]]$$

$$=\cos\theta_i \qquad (24)$$

$$\sum_{m=1}^{2M-1}\{A_m P_m(\cos\theta_i) - B_m[P_m(\cos\theta_i)$$

$$+\int_0^\infty T_m(Rt)I_0(t\sin\theta_i)\sin(t\cos\theta_i)dt]]$$

$$=\cos\theta_i \qquad (25)$$

where i denotes the collocation point (i=1,2,...M).). Note that because of the antisymmetry, collocation points need only be taken along the first quadrant of the sphere. The above set can be solved by matrix inversion to yield values for the constants A_m and B_m up to index 2M-1. As M is increased sufficiently, the values obtained for A_m and B_m by inversion of matrices of higher rank begin to converge, and the truncated expressions for the temperature field approach the exact solution.

In this implementation of the collocation technique, the convergence criteria is based on incrementing M until a prescribed resolution is achieved for the temperature gradient on the surface of the drop. At the level M, this gradient is given by the truncated expression:

$$\frac{\partial\Theta^{(1)}}{\partial\theta}(1,\theta_i) = \sum_{m=1}^{2M-1} A_m[mzP_m(z) - mP_{m-1}(z)]/\sin\theta_i \qquad (26)$$

Convergence is formulated in this way because the gradient in the surface temperature is what determines directly the hydrodynamic flow field and terminal velocity. At each level in M, the surface temperature gradient is

evaluated from the truncated expression at three degree intervals along the first quadrant of the drop from θ=0. These values are then compared with the surface temperature gradient at the same points on the sphere surface for the level M-1, and the gradient field is deemed converged when the difference at each angular location is less that 10^{-5}%. Example values of M necessary to satisfy this criteria are given on the first row in table 1 as a function of a'/b' for k=10^{-5}. Note that as the ratio of the sphere to the tube diameter increases, M increases. As will be discussed in the Results section (Section 3), for this case of a non-conducting sphere, the surface temperature gradient strongly increases with θ in the first quadrant as heat is conducted through the narrow gap between the sphere and tube wall, and more terms in the series expansion are necessary to describe this behavior.

Some final notes with regard to the implementation of the collocation procedure: an examination of the linear algebraic equations (24) and (25) shows that when the collocation points θ_i=0 and $\pi/2$ are used the equations become linearly dependent. In order to overcome this difficulty, these points can be replaced by closely adjacent points, i.e. θ_i=0-ε and θ_i= $\pi/2$-ε. The optimum value of ε is 0.8° as established by Leichtberg et al.(1967).

III. 2.3 *Solution of the Velocity Field*

A general solution for the stream function of the droplet phase in spherical coordinates in which velocities are bounded at the drop center

(consideration (1) preceding Eq.(12)) may be expressed in terms of an infinite series of Gegenbauer polynomials $C_n^{-1/2}(\cos\theta)$:

$$\Psi^{(1)}(r,\theta)=\sum_{n=2}^{\infty}(E_n^{(1)}r^n+F_n^{(1)}r^{n+2})C_n^{-1/2}(\cos\theta) \qquad \text{(n=even)} \qquad (27)$$

where the restriction to even terms is a consequence of the flow field symmetry about the equatorial plane. For the continuous fluid, note first that the stream function must from Eq.(13) tend to $U\rho^2/2$ as $|z|\to\infty$ in order to match to the uniform flow. Denoting this uniform flow field by $\Psi_\infty(\rho)$, solutions for $\Psi^{(2)}-\Psi_\infty(\rho)$ must tend to zero as $|z|\to\infty$. General solutions which obey this far-field restriction may be constructed by the addition of the general cylindrical solution which is bounded as $\rho\to 0$ and tends to zero as $|z|\to\infty$ and the spherical solution which disappears as $r\to\infty$:

$$\Psi^{(2)}=\Psi_\infty(\rho)+\int_o^\infty[A(t)\rho I_1(t\rho)+B(t)\rho^2 I_0(t\rho)]\cos tz\,dt$$
$$+\sum_{n=2}^{\infty}(E_n^{(2)}r^{-n+1}+F_n^{(2)}r^{-n+3})C_n^{-1/2}(\cos\theta) \qquad \text{(n=even)} \qquad (28)$$

As was the case with the solution for the temperature field, the determination of the hydrodynamic constants and functions is undertaken by a two-step procedure in which the wall conditions are satisfied exactly by a Fourier inversion, and the conditions on the fluid particle surface are satisfied numerically at collocation points.

The boundary conditions on the surface of the tube are given by Eq.(13); in order to satisfy these conditions, explicit expressions for the velocity fields in the cylindrical system for the solution form given by Eq.(28) are given first with the aid of the spherical - cylindrical coordinate transformation:

$$V_z(z,\rho) = -\frac{1}{\rho}\frac{\partial \Psi_\infty}{\partial \rho} - \int_o^\infty \{A(t)tI_0(t\rho) + B(t)[\rho t I_1(t\rho) + 2I_0(t\rho)]\}\cos(tz)dt$$
$$- \sum_{n=2}^{\infty}[E_n^{(2)}G_n^1(\rho,z) + F_n^{(2)}G_n^2(\rho,z)] \qquad (29a)$$

$$V_\rho(z,\rho) = \int_o^\infty [A(t)I_1(t\rho) + B(t)\rho I_0(t\rho)]t\sin(tz)dt$$
$$+ \sum_{n=2}^{\infty}[E_n^{(2)}G_n^5(\rho,z) + F_n^{(2)}G_n^6(\rho,z)] \qquad (29b)$$

where the functions $G_n^k(\rho,z)$ appearing in the above are detailed in the Appendix. From Eqs.(13a) and (29a) the following equation is obtained:

$$\int_o^\infty \{A(t)tI_0(Rt) + B(t)[RtI_1(Rt) + 2I_0(Rt)]\}\cos(tz)dt$$
$$= -\sum_{n=2}^{\infty}[E_n^{(2)}G_n^1(R,z) + F_n^{(2)}G_n^2(R,z)] \qquad (30)$$

From Eq.(13b) it is clear that the stream function at the wall is a constant; from the solution form of Eq.(28) this constant is clearly equal to $\Psi_\infty(\rho = R)$ and the integral and series summations must equal zero:

$$\int_o^\infty [A(t)RI_1(Rt) + B(t)R^2 I_0(Rt)]\cos(tz)dt$$

$$= -\sum_{n=2}^{\infty}[E_n^{(2)}G_n^3(R,z)+F_n^{(2)}G_n^4(z)] \tag{31}$$

By applying Fourier cosine integral inversions to Eqs.(30) and (31), A(t) and B(t) can be expressed in terms of the constants $E_n^{(2)}$ and $F_n^{(2)}$ as follows:

$$A(t)tI_0(Rt)+B(t)[RtI_1(Rt)+2I_0(Rt)] = -\sum_{n=2}^{\infty}[E_n^{(2)}H_n^1(t)+F_n^{(2)}H_n^2(t)]$$
$$A(t)RI_1(Rt)+B(t)R^2I_0(Rt) = -\sum_{n=2}^{\infty}[E_n^{(2)}H_n^3(t)+F_n^{(2)}H_n^4(t)] \tag{32}$$

where the functions $H_n^i(t)$, i=1,2,3,4, are obtained by analytical integration (Leichtberg et al. 1976) and are detailed in the Appendix. The integrals which define the $H_n^i(t)$ functions are, like the corresponding conduction integrals, improper and divergent at the lower (zero) limit. However, by using asymptotic formulae, the divergence can be shown to be integrable, and the improper integral is convergent. In the numerical solution to follow, these integrals were once again evaluated using the IMSL's DQDAG routine, and the integral limits were specified in a manner which was similar to that used for the conduction integrals.

From Eq.(32), A(t) and B(t) can be solved in terms of the unknown constants $E_n^{(2)}$ and $F_n^{(2)}$. Substituting this solution into Eq.(28), the stream function can be expressed in spherical coordinates r, θ in terms only of $E_n^{(2)}$ and $F_n^{(2)}$:

$$\Psi^{(2)}(r,\theta)=\Psi_{\infty}(r,\theta)+\sum_{n=2}^{\infty}[E_n^{(2)}S_n^1(r,\theta)+F_n^{(2)}S_n^2(r,\theta)] \tag{33}$$

where the functions S_n^q are given in the Appendix.

Four unknown constants remain to be determined, $E_n^{(1)}$, $F_n^{(1)}$, $E_n^{(2)}$ and $F_n^{(2)}$. Of the two pertaining to the solution for the drop stream function, one constant can be expressed in terms of the other by the condition that $V_r^{(1)}(r=1,\theta)=0$. Eliminating $F_n^{(1)}$ in this manner, the inner solution can be expressed as:

$$\Psi^{(1)}(r,\theta)=\sum_{n=2}^{\infty}E_n^{(1)}(r^n-r^{n+2})C_n^{-1/2}(\cos\theta) \tag{34}$$

By using the remaining hydrodynamic boundary conditions on the sphere surface, three simultaneous equations are obtained:

$$\begin{aligned}
-U\cos\theta &= \sum_{n=2}^{\infty}[E_n^{(2)}S_n^3(1,\theta)+F_n^{(2)}S_n^4(1,\theta)\\
-U\sin\theta &= \sum_{n=2}^{\infty}[E_n^{(2)}S_n^5(1,\theta)+F_n^{(2)}S_n^6(1,\theta)+\frac{2}{\sin\theta}E_n^{(1)}C_n^{-1/2}(\cos\theta)]\\
-U\sin\theta+(2+k)(1+\frac{2}{3}\kappa)\frac{\partial\Theta}{\partial\theta}(1,\theta) &= \sum_{n=2}^{\infty}[E_n^{(2)}S_n^7(1,\theta)+F_n^{(2)}S_n^8(1,\theta)\\
&\quad -\frac{2(2n-1)\kappa}{\sin\theta}E_n^{(1)}C_n^{-1/2}(\cos\theta)]
\end{aligned} \tag{35}$$

The above equation set contains the remaining three infinite series of unknown constants, $E_n^{(2)}$, $F_n^{(2)}$ and $E_n^{(1)}$. Solutions for these constants from

the above three equations is obtained by the same collocation procedure used for the temperature field, but there are a few important differences. Since the inhomogeneity in the above three equations consists of two separate terms, one a multiple of U and one a multiple of the fluid particle surface temperature gradient, the solutions for the constants may be decomposed into separate terms, one in which $(\partial\Theta/\partial\theta)(1,\theta)=0$ and U is non-zero, and one in which U=0 and the temperature gradient is non-zero. This decomposition reflects the linearity of the Stokes equations and boundary conditions. It also allows for the interpretation of the fluid particle movement due to the temperature gradient as the sum of two flow idealizations in the fluid particle fixed frame, one in which the temperature gradient is equal to zero and a uniform flow from infinity moves over the fluid particle (U not equal to zero), and second idealization in which the flow at infinity is zero, and a temperature gradient produces fluid streaming.

The values for the constants for the first case of uniform flow are linear in U, and may therefore be solved generally by setting U=1. These constants are denoted with a "U" subscript. As before, a collocation solution procedure is developed in which the above three equations are satisfied at P points on the first quadrant, the infinite series are truncated at n=2P, and the 3P constants are obtained from the algebraic solution of the satisfaction of the three boundary conditions at P collocation points. The convergence criteria is formulated in the following way. It will be shown in the next section that (i) the terminal velocity is determined by the sum of the hydrodynamic forces exerted by the continuous phase on the fluid particle in the two flow idealizations, and (ii) this force is only dependent on $F_2^{(2)}$.

Since the aim of the study is the accurate computation of the terminal velocity, the convergence criteria is based on the accurate resolution of $F_2^{(2)}$. Thus the constant $F_{2U}^{(2)}$ is computed for P-1 and P collocation points, and the relative change in the constant is then obtained. The collocation number is incremented until the relative change is less than 10^{-5}. Listed on the second line of table 1 are the values of P necessary for convergence for κ=0 as a function of a'/b'. The table indicates that the number of collocation points increases as the sphere to tube diameter increases. Although the hydrodynamic flow patterns will be examined carefully in the results section to follow, this trend is clearly a consequence of the fact that large θ-gradients in $V_\theta^{(2)}$ develop in the gap as a'/b' increases in order to keep the overall flow rate in the z-direction constant, and more terms in the series expansion are necessary to describe accurately these gradients.

In the second flow idealization, the fluid at infinity is at rest, and flow is only caused by the temperature gradient. Again using a collocation procedure for numerical solution, the constants are determined by truncating the infinite series at L terms and satisfying the three boundary conditions at L discrete points. (These constants are identified by an "M" subscript.) Convergence is based on the accurate determination of $F_{2M}^{(2)}$, and the number of collocation points L necessary to achieve a 10^{-5} resolution in this constant are given in the third line of table 1 for κ=0 and k=1.0×10^{-5}. The table shows that more collocation points are necessary as the sphere to tube diameter increases. As will become clearer below, this trend results from the fact that the fluid streaming due to the Marangoni force creates recirculating eddies between the sphere and the tube wall,

and as a'/b' increases these eddies are squeezed and large θ gradients develop which necessitate more terms in the series expansion.

III.3. Results and Discussion

III.3.1 *Temperature Field*

Three separate presentations are given to illustrate the results for the nondimensional temperature field $\Theta^{(i)}(\rho,z)$, and the dependence of this field on the thermal conductivity and fluid particle to tube diameter ratios k and a'/b'. In the first presentation the temperature field isotherms are detailed. These are shown for the infinite system (a'/b'=0) in Figs.2(a) ($k=1.0\times10^{-5}$) and 2(b) (k=5), for a'/b'=0.5 in Figs. 3(a) ($k=1.0\times10^{-5}$) and 3(b) (k=5) and for a'/b'=0.9 in Figs.4(a) ($k=1.0\times10^{-5}$) and 4(b) (k=5). The thermocapillary velocity is determined by the magnitude of the surface temperature gradient, $(\partial\Theta/\partial\theta)(r=1,\theta)$. The final two presentations quantify this gradient by providing two different measures of $(\partial\Theta/\partial\theta)(r=1,\theta)$. In Figs.5 (for a'/b'=0.5) and 6 (a'/b'=0.9), $(\partial\Theta/\partial\theta)(r=1,\theta)$ is plotted, as a function of θ, for different values of k. To facilitate comparison with the surface temperature gradient for an infinite continuous phase, plotted alongside the tube results in Figs.5 and 6 are the infinite system gradients for the same value of k. In the second measure, the overall change in the surface temperature of a bounded droplet relative to the unbounded one is computed. This ratio is defined by Φ, and is given by:

$$\Phi = (\Theta(r=1,\theta=0) - \Theta(r=1,\theta=\pi))(2+k)/6 \tag{36}$$

where, for the case of an infinite continuous phase, the difference between the temperatures at the two poles is given by 6/(2+k), and is obtained from the surface temperature distribution

$$\frac{\partial\Theta}{\partial\theta}(r=1,\theta,\frac{a'}{b'}=0) = -\frac{3}{2+k}\sin\theta \tag{37}$$

In Fig.7, Φ is plotted as a function of a'/b' for different values of k.

Physical interpretation and discussion of the temperature results as given in Figs.2-7 begins with the examination of the influence of the thermal conductivity ratio k. For the infinite system, if the conductivity ratio becomes just less than one, there is less resistance to conduction in the continuous phase, and a greater proportion of the energy is conducted through the suspending phase. As a consequence of this heat flow pattern, the temperature isotherms beginning at $\rho\rightarrow\infty$ and perpendicular to the z-axis bend towards the sphere (Fig.2a). Therefore, relative to the case of k=1 which represents a linear temperature field, the temperature difference between the poles and the temperature gradient along the sphere surface is increased (cf. the dotted lines in Figs.5 and 6). As k decreases further from one, the temperature gradient and difference in pole temperatures continues to increase, as more heat is transported around the sphere. In the limit in which the conductivity of the sphere becomes equal to zero, all energy is conducted around the sphere and the isotherms intersect the fluid

particle surface at right angles. The behavior is reversed when k becomes just larger than one. A greater proportion of the energy is now transported through the sphere. The temperature isotherms starting at infinity bend away from the sphere (Fig.2b) and the pole temperature difference and surface temperature gradient are decreased relative to k=1 (Figs.5 and 6). As k increases further from one, the temperature difference between the poles decreases, and the gradient along the surface is uniformly reduced. In the limit in which the sphere becomes infinitely conducting, the sphere surface becomes an isotherm and only the equatorial plane isotherm intersects the sphere surface. In this case, as is evident from Eq.(37), the temperature gradient becomes equal to zero.

In the confined geometry, (Figs.3 and 4) the effect of the conductivity ratio is similar to the behavior explained above for an infinite expanse of a continuous phase. As is evident from Figs.3(a) and 4(a) for a non-conducting sphere ($k=1.0\times10^{-5}$), isotherms (now originating at the tube wall and perpendicular to it) bend towards the sphere to allow the heat to be transported through the more conductive continuous phase. Again as k decreases from one, the temperature gradient along the surface increases relative to the k=1 distribution, and this is clearly shown in Figs.5 and 6 for a'/b'=0.5 and 0.9, respectively. The more important point is how this increase in surface gradient compares with that realized for the infinite case. Figs.5 and 6 indicate that as k decreases, the temperature gradient for the confined geometry increases more rapidly than the gradient for the infinite case. Thus for any particular value of k<1, the surface temperature gradient is larger for the fluid particle in the tube than in an infinite amount

of fluid. This central conclusion can be shown more clearly in terms of the Φ, the quotient in pole temperature differences. As detailed in Fig.7, Φ increases as k decreases from one.

The reason why, for k less than one, the surface temperature gradients larger in the tube than in an infinite medium can be understood very simply. Consider the isotherms for the infinite system Fig.2(a), and superimpose onto this isotherm plot, a conceptual volume consisting of a tube of radius b' (>a') closed at both ends and placed with its centerline coincident with the z-axis of the infinite system coordinates. The ends of the tube are located at a sufficiently large distance from the sphere so that at these ends the temperature gradient is unperturbed by the sphere and is therefore in the z-direction with magnitude $(\nabla' T')_\infty$. For z>>0, the surface which closes the tube is denoted by A_1. The amount of energy entering through A_1 is equal to $k^{(2)}(\nabla' T')_\infty \pi b'^2$. As Fig.2(a) indicates for k<1, since the energy is transported around the sphere, there is a net flux of energy out of the inscribed boundary for the region above the equatorial plane. For the case of conduction in a tube, since the cylindrical portion of the tube boundary is insulated, no such heat loss occurs, yet the heat entering the tube is again $k^{(2)}(\nabla' T')_\infty \pi b'^2$. Consequently, for any cross sectional area A_2 above the equatorial plane, the energy conducted through A_2 must be larger in the tube than in the infinite geometry, and therefore the area averaged temperature gradient in the z-direction must be larger in the case of the tube. This increase in the z-component of the temperature gradient in the tube relative to that in an infinite medium accounts for the relative increase in the temperature gradient on the fluid particle surface.

For the opposite case of k>1, the isotherms of the finite system originating from and perpendicular to the tube wall bend away from the sphere (Figs.3(b) and 4(b)) so that a greater proportion of energy is conducted through the less resistive sphere. As k increases from one, the temperature gradient along the surface decreases and this is shown in Figs.5 and 6. This behavior of course is qualitatively the same as that of the infinite system as described above. However, Figs.5 and 6 show that for k>1, the temperature gradient in the tube is reduced more than it is in the infinite system as k increases. This marked reduction, as k increases from one, in the Marangoni driving force compared to that realized in the infinite system is clearly evident in the graph of Φ, Fig.7.

The reason why, for k>1, the temperature gradients along the surface of the sphere are less in the tube than in the infinite system can again be understood using control volume arguments. Specifically, consider the tube of radius b' superimposed on the isotherm contour diagram for the infinite system for k>1 (Fig.2(b)). The enclosing top surface of the tube is again denoted by A_1 and a representative cross sectional area above the equator is identified by A_2. Energy is now conducted into the superimposed tube region for the infinite system case since the isotherms bend away from the sphere enabling more energy to pass through the sphere. Therefore the energy flux through A_2 must be larger in the infinite case than in the tube case because no energy can pass through the tube wall in the tube case. The temperature gradient in the z-direction is correspondingly greater, and this explains why the temperature gradient along the surface is larger in the infinite case.

The last result to comment upon is the dependence of the isotherm contours and the surface temperature gradients on the sphere to tube diameter ratio. For k fixed and less than one, as b'/a' decreases, the isotherm contours of Figs.2(a), 3(a), and 4(a) establish that the temperature gradient along the surface increases. When k>1, the opposite behavior is obtained. These results follow for the same reasons that for k<1 the surface temperature gradient is larger in the tube than in an infinite system, while for k>1 the gradient is smaller.

To summarize the results for the temperature gradient along the surface: When k<1, energy is conducted around the sphere. The surface gradient for a fluid particle in a tube is larger than the gradient on the surface of a fluid particle in an infinite medium, and this difference increases as b'/a' decreases. For k>1, a greater proportion of the energy is transported through the particle. The surface gradient on the fluid particle surface is less than the gradient developed when the fluid particle is in an infinite medium, and the absolute value of this difference increases as b'/a' decreases.

III.3.2 *Hydrodynamic Forces*

The hydrodynamic force in the z-direction (F'_z) exerted by the exterior fluid on the drop or bubble is obtained by integrating the viscous traction and pressure forces over the fluid particle surface. The force may be expressed in the following form (Happel and Brenner, 1973):

$$F_z' = 4\pi a' \mu'^{(2)} U_o' F_2^{(2)} \tag{38}$$

where the constant $F_2^{(2)}$ is obtained as part of the solution of the system of equations as given in Eq.(35). As outlined in the previous section, the flow and therefore the hydrodynamic forces exerted on the fluid particle may be considered to be composed of the sum from two flow idealizations, one in which the temperature gradient is equal to zero, and the wall is moving creating a flow which drags against the particle, and a second idealization in which the wall is stationary and a Marangoni stress gives rise to fluid motion and a resulting lift force. The forces from each of these flow idealizations are discussed separately below.

Consider first the drag exerted on the particle by the exterior flow caused by the movement of the wall only. This idealization is described by Eq.(35) with the temperature gradient set equal to zero, and the dimensional drag is given by

$$F_{zu}' = 4\pi a' \mu'^{(2)} U_o' F_{2U}^{(2)} U \tag{39}$$

The constant $F_{2U}^{(2)}$ is obtained by the collocation procedure and is tabulated in terms of a drag coefficient λ_u which is defined as the ratio of the drag on the fluid particle in this idealization to the drag exerted by the particle in an infinite medium with uniform flow of the same magnitude, U'. This latter drag is equal to $-4\pi a' U' \mu'^{(2)}(1+3\kappa/2)/(1+\kappa)$ (cf. for example, Happel & Brenner 1973) and therefore the drag coefficient is defined by:

$$\lambda_u = -F_{2U}^{(2)}(1+\kappa)/(1+3\kappa/2) \tag{40}$$

In the second problem, the wall is stationary and the Marangoni force causes fluid streaming and an associated lift force. This idealization is described by Eq.(35) with U=0, and the drag is given by:

$$\begin{aligned} F_{zm}^{'} &= 4\pi a' \mu'^{(2)} U_o^{'} F_{2M}^{(2)} \\ &= 4\pi a'^2 F_{2M}^{(2)} \left(-\frac{\partial \sigma'}{\partial T'} \right) (\nabla' T')_\infty / ((1+\frac{3}{2}\kappa)(2+k)) \end{aligned} \tag{41}$$

The lift coefficient λ_m is defined as the ratio of this force F'_{zm} exerted on the sphere in the tube divided by the lift force exerted on the sphere in an infinite, stationary, medium due to the fluid streaming arising from a Marangoni force derived from an equal temperature gradient. The force in the infinite medium is equal to $4\pi a'^2 (-\partial\sigma'/\partial T')(\nabla' T')_\infty / ((1+\kappa)(2+k))$. (Note that this lift force is balanced by the drag, $-4\pi a' U_o^{'} \mu'^{(2)} (1+3\kappa/2)/(1+\kappa)$, which is due to the forward motion of the particle, and (1) in fact follows easily by summing these forces to zero.) the lift coefficient λ_m defined as the quotient of the actual Marangoni lift exerted in the tube divided by the lift in an infinite medium, is therefore given by:

$$\lambda_m = \frac{F_{2M}^{(2)}(1+\kappa)}{(1+3\kappa/2)} \tag{42}$$

The calculations were checked by comparing values obtained for the drag coefficients to known values for certain limiting situations. Three

verifications were done: First, the values for λ_u as a function of a'/b' for a solid sphere (implemented here by setting $\kappa=10^8$) were compared with the results of Haberman and Sayre (1958) and Wang and Skalak (1969) assuming a priori solid spheres (i.e. using the no-slip condition). This comparison is given in table 2, and it can clearly be seen that the coefficients obtained in this study are within one percent of those from the past studies. Additional verification of the λ_u calculations is obtained by comparing the results for a fluid sphere to those of Hyman and Skalak (1972a) (table 3). This comparison is shown in table 3 for values of κ =0 and 1 (the only two values studied by Hyman and Skalak); again the agreement is excellent. No previous studies have computed λ_m, and therefore the only way of checking these results is to verify that they properly converge towards one for all κ and k as a'/b'$\rightarrow$0. This behavior will be evident in the graphs to be presented below.

Converged values for λ_u are plotted in Fig.8, for respectively κ=0, 0.5, 1.0, 2.0, and 10^8(solid sphere) and for a range of a'/b' between 0 and 0.9. Figure 8 shows several interesting features. The figure indicates that λ_u increases as a'/b' increases for fixed κ. The dimensional drag (F'_{zu}) in terms of this drag coefficient is equal to $-4\pi a' \mu'^{(2)} ((1+3\kappa/2)/(1+\kappa))\lambda_u U'$ and it represents the force exerted on a fixed sphere with the wall moving with a velocity U'. It can be concluded from Fig.8 and the expression for F'_{zu} that for fixed viscosity and sphere diameter, the drag increases as the tube radius decreases. This increase in drag is due to the hydrodynamic interaction of the sphere with the wall: as the gap between the sphere perimeter and the tube wall decreases, the

shear rate in the gap in the vicinity of the sphere increases. The sphere suffers a higher shear stress applied by the fluid, therefore the drag consequently increases. Also evident from Fig.8 is the fact that the drag coefficient increases with κ at fixed a'/b'. As a physical example, increasing κ can be realized by varying the droplet viscosity with the continuous phase viscosity and the tube and fluid particle diameters held constant. For that case, the dimensional drag also increases since the factor $(1+3\kappa/2)/(1+k)$ monotonically increases with κ along with λ_u. The reason for the increase in dimensional drag is also clear; as the droplet viscosity increases, the sphere surface velocity decreases and this causes the shear rate in the vicinity of the sphere to increase, thereby increasing the drag coefficient.

The converged results for λ_m as a function of a'/b' are detailed graphically in Fig.9 for different values of the conductivity ratio k and κ=0, and in Fig.10 for different values of the viscosity ratio κ and $k=1.0\times10^{-5}$. Consider first the dependence on k, Fig.9, and note the behavior for k=1. For equal thermal conductivity, Fig.9 indicates that λ_m is larger than one, and increases with a'/b'. Recall that when k=1, the surface temperature gradient is identical to that for the infinite case, and is therefore independent of a'/b'. Thus the fact that the lift forces in the tube case become increasingly larger than those in the infinite case cannot be due to an increase in the surface Marangoni force. The reason for this behavior may be attributed to the pressure differential which develops across the sphere. In the flow idealization which defines λ_m, the surface force drives, in the continuous phase, a streaming flow in the vicinity of the fluid particle interface in the negative z-direction. Since the wall is stationary, and the

fluid at infinity is at rest, the net flow rate for this streaming flow in the z-direction must be equal to zero. Therefore downstream from the particle, pressure forces develop to turn the fluid around. As this pressure force acts in the positive z-direction it provides, along with the reaction to the surface Marangoni force, the lift which propels the droplet in the positive z-direction. As the tube diameter decreases, for a constant Marangoni force, the surface velocity and therefore the magnitude of the streaming flow decreases. However, the pressure force which drives the recirculation does not decrease because it must drive fluid through an increasingly smaller gap between the fluid particle and the tube surface. This fact is over-riding, and causes the pressure to increase as the tube diameter decreases. This increase in pressure manifests itself as an increase in the lift force, and explains why λ_m is larger than one for k=1, and increases with a'/b'.

Consider next the dependence of λ_m on the conductivity ratio k. Figure 9 shows that as k decreases from one, λ_m increases and as k increases from one, λ_m decreases. This effect can be understood completely in terms of the influence of k (at fixed a'/b') on the surface temperature gradient as discussed in Sec.3.1 (cf. Figs.5-7): as k decreases from one, the surface temperature gradient in the tube geometry becomes increasingly larger than that which develops on a fluid particle in an infinite medium, and therefore λ_m, which is the ratio of the lift forces in the tube and infinite geometry, increases. Similarly, as k increases from one, the surface temperature gradient for the particle in a tube decreases relative to the infinite medium value, and λ_m decreases. Note finally that since the dimensional lift force, F'_{zm} is equal to

$-4\pi a'^2(\partial\sigma'/\partial T')(\nabla' T')_\infty \lambda_m/((1+\kappa)(2+k))$, for fixed fluid viscosity and sphere and tube diameters, the dimensional drag increases as k decreases.

Consider next the dependence of λ_m on a'/b' for k not equal to one. Figure 9 shows that for all k, λ_m increases with a'/b'. Significantly, this increase is enhanced as k decreases. Reasons for this behavior may be attributed to two effects, the back pressure which develops to recirculate the fluid and which increases with a'/b', and the influence of a'/b' on the surface temperature gradient (Fig.7). When k<1, the surface temperature gradient increases as a'/b' increases. This causes larger Marangoni stresses which act to increase the lift force. In addition, the back pressure increases because the gap thickness decreases. Thus λ_m should increase rapidly. For k<1, these two influences have opposite effects. Although the back pressure increases with a'/b', the surface Marangoni force decreases (Fig.7). However as was the case with k=1, the effect of the decreasing gap size on the back pressure is dominant, and λ_m slowly increases with a'/b'.

The dependence of λ_m on the fluid viscosity ratio κ is given in Fig.10, and this figure indicates that for a fixed a'/b', λ_m increases with κ. To understand this dependence, consider first how the dimensional lift force behaves with κ for a fixed continuous phase viscosity and fluid particle radius a'. The dimensional lift (F'_{zm}) is plotted in Fig.11, for $k=1.0\times10^{-5}$ as a function of κ, divided by the lift for the same a'/b' and $\kappa=0$. This quotient, which is equal to $\lambda_m(\kappa,\ k=1.0\times10^{-5},\ a'/b')/\lambda_m\ (\kappa=0,\ k=1.0\times10^{-5},\ a'/b')$ is defined as Ψ. Figure 11 indicates that as κ increases, Ψ and consequently the dimensional drag decreases. As κ increases, the velocity on the surface

owing to the Marangoni force (which is independent of κ) decreases, and this causes the lift force to decrease. Reconsider Fig.10: Mathematically, the reason why λ_m increases with κ at fixed a'/b' is that, as is evident in Fig.11 (for $k=1.0\times10^{-5}$), the dimensional lift in the tube does not decrease as fast with κ as that for an infinite medium (the latter varies as $(1+\kappa)^{-1}$, and corresponds to the curve labeled $a'/b'=10^{-3}$ in Fig.11). Physically, this behavior reflects the fact that in the infinite medium at finite κ, the droplet stress which retards the surface force is a larger percentage of the total retarding force (outside and inside) than it is in the confined geometry. The reason for this is that the length scale for the relaxation in the velocity in the unbounded geometry is much larger than in the confined one. When the interior viscosity is increased, the droplet stress is increased, and to maintain a constant surface force, a reduction in the surface velocity (relative to its previous value) is necessary. This reduction is larger in the unbounded than in the bounded case since the droplet stress is a larger component of the total retarding shear stress. Thus the proportional change in the drag is more for the unbounded case, and λ_m increases with κ.

III.3.3 *Terminal Velocities*

The total drag on the fluid particle ($F'_{zu} + F'_{zm}$) is equal to zero. This requirement allows the fluid particle velocity U' to be computed; using Eqs.(39)-(42), U' may be expressed relative to the speed in an infinite medium (U') through the drag and lift coefficients λ_u and λ_m:

$$\frac{U'}{U_o'} = \frac{\lambda_m}{\lambda_u} \tag{43}$$

This equation clearly illustrates the competing effects which determine the relative speed: The enhancement of the Marangoni lift force relative to the infinite value, λ_m (Figs.9 and 10), acts to increase the relative speed, while the enlargement (relative to the infinite system) of the drag force owing to the forward motion, λ_u (Fig.8), retards the relative speed. The result of these competing effects is shown in Figs.12(a) and 12(b) which graph U'/U'_o as a function of a'/b' for different values of k (Fig.12(a)) and κ (Fig. 12(b)). The principal observation from these graphs is that U'/U'_o is always less than one, and is a monotonically decreasing function of a'/b' for all values of the conductivity and viscosity ratios. Hence, with increasing a'/b', the increased drag due to the hydrodynamic interaction of the fluid particle with the tube wall dominates the increase in the Marangoni lift force, and the fluid particle in the tube always moves slower than it does in an infinite medium. At a fixed ratio of the diameter of the fluid particle to that of the tube, the dependence of U'/U'_o on k and κ follows directly from the dependencies of λ_m and λ_u on these variables. Consider first the behavior with k: The drag coefficient λ_u is independent of k. The Marangoni lift coefficient, λ_m, increases with decreasing k as a greater proportion of the energy from infinity circumvents the fluid article and creates a high surface temperature gradient allowing the energy to pass through the narrow gap. Therefore, as indicated in Fig.10, the relative speed increases with decreasing k. The dependence of U'/U'_o on κ at fixed a'/b' and k is more

complicated. In this case, although both λ_m and λ_u increase with κ, comparison of Figs.8 and 10 indicate that the effect of the viscosity ratio on λ_m is greater than that on λ_u. Hence, as demonstrated in Fig.12(b), the relative velocity increases as the viscosity of the fluid particle becomes larger than that of the continuous phase.

III.4. Conclusions

This paper has examined the steady, creeping, thermocapillary migration of a spherical fluid particle in a tube owing to an imposed axial temperature gradient under conditions of axisymmetry, negligible thermal convection and an insulated tube wall. As outlined in the introduction, the intention of this study is to use this flow geometry as a model for understanding the influence of lateral wall-fluid particle hydrodynamic and thermal interactions in determining the thermocapillary migration velocity.

In this Stokes problem, the force of the continuous phase on the fluid particle can be divided into the forces from two fixed- fluid particle flow idealizations, one in which the tube wall is moving dragging fluid over the stationary fluid particle with no Marangoni force, and a second idealization in which the wall is fixed and the surface temperature gradient drives a streaming, recirculating motion that propels the fluid particle towards the warmer fluid. The dragging force is described by a drag coefficient λ_u, and the thermocapillary lift or propulsion force is described by a lift coefficient λ_m. Each of these coefficients represents the ratio of the force in the idealization in the confined tube geometry divided by that in an infinite

medium. The first idealization and the coefficient λ_u describe the hydrodynamic resistance of the wall on the forward motion of the fluid particle. This coefficient increases sharply as the sphere to tube diameter ratio increases. The second idealization and the lift coefficient λ_m describe the thermal interaction between the wall and the fluid particle. The lift coefficient increases as the ratio of the fluid particle to the continuous phase liquid conductivity decreases since in that limit more energy is conducted through the gap between the fluid particle and the wall, and this heat flow intensifies the fluid particle surface temperature gradient. This increase is enhanced as the gap thickness decreases. The lift coefficient also describes a secondary wall-fluid particle hydrodynamic interaction apart from the resistance to forward motion as described by λ_u. Specifically, for the case in which the conductivity of the fluid particle and the continuous phase are equal, and therefore the thermal interaction is equal to zero, the lift coefficient λ_m increases as the gap distance between the fluid particle and the wall decreases. This increase is ascribed to the increase in the back pressure which drives the recirculating motion of the Marangoni flow idealization, and which propels the fluid particle towards the warmer temperature. This back pressure increases with decreasing gap thickness because a higher back pressure is necessary to drive fluid through a narrowing gap.

The ratio of λ_m to λ_u determines the migration velocity in the tube relative to that in an infinite medium. Calculations of this ratio indicate that, for a fixed gap thickness, the relative velocity increases as the fluid particle conductivity decreases, and that this increase in migration becomes more

pronounced as the gap thickness decreases. Both these results are attributable to the influence of the thermal interaction on λ_m. However for a fixed, small conductivity ratio, the relative velocity decreases as the gap thickness decreases, and this reflects the predominance of the hydrodynamic retardation of the wall on the forward motion (as described by λ_u) over the migration enhancing thermal interaction and secondary back pressure hydrodynamic interaction (as given by λ_m).

Appendix

Expressions for the G_n^k functions are given below.

$$
\begin{aligned}
G_n^1(\rho,z) &= (\rho^2+z^2)^{-\frac{1}{2}(n+1)} P_n\left[\frac{z}{(\rho^2+z^2)^{\frac{1}{2}}}\right] \\
G_n^2(\rho,z) &= (\rho^2+z^2)^{-\frac{1}{2}(n-1)}\left[P_n\left[\frac{z}{(\rho^2+z^2)^{\frac{1}{2}}}\right]+2C_n^{-\frac{1}{2}}\left[\frac{z}{(\rho^2+z^2)^{\frac{1}{2}}}\right]\right] \\
G_n^3(\rho,z) &= (\rho^2+z^2)^{-\frac{1}{2}(n-1)} C_n^{-\frac{1}{2}}\left[\frac{z}{(\rho^2+z^2)^{\frac{1}{2}}}\right] \\
G_n^4(\rho,z) &= (\rho^2+z^2)^{-\frac{1}{2}(n-3)} C_n^{-\frac{1}{2}}\left[\frac{z}{(\rho^2+z^2)^{\frac{1}{2}}}\right] \\
G_n^5(\rho,z) &= \frac{(n+1)}{\rho}(\rho^2+z^2)^{-\frac{1}{2}n} C_{n+1}^{-\frac{1}{2}}\left[\frac{z}{(\rho^2+z^2)^{\frac{1}{2}}}\right] \\
G_n^6(\rho,z) &= \frac{(n+1)}{\rho}(\rho^2+z^2)^{-\frac{1}{2}(n-2)} C_{n+1}^{-\frac{1}{2}}\left[\frac{z}{(\rho^2+z^2)^{\frac{1}{2}}}\right] - \\
&\quad -\frac{2z}{\rho}(\rho^2+z^2)^{-\frac{1}{2}(n-1)} C_n^{-\frac{1}{2}}\left[\frac{z}{(\rho^2+z^2)^{\frac{1}{2}}}\right]
\end{aligned}
\tag{A.1}
$$

Expressions for the terms H_n^i are given below.

$$
\begin{aligned}
H_n^1(t) &= (-1)^{\frac{1}{2}n}\frac{2}{\pi n!}t^n K_0(Rt) \\
H_n^2(t) &= -(-1)^{\frac{1}{2}n}\frac{2}{\pi n!}t^{n-2}[n(n-1)K_0(Rt)-(2n-3)RtK_1(Rt)] \\
H_n^3(t) &= -(-1)^{\frac{1}{2}n}\frac{2}{\pi n!}Rt^{n-1}K_1(Rt) \\
H_n^4(t) &= -(-1)^{\frac{1}{2}n}\frac{2}{\pi n!}Rt^{n-3}[(2n-3)RtK_0(Rt)-(n-2)(n-3)K_1(Rt)]
\end{aligned}
\qquad \text{(A.2)}
$$

The functions S_n^q are defined as:

$$
\begin{aligned}
S_n^1(r,\theta) &= r^{-n+1}C_n^{-\frac{1}{2}}(\cos\theta)+\int_o^\infty dt\cos(tr\cos\theta)[T_n^1(t)r\sin\theta I_1(tr\sin\theta) \\
&\quad +T_n^3(t)(r\sin\theta)^2 I_0(tr\sin\theta)], \\
S_n^2(r,\theta) &= r^{-n+3}C_n^{-\frac{1}{2}}(\cos\theta)+\int_o^\infty dt\cos(tr\cos\theta)[T_n^2(t)r\sin\theta I_1(tr\sin\theta) \\
&\quad +T_n^4(t)(r\sin\theta)^2 I_0(tr\sin\theta)], \\
\begin{bmatrix} S_n^3 \\ S_n^4 \end{bmatrix} &= P_{n-1}(\cos\theta)+\int_o^\infty dt\Bigg\{t\sin\theta\sin(t\cos\theta)\Bigg(\begin{bmatrix} T_n^1 \\ T_n^2 \end{bmatrix}I_1(t\sin\theta) \\
&\quad +\begin{bmatrix} T_n^3 \\ T_n^4 \end{bmatrix}\sin\theta I_0(t\sin\theta)\Bigg)+\cos\theta\cos(t\cos\theta)\Bigg(\begin{bmatrix} T_n^1 \\ T_n^2 \end{bmatrix}tI_0(t\sin\theta) \\
&\quad +\begin{bmatrix} T_n^3 \\ T_n^4 \end{bmatrix}(2I_0(t\sin\theta)+t\sin\theta I_1(t\sin\theta))\Bigg)\Bigg\},
\end{aligned}
\qquad \text{(A.3)}
$$

$$\begin{bmatrix} S_n^5 \\ S_n^6 \end{bmatrix} = \begin{bmatrix} (1-n) \\ (3-n) \end{bmatrix} \frac{C_n^{-\frac{1}{2}}(\cos\theta)}{\sin\theta} + \int_o^\infty dt \left\{ t\cos\theta \sin(t\cos\theta) \left(-\begin{bmatrix} T_n^1 \\ T_n^2 \end{bmatrix} I_1(t\sin\theta) \right.\right.$$
$$\left. - \begin{bmatrix} T_n^3 \\ T_n^4 \end{bmatrix} \sin\theta I_0(t\sin\theta) \right) + \sin\theta\cos(t\cos\theta) \left(\begin{bmatrix} T_n^1 \\ T_n^2 \end{bmatrix} t I_0(t\sin\theta) \right.$$
$$\left.\left. + \begin{bmatrix} T_n^3 \\ T_n^4 \end{bmatrix} (2I_0(t\sin\theta) + t\sin\theta I_1(t\sin\theta)) \right) \right\},$$

$$\begin{bmatrix} S_n^7 \\ S_n^8 \end{bmatrix} = \begin{bmatrix} S_n^5 \\ S_n^6 \end{bmatrix} - \begin{bmatrix} (n^2-1) \\ (3-n)(1-n) \end{bmatrix} \frac{C_n^{-\frac{1}{2}}(\cos\theta)}{\sin\theta}$$
$$- \int_o^\infty dt \left\{ \cos(t\cos\theta) \left(\begin{bmatrix} T_n^1 \\ T_n^2 \end{bmatrix} t^2 (\sin^2\theta - \cos^2\theta) I_1(t\sin\theta) \right.\right.$$
$$\left. + \begin{bmatrix} T_n^3 \\ T_n^4 \end{bmatrix} \sin\theta (t^2(\sin^2\theta - \cos^2\theta) I_0(t\sin\theta) + 2t\sin\theta I_1(t\sin\theta)) \right)$$
$$- t\cos\theta \sin(t\cos\theta) \left(\begin{bmatrix} T_n^1 \\ T_n^2 \end{bmatrix} (2t\sin\theta I_0(t\sin\theta) - I_1(t\sin\theta)) \right.$$
$$\left.\left. + \begin{bmatrix} T_n^3 \\ T_n^4 \end{bmatrix} \sin\theta (3I_0(t\sin\theta) + 2t\sin\theta I_1(t\sin\theta)) \right) \right\},$$

where the functions $T_n^i(t)$ (i=1,2,3,4) are defined as

$$T_n^1(t) = [(2 + Rt\Omega) H_n^3(t) - R^2 H_n^1(t)] / \Delta$$
$$T_n^2(t) = [(2 + Rt\Omega) H_n^4(t) - R^2 H_n^2(t)] / \Delta$$
$$T_n^3(t) = [R\Omega H_n^1(t) - t H_n^3(t)] / \Delta$$
$$T_n^4(t) = [R\Omega H_n^2(t) - t H_n^4(t)] / \Delta \qquad \text{(A.4)}$$

The variable Ω is given by $I_1(Rt)/I_0(Rt)$ and

$\Delta = R^2 t I_0(Rt) - 2R I_1(Rt) - R^2 t I_1(Rt)\Omega$

Table 1

The number of collocation points necessary to achieve the accuracy requirement for the gas bubble (κ=0 & k=1.0×10^{-5})

λ	a'/b'	0.1	0.2	0.3	0.4	0.5	0.6	0.7	0.8	0.9
	M	4	6	6	6	8	10	12	14	16
λ_u	P	4	4	5	7	7	9	10	11	13
λ_m	L	3	3	4	4	4	5	5	6	7

Table 2

Comparison of converged values of drag coefficients λ_u with the results of Haberman and Sayre (1958) and Wang and Skalak (1969) for a solid particle ($\kappa=10^8$).

		Haberman & Sayre	Wang & Skalak
a'/b'	λ_u	λ_u	λ_u
0.0	1.000	1.000	1.000
0.1	1.2632	1.263	1.263
0.2	1.6795	1.680	1.680
0.3	2.370	2.371	2.370
0.4	3.591	3.596	3.592
0.5	5.940	5.970	5.949
0.6	11.09	11.135	11.10
0.7	24.665	24.955	24.70
0.8	74.567	73.555	74.97
0.9	464.97		

Table 3

Comparison of converged values of drag coefficients λ_u with the results of Hyman and Skalak's solution (1972a) for a fluid droplet.

			Hyman & Skalak
a'/b'	k	λ_u	λ_u
0.1	0.0	1.1632	1.16
	0.5	1.1947	
	1.0	1.2111	1.211
	2.0	1.228	
0.2	0.0	1.3899	1.390
	0.5	1.4745	
	1.0	1.5209	1.520
	2.0	1.5703	
0.3	0.0	1.7251	1.725
	0.5	1.8957	
	1.0	1.9951	1.995
	2.0	2.1059	
0.4	0.0	2.2626	2.263
	0.5	2.5714	
	1.0	2.7646	2.765
	2.0	2.992	
0.5	0.0	3.2223	3.222
	0.5	3.7559	
	1.0	4.1195	4.123
	2.0	4.5767	
0.6	0.0	5.2040	5.205
	0.5	6.1157	
	1.0	6.8064	6.808
	2.0	7.7475	
0.7	0.0	10.256	10.26
	0.5	11.832	
	1.0	13.216	13.22
	2.0	15.305	
0.8	0.0	28.553	28.59
	0.5	31.252	
	1.0	34.398	34.47
	2.0	39.864	
0.9	0.0	172.81	
	0.5	173.05	
	1.0	182.19	
	2.0	203.92	

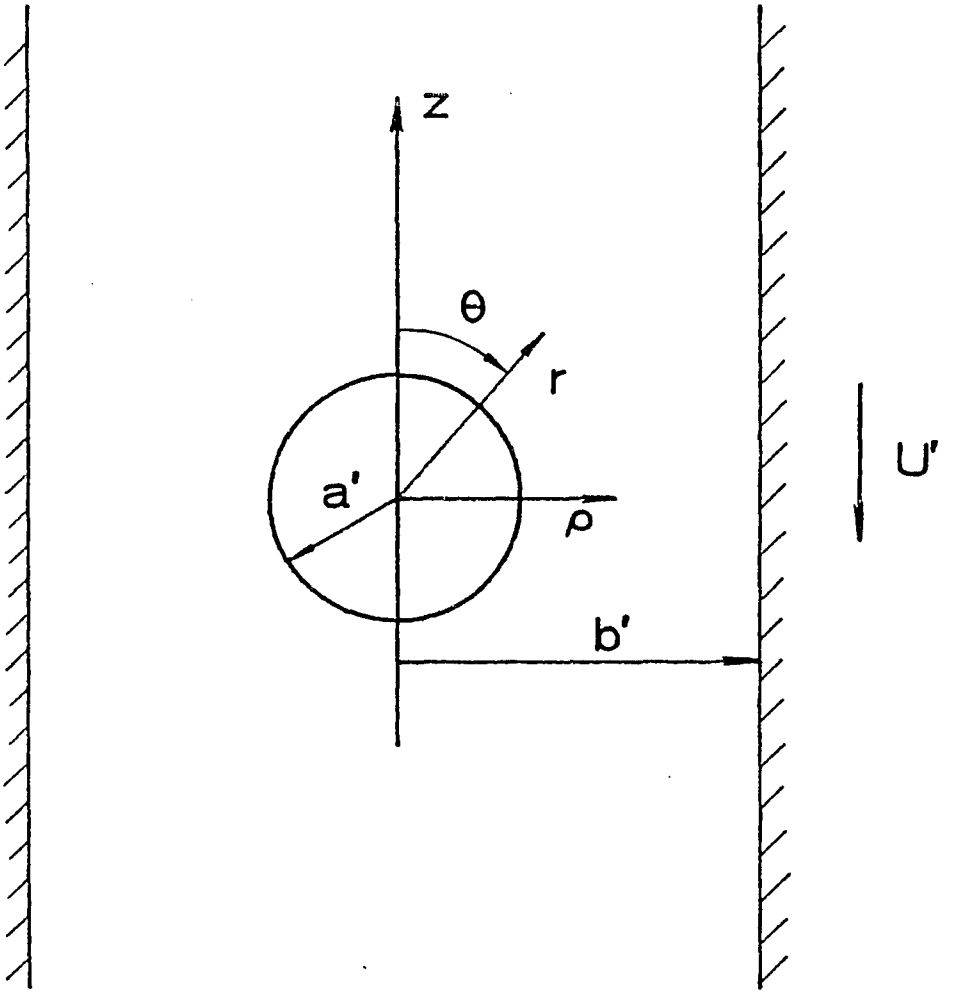

Fig.1

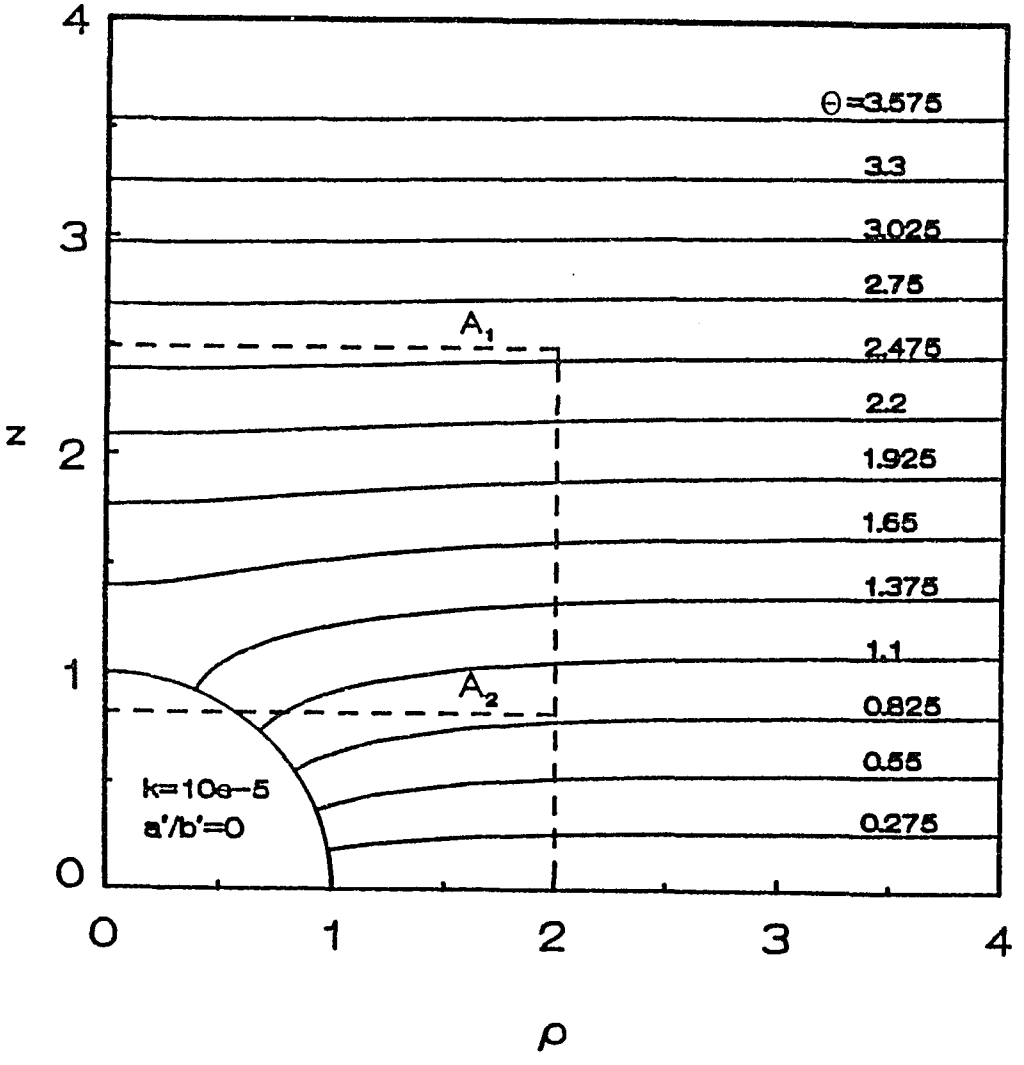
Θ=3.575
3.3
3.025
2.75
2.475
2.2
1.925
1.65
1.375
1.1
0.825
0.55
0.275
A1
A2
k=10e-5
a'/b'=0
z
ρ
0
1
2
3
4

Fig.2(a)

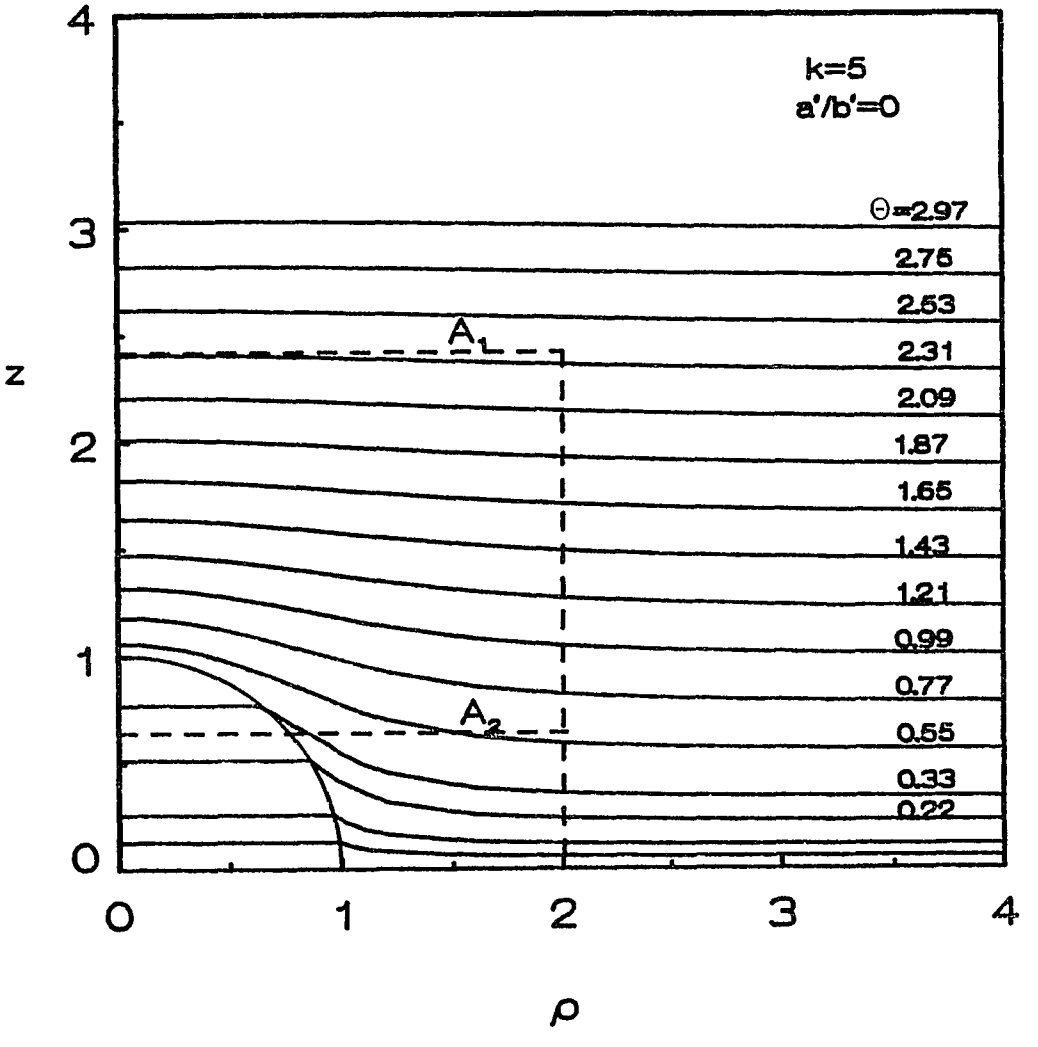
k=5
a'/b'=0
Θ=2.97
2.75
2.53
2.31
2.09
1.87
1.65
1.43
1.21
0.99
0.77
0.55
0.33
0.22
A1
A2
z
ρ
0
1
2
3
4

Fig.2(b)

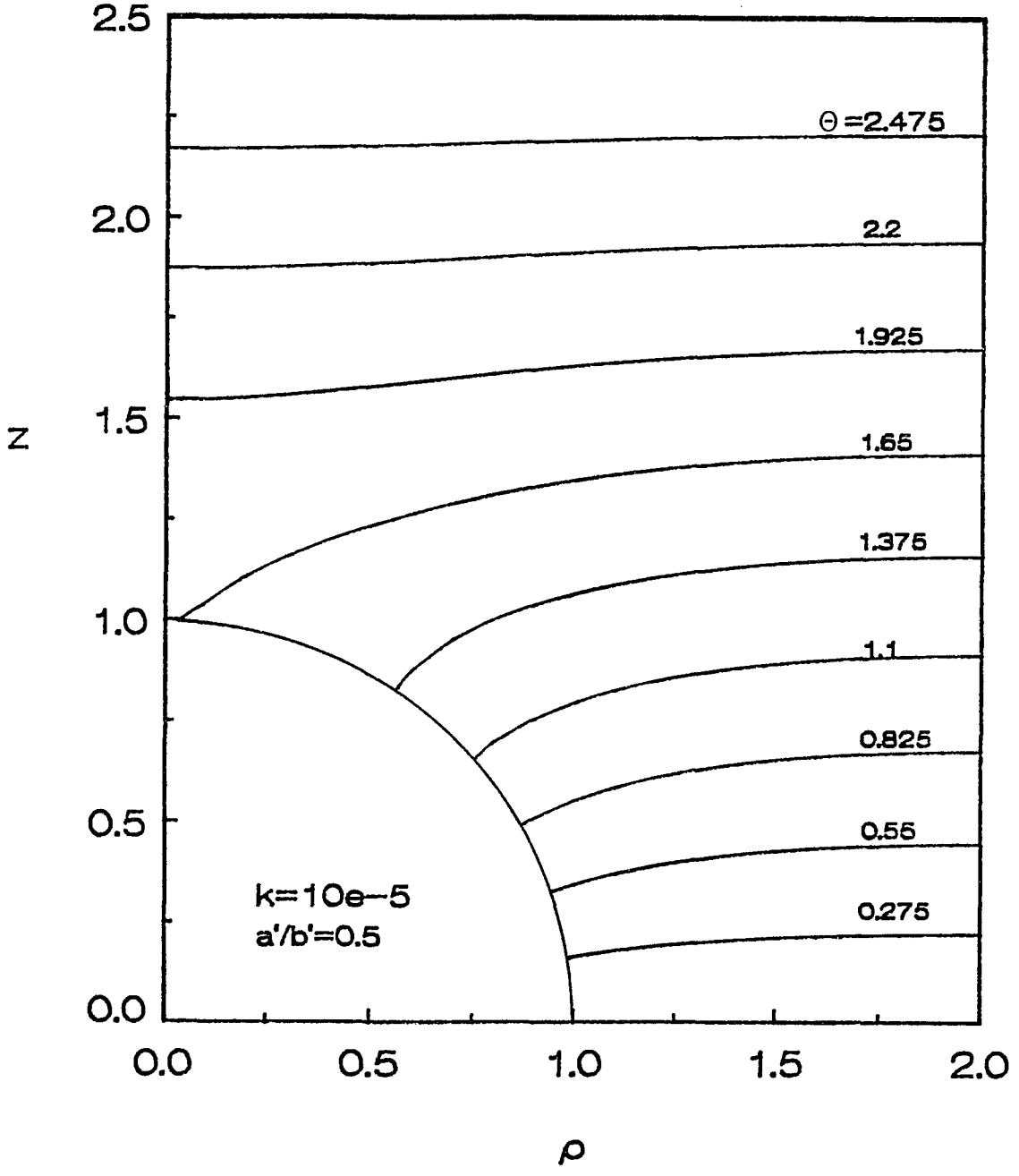
2.5
2.0
1.5
1.0
0.5
0.0
z
Θ=2.475
2.2
1.925
1.65
1.375
1.1
0.825
0.55
0.275
k=10e−5
a'/b'=0.5
0.0
0.5
1.0
1.5
2.0
ρ

Fig.3(a)

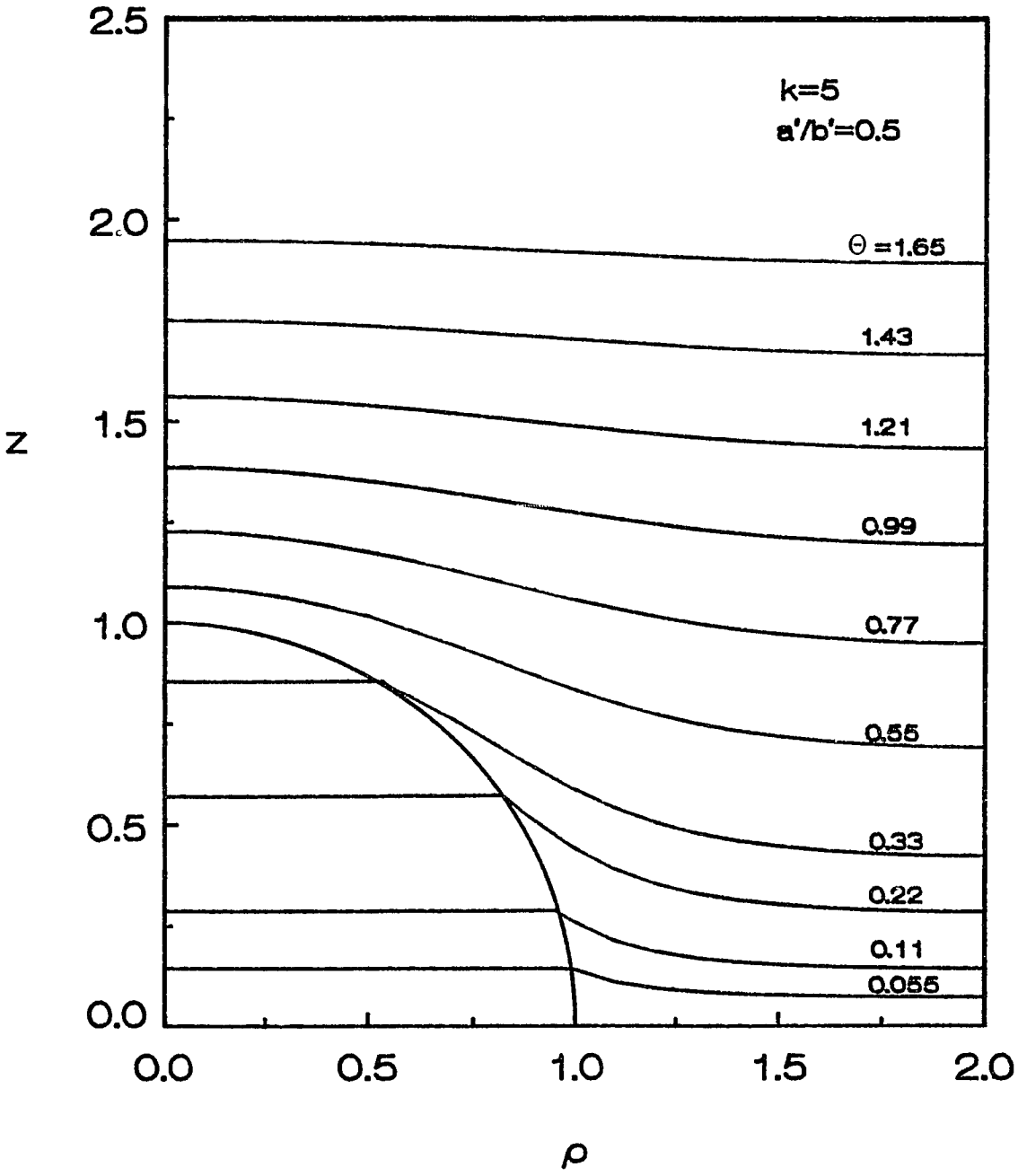
k=5
a'/b'=0.5
Θ =1.65
1.43
1.21
0.99
0.77
0.55
0.33
0.22
0.11
0.055
z
ρ
2.5
2.0
1.5
1.0
0.5
0.0
0.0
0.5
1.0
1.5
2.0

Fig.3(b)

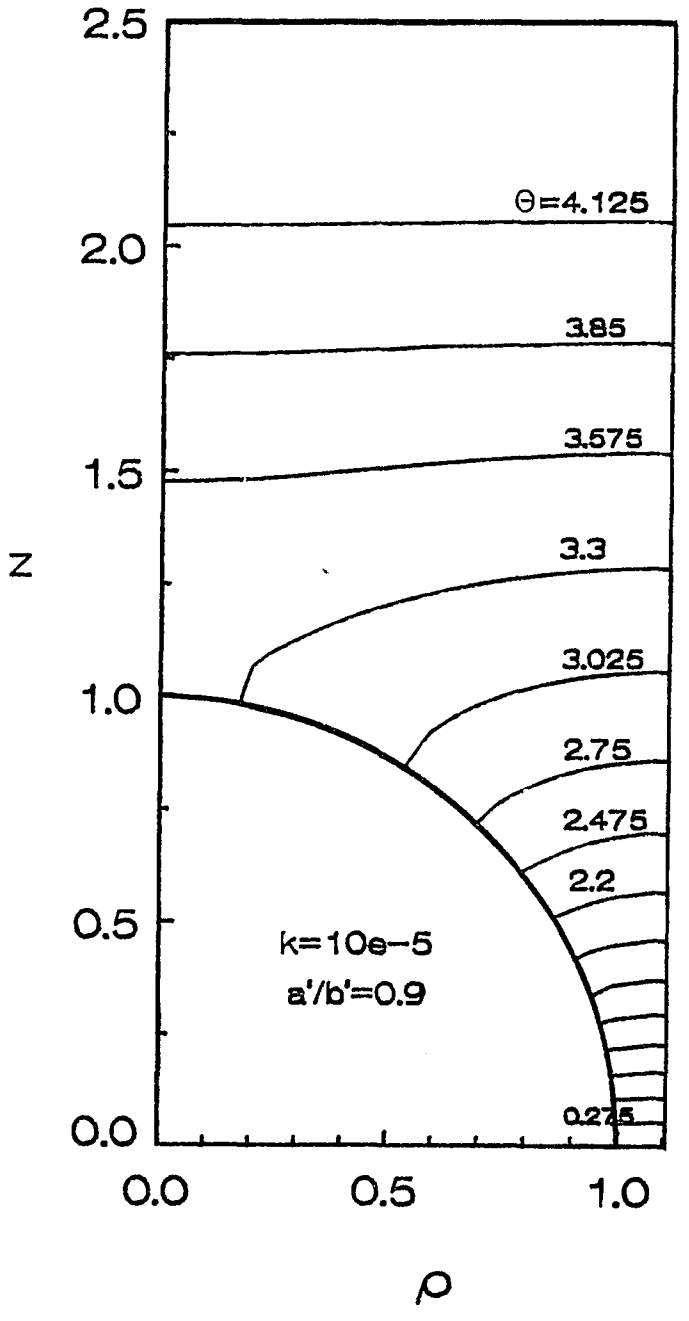
2.5
2.0
1.5
1.0
0.5
0.0
z
Θ=4.125
3.85
3.575
3.3
3.025
2.75
2.475
2.2
0.275
k=10e−5
a'/b'=0.9
0.0
0.5
1.0
ρ

Fig.4(a)

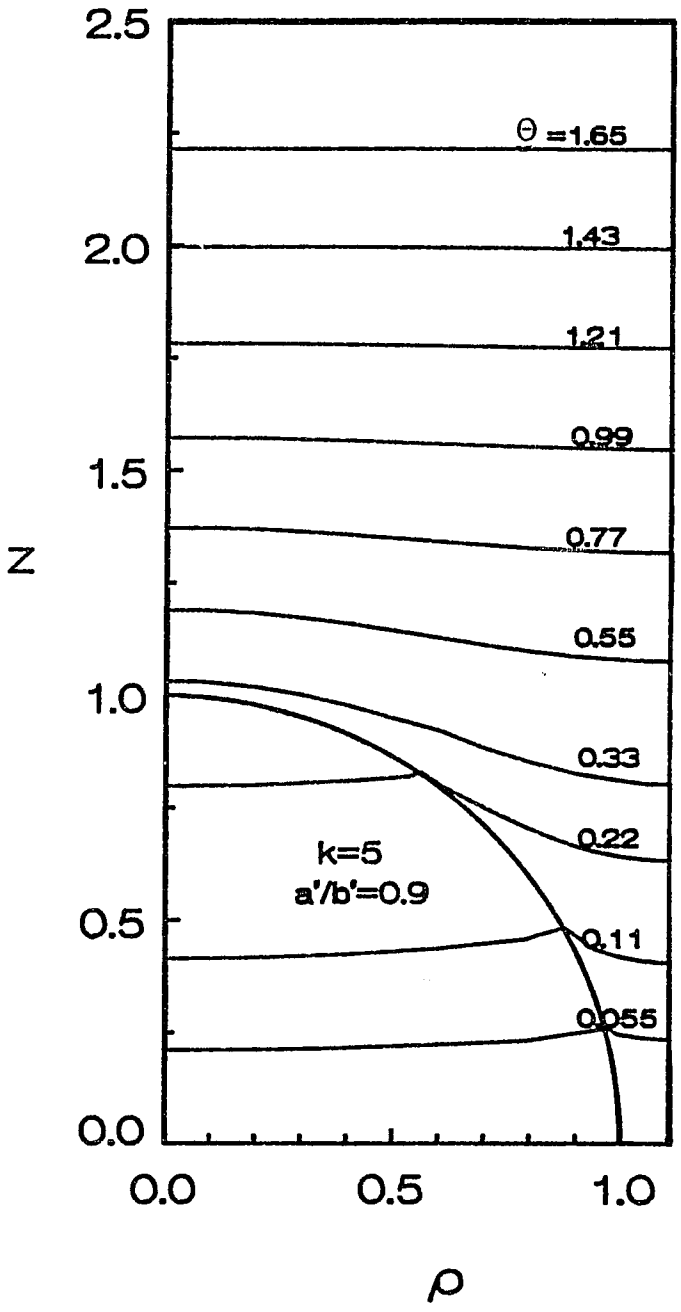
2.5
2.0
1.5
1.0
0.5
0.0
Z
Θ =1.65
1.43
1.21
0.99
0.77
0.55
0.33
0.22
0.11
0.055
k=5
a'/b'=0.9
0.0
0.5
1.0
ρ

Fig.4(b)

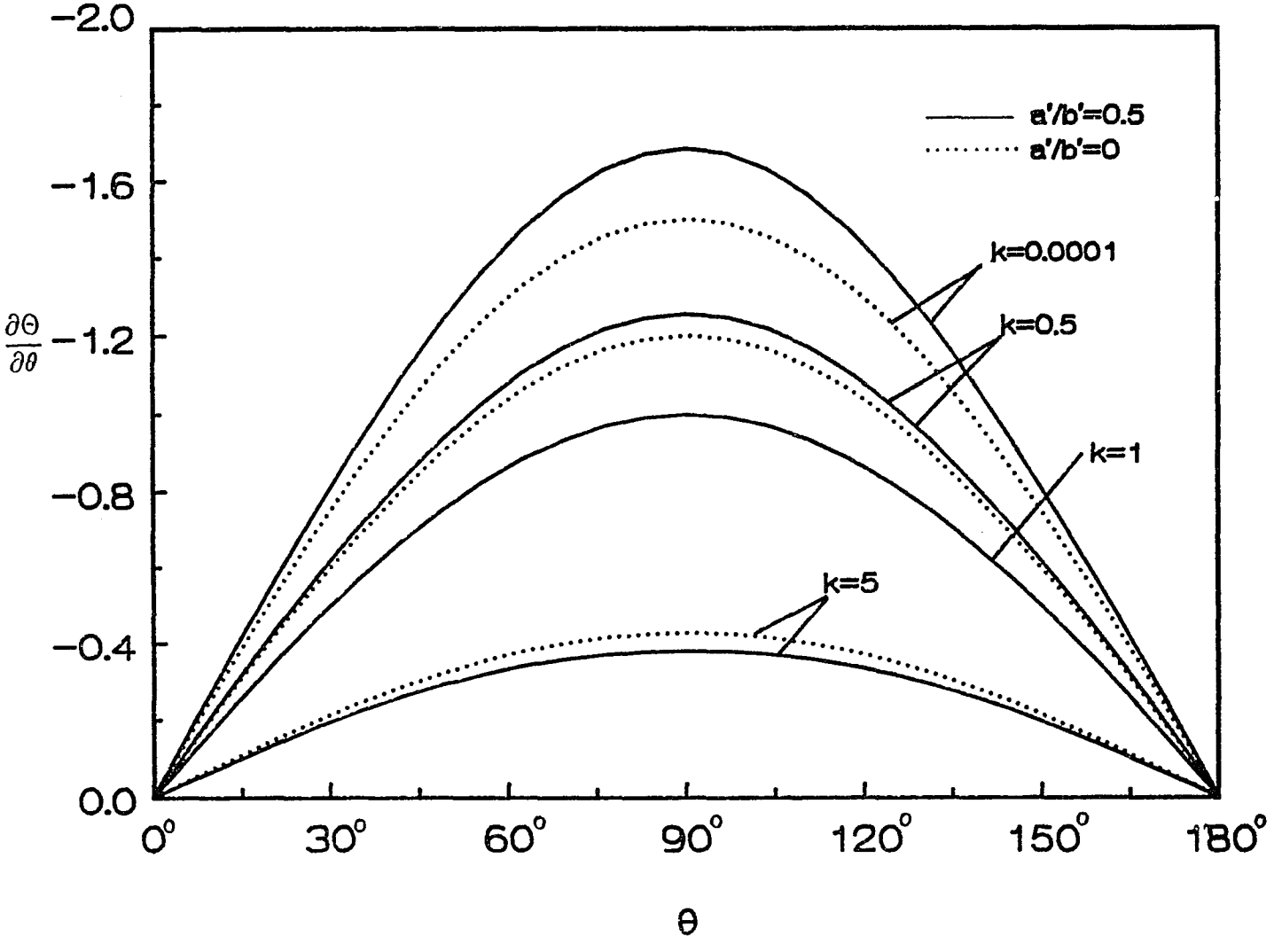
−2.0
−1.6
−1.2
−0.8
−0.4
0.0
$\frac{\partial\Theta}{\partial\theta}$
0°
30°
60°
90°
120°
150°
180°
θ
a'/b'=0.5
a'/b'=0
k=0.0001
k=0.5
k=1
k=5

Fig.5

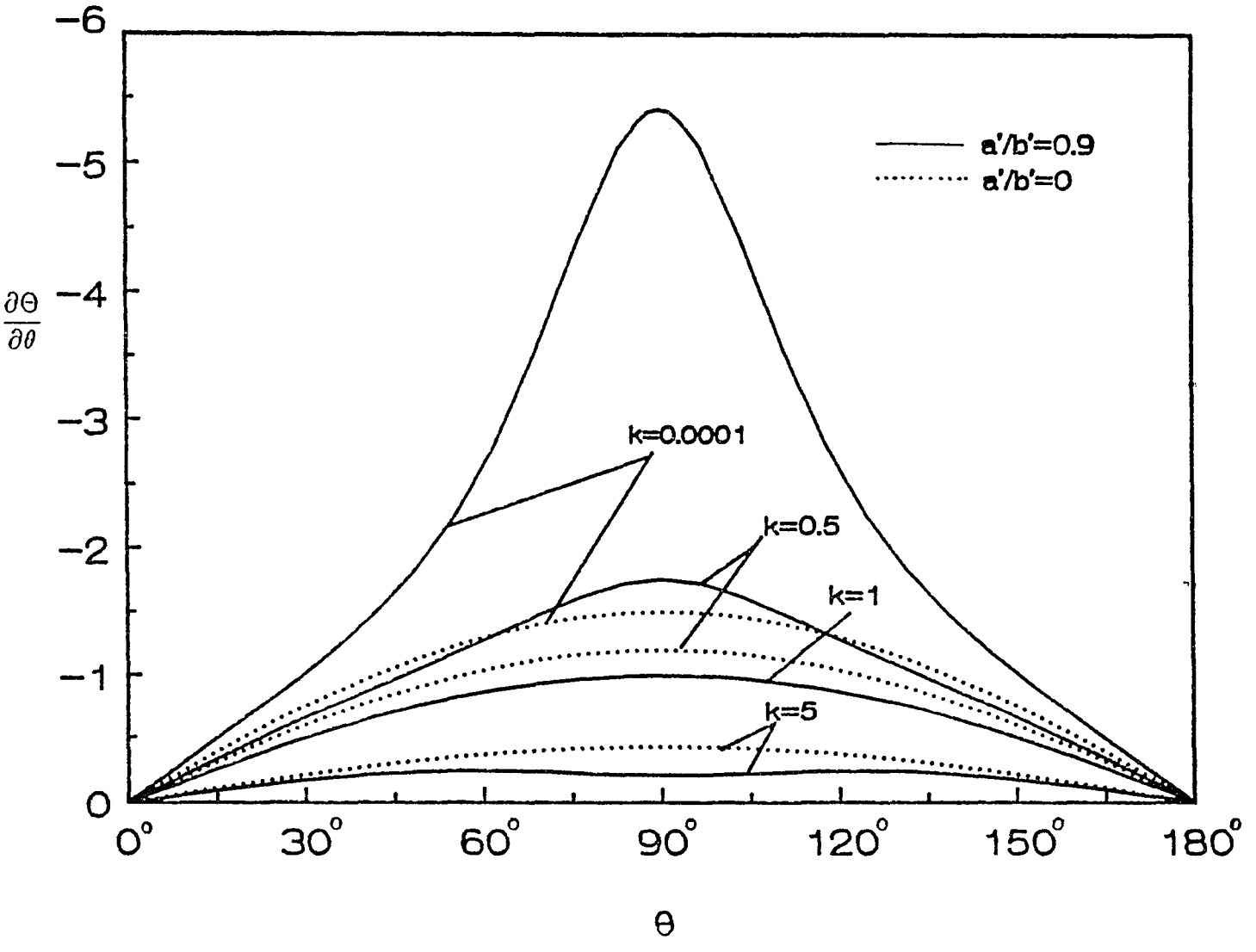
−6
−5
−4
−3
−2
−1
0
$\frac{\partial\Theta}{\partial\theta}$
a'/b'=0.9
a'/b'=0
k=0.0001
k=0.5
k=1
k=5
0°
30°
60°
90°
120°
150°
180°
θ

Fig.6

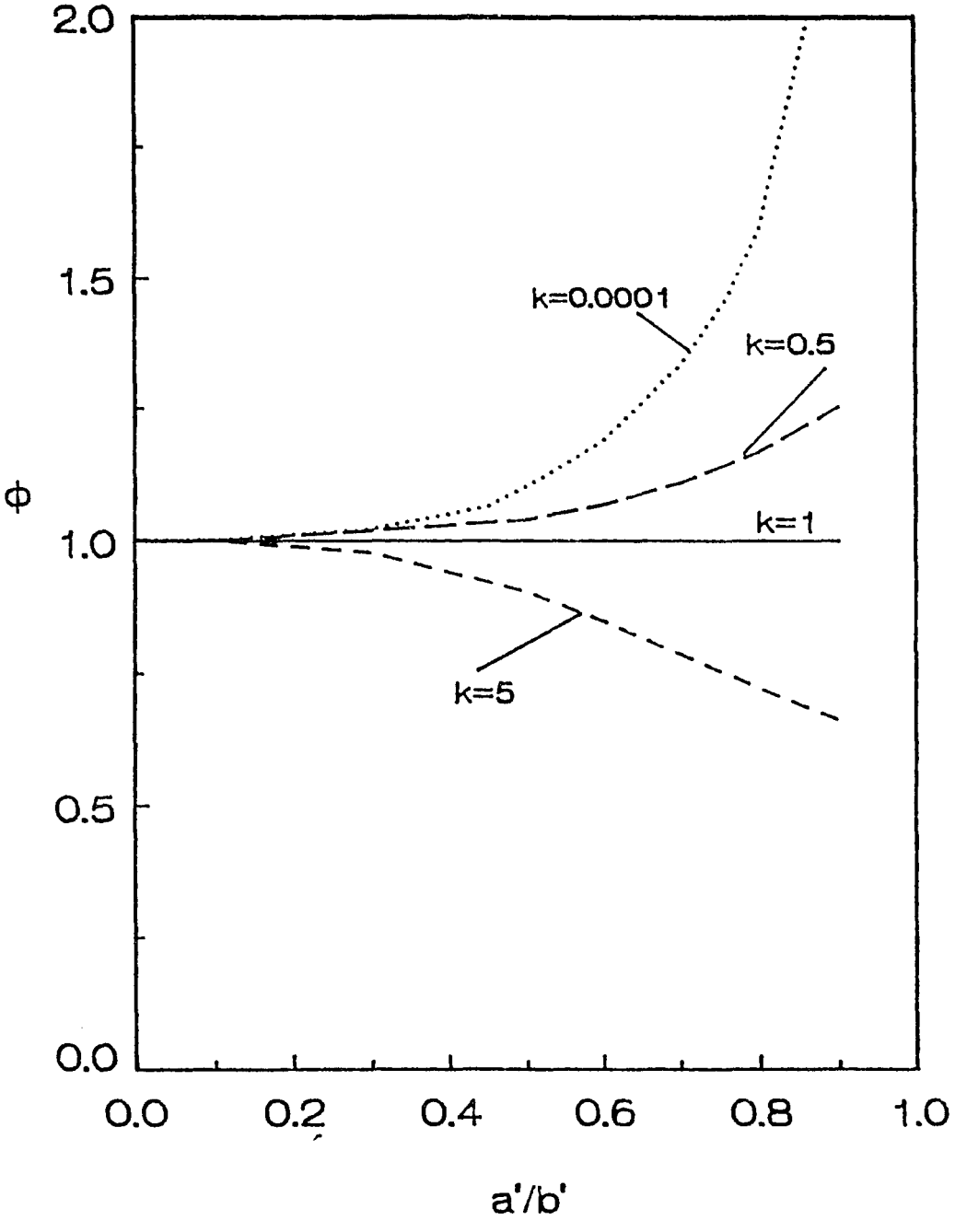

Flg.7

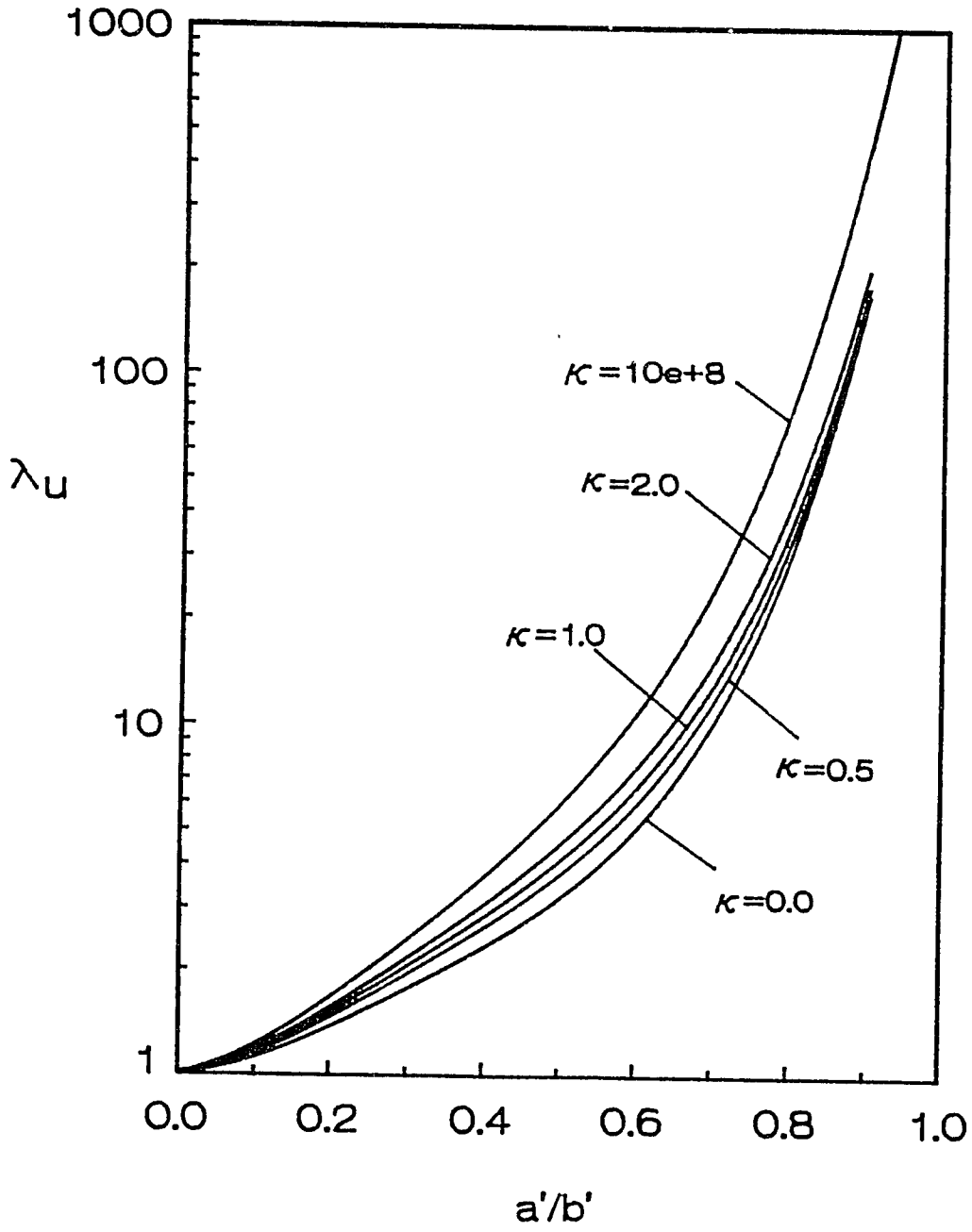

Fig.8

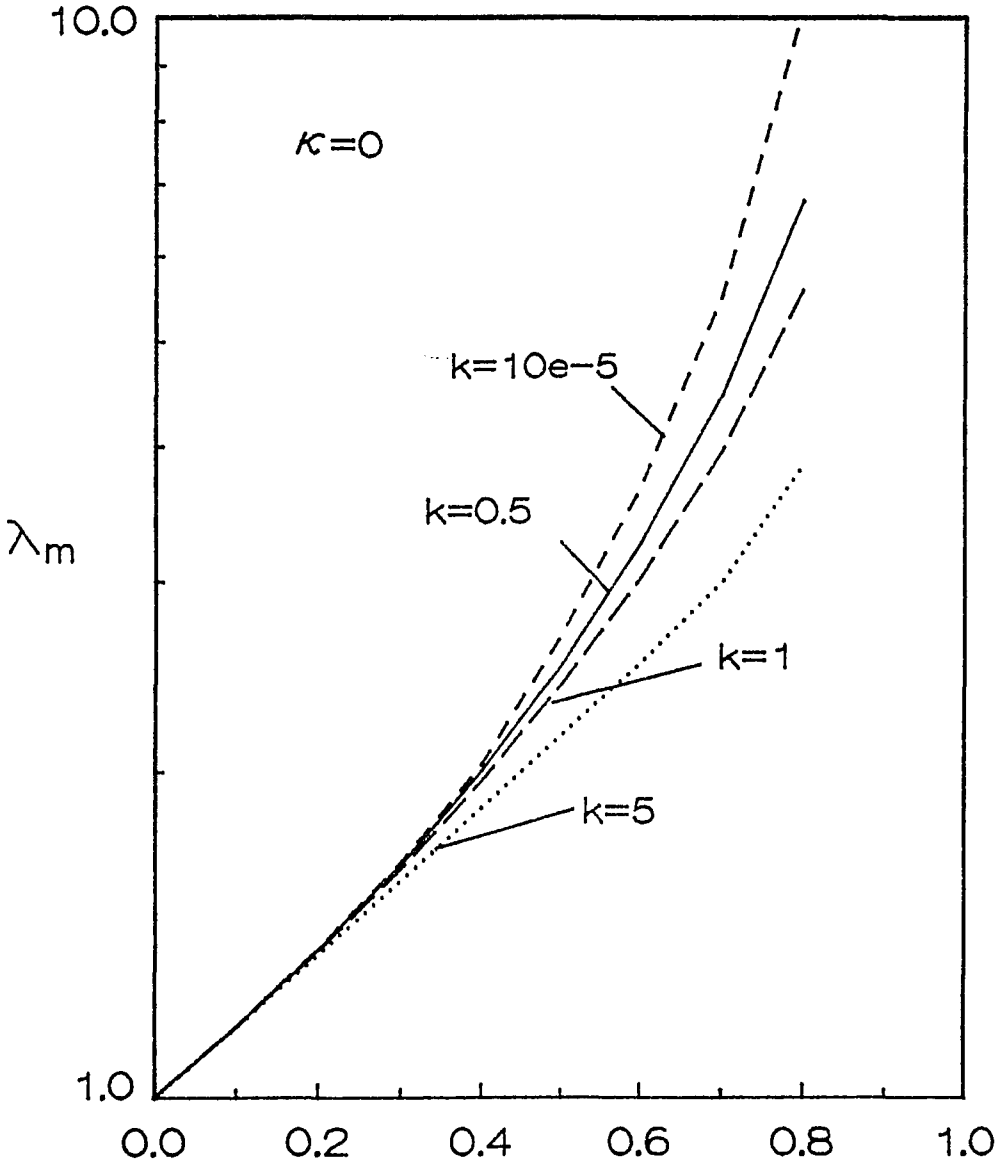

Fig.9

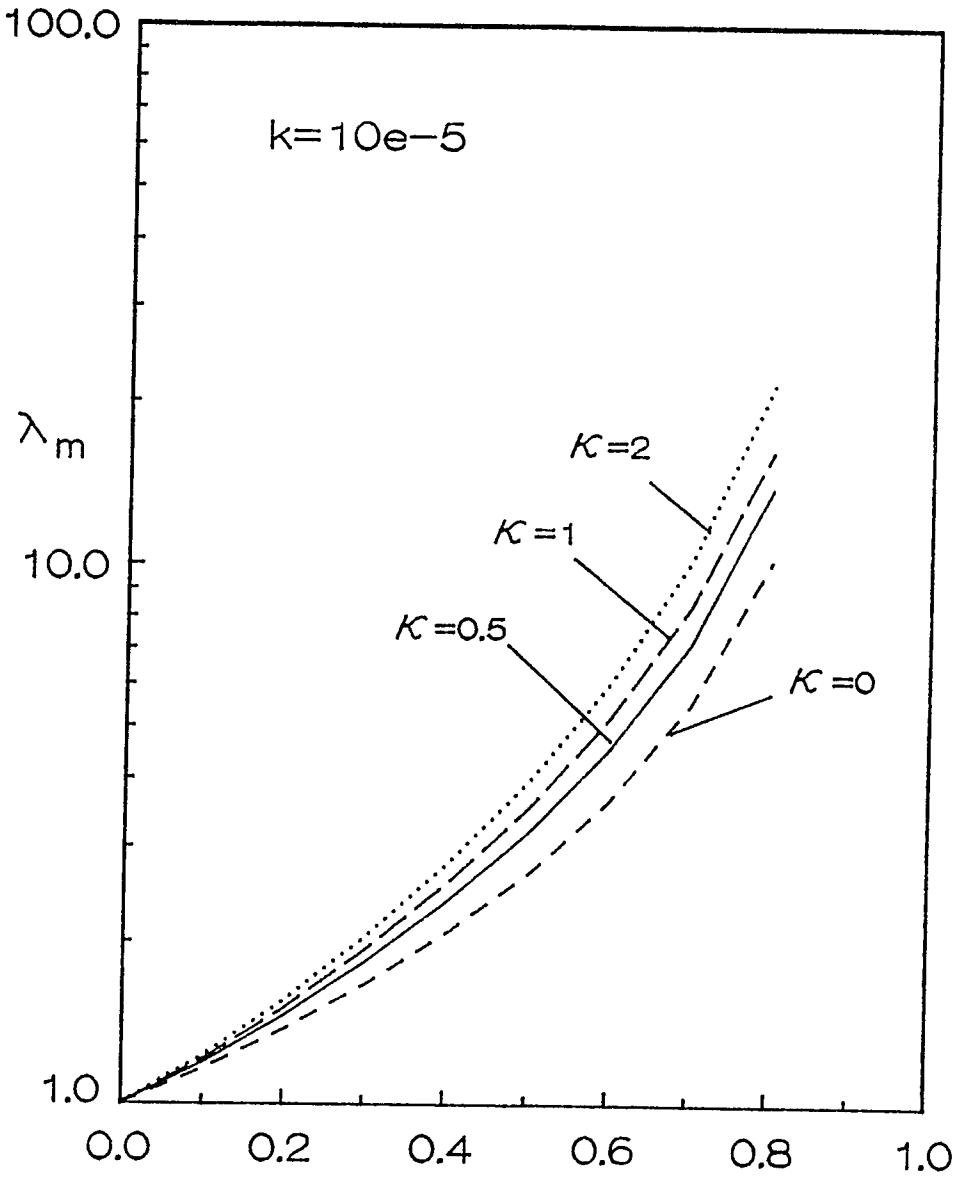

Fig.10

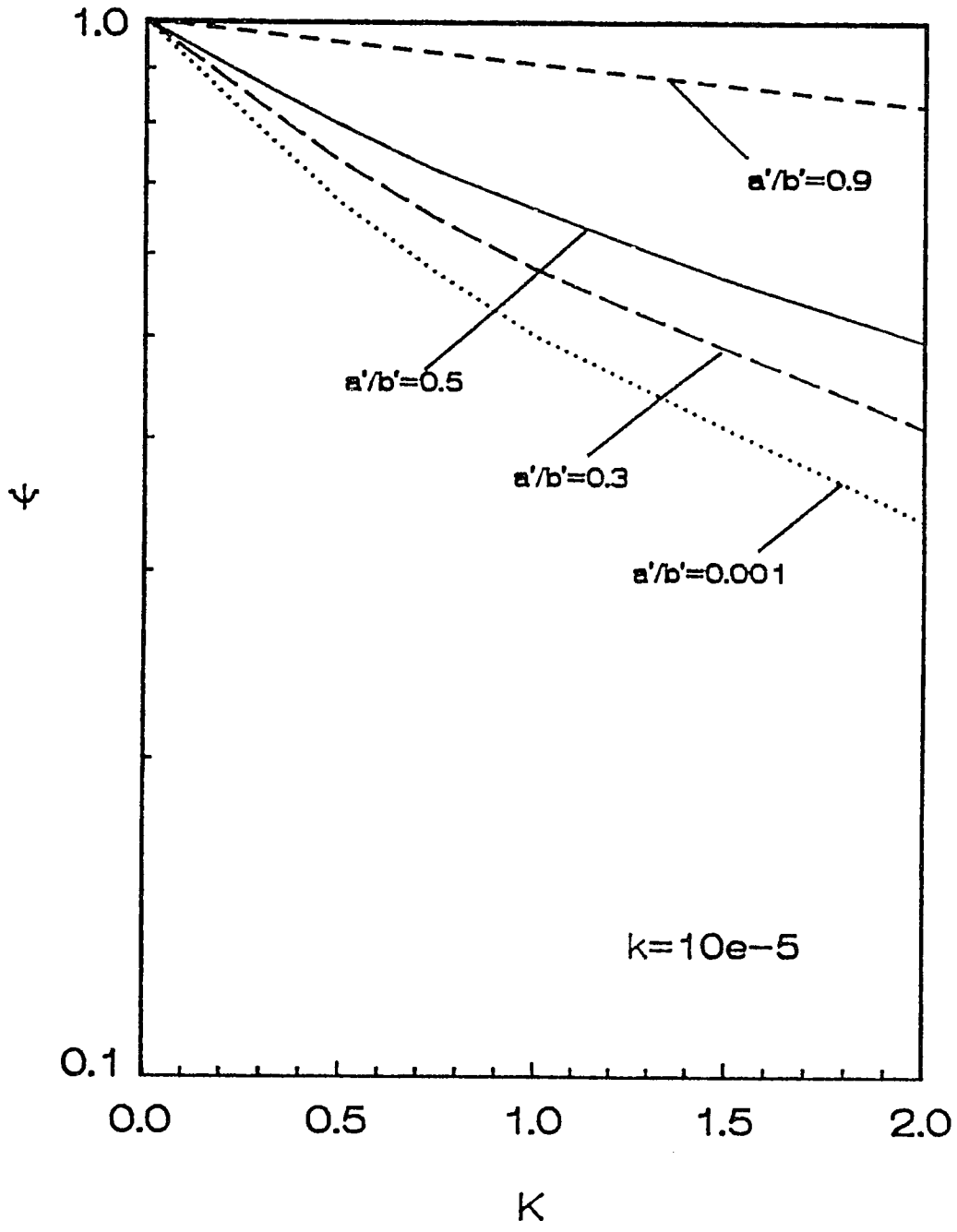

Fig.11

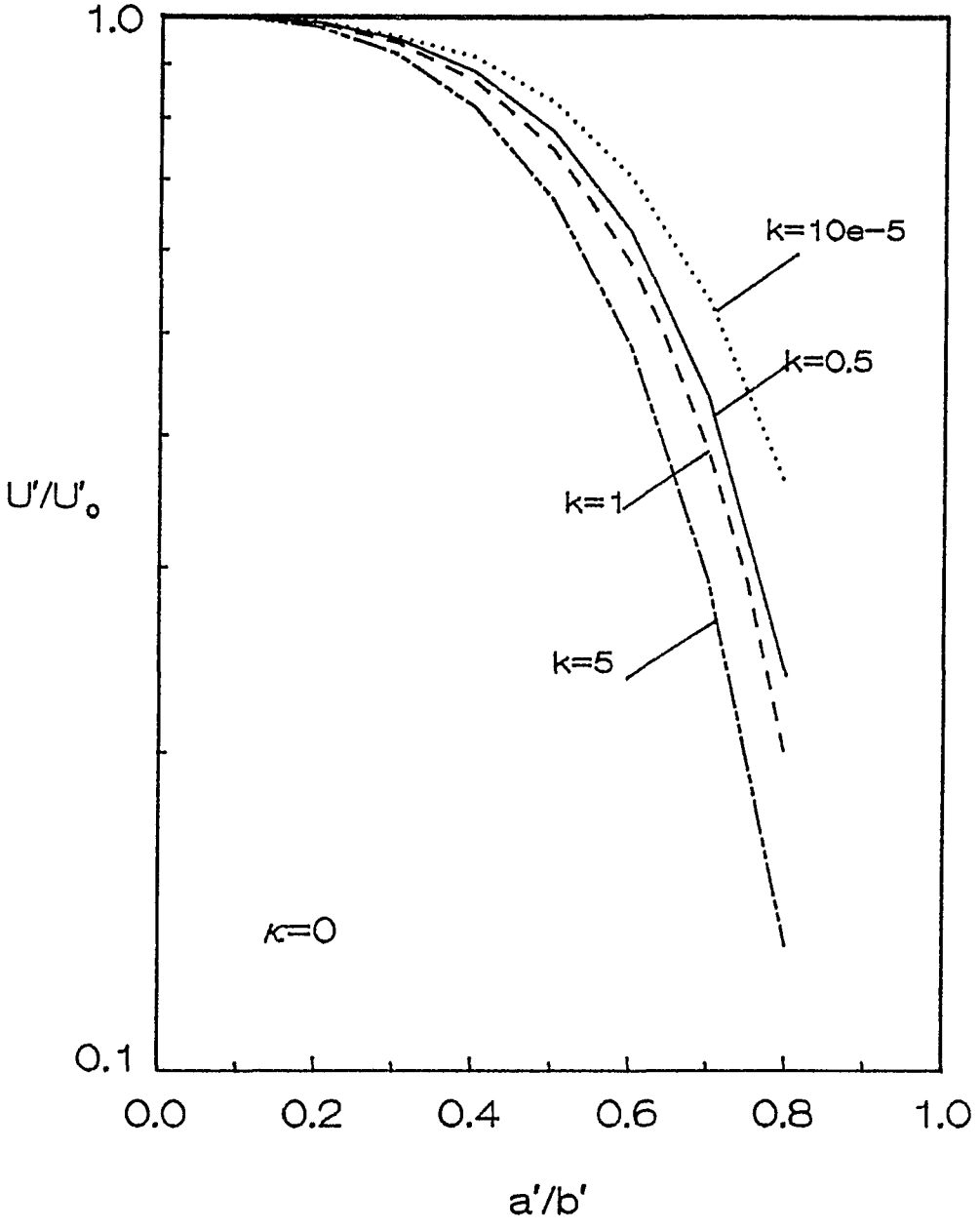

Fig.12(a)

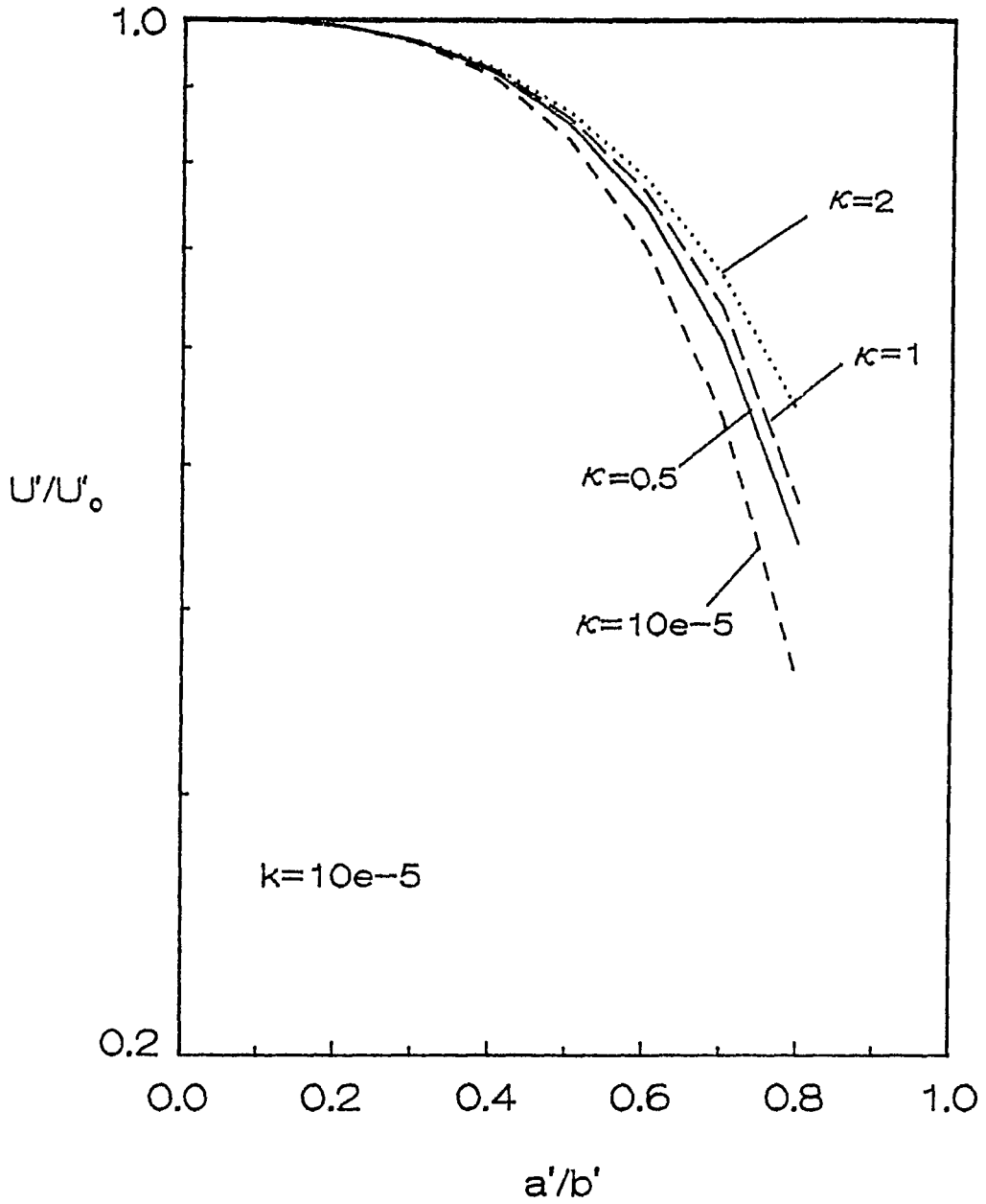

Fig.12(b)

Chapter IV

THERMOCAPILLARY MOTION OF DEFORMABLE FLUID PARTICLES IN TUBES

IV.1. Introduction

In this chapter, we relax the assumption of large interfacial tension and examine the influence of interfacial deformation on the thermocapillary movement of a bubble or a drop through a tube. We restrict our attentions to compact particles, i.e. those whose spherical radius ($a'= (3V'/4\pi)^{1/3}$) is smaller than that of the tube radius (b') ($a'/b'<1$). What we would like to learn from this analysis is how the deformation affects the competition between the hydrodynamic resistance forces which tend to slow the fluid particle down as a'/b' approaches one, and the Marangoni stresses which, for $k<1$, accelerate the fluid particle as a'/b' approaches one because of the higher surface temperature gradients which obtain as the fluid particle-tube gap thickness decreases. Clearly, hydrodynamic forces acting on the fluid particle will elongate the particle in the axial direction and thereby reduce the hydrodynamic interaction with the wall by increasing the gap thickness between the tube and the fluid particle. However, the opening up of the gap will reduce the temperature gradient on the fluid particle surface (for $k<1$), and this will decrease the Marangoni driving force. Our numerical solution of the flow should be able to resolve this competition. In addition, by calculating particle profiles, we hope to understand how deformation owing

to thermocapillary driven motion differs from the deformation due to other driving forces such as buoyancy.

To solve for the hydrodynamic flow and account for the deformation, we will use the boundary integral technique. We formulate the deformation problem in Section 2, and outline the boundary integral solution technique in Section 3. Finally, in Section 4, results for the test case of buoyancy driven motion are detailed, and results for thermocapillary motion for values of a'/b' ($a'/b' \leq 0.8$, at $\kappa=1$, $k=0$ or 1) are given and compared to the buoyancy results.

IV.2 Thermal and Hydrodynamic Field Equations and Boundary Conditions

In order to facilitate the implementation of the boundary integral solution technique, the problem is formulated in a reference frame in which the tube wall is at rest. Dimensional quantities are marked by a prime, and dimensionless quantities are unprimed. With respect to the tube fixed frame, we locate a cylindrical coordinate system (ρ',ω,z') with the z' axis of the cylindrical system coincident with the tube centerline. The bubble is assumed to be moving axisymmetrically along this centerline (see Fig.1). The spherical radius of the fluid particle and of the tube are denoted, respectively, by a' and b'. Droplet and continuous phase variables are denoted by superscripts (1) and (2) respectively. Finally, viscosity and thermal conductivity are denoted by $\kappa'^{(i)}$ and $k'^{(i)}$, and the ratios of the droplet

to the continuous phase viscosity and conductivity are denoted by κ and k respectively.

The temperature gradient is imposed in the laboratory frame. Far from the drop, in the lab frame, the temperature field is of the form $T'(z') = (\nabla' T')_\infty z' + T'_m$, where T' denotes the temperature, $(\nabla' T')_\infty$ denotes the imposed gradient, and T'_0 is the temperature at z'=0 when the fluid particle is not present. Since the temperature increases in the positive z-direction, the fluid particle moves in that direction. A non-dimensional temperature field $\theta^{(i)}(z,\rho)$ measured in the tube fixed system is defined as:

$$\Theta^{(i)}(z,\rho) = (T'^{(i)}(z,\rho) - T'_m)/(b'(\nabla' T')_\infty)$$

Note that this field must tend to $\pm z$ as $z \to \pm\infty$.

In formulating the energy conservation equations, we assume that the thermal convection is negligible, and therefore the non-dimensional temperature field is quasisteady and is described by Laplace's equation

$$\nabla^2 \Theta^{(i)} = 0 \qquad (1)$$

where ∇^2 is the (non-dimensional) axisymmetric Laplacian operator. We note that to scale the spatial coordinates ρ' and z', the tube diameter b' is used.

To formulate the hydrodynamic equation we need an appropriate scale for velocities. To scale velocities, we note that if the drop moves in an infinite medium in creeping motion and the variation of the surface tension

is assumed linear over the surface of the fluid particle, then the fluid particle moves quasi-steadily with a spherical shape and a velocity given by Young et al. (1959)

$$U_o'(T_m') = -\frac{a'(\nabla' T')_\infty (\partial\sigma'/\partial T')_{|T_m'}}{\mu'^{(2)}(1+3\kappa/2)(2+k)}$$

where $\partial\sigma'/\partial T'$ is the derivative of the tension with respect to the temperature, and is evaluated at the temperature (T'_m) of the position on the surface with the same z-coordinate as the center of mass. The motion is quasi-steady because the temperature T'_m increases with time.

In formulating the hydrodynamic equations, we assume that the Reynolds number is small and therefore the flow is quasisteady and creeping and therefore governed by the Stokes equations:

$$0 = -\nabla p^{(i)} + \nabla^2 \underline{u}^{(i)} \tag{2}$$

where $p^{(i)}$ is the pressure made dimensionless with $\mu^{(2)}U'_o/b'$, and the flow field is required to be solenoidal

$$0 = \nabla \cdot \underline{u}^{(i)} \tag{3}$$

to satisfy the condition of incompressibility.

Boundary conditions are formulated along the inside surface of the tube wall, and on the surface of the fluid particle. Along the tube wall ($\rho=\rho_o$), we assume energy cannot be conducted out of the tube,

$$\frac{\partial\Theta^{(2)}}{\partial\rho}=0 \tag{4}$$

and the fluid velocity is zero.

$$u_z^{(2)}=0, \qquad u_\rho^{(2)}=0 \tag{5}$$

To formulate boundary conditions on the fluid particle surface, we introduce the following surface formalisms. The locus of points which comprise the axisymmetric surface of the drop are prescribed parametrically as ($\rho(s)$,$z(s)$), where s is the arc length from the leading pole of the drop (see Fig.1). We define the total arc length as s_t. Using these parametrizations, we can express the normal ($\underline{n} = n_\rho\underline{\delta}_\rho + n_z\underline{\delta}_z$) and tangent vectors ($\underline{t} = t_\rho\underline{\delta}_\rho + t_z\underline{\delta}_z$) to the surface by the following relations

$$n_\rho=-\dot{z} \qquad n_z=\dot{\rho}$$
$$t_\rho=\dot{\rho} \qquad t_z=\dot{z}$$

where the superscript dots indicate differentiation with respect to the variable s, $\underline{n}$ is the normal pointing out of the drop, and $\underline{t}$ points in the

direction of increasing s. Finally the mean curvature of the surface, $\nabla_s \cdot \underline{n}$, is given by the equation:

$$\nabla_s \cdot \underline{n} = -\dot{z} / \rho + \ddot{\rho}\dot{z} - \dot{\rho}\ddot{z} \tag{6}$$

The thermal conditions on the fluid particle surface are that the temperature and conduction flux are continuous across the surface:

$$k(\underline{n} \cdot \nabla\Theta^{(1)}) - \underline{n} \cdot \nabla\Theta^{(2)} = 0 \tag{7}$$

$$\Theta^{(1)} = \Theta^{(2)} = \Theta^{(I)} \tag{8}$$

At the surface of the bubble (ρ=a) velocities are continuous,

$$\underline{u}^{(1)} = \underline{u}^{(2)} = \underline{u}^{(I)} \tag{9}$$

In addition, normal and tangential stresses balance surface tension forces. The tension on the surface of the moving drop varies with position on the surface because of the temperature gradient. To formulate the dependence of the tension on temperature, we first note that all points on the surface become warmer as the drop moves up the imposed temperature gradient. We have denoted by T'_m the temperature at the position on the surface with the same z coordinate as the center of mass. Relative to this temperature, we can expand the dependence of the surface tension in a Taylor series about the tension σ'_m for $T'=T'_m$ thus

$$\sigma(s)=\sigma'/\sigma'_m=1+\frac{b'(\nabla' T')_\infty}{\sigma'_m}(-\frac{\partial\sigma'}{\partial T'})|_{T'_m}(\Theta_s(s)-\Theta_m)+0((\Theta_s(s)-\Theta_m)^2)$$

where Θ_s denotes the surface temperature. We restrict our attention to the case in which the maximum change in temperature from T'_m on the surface is small enough that the linear term is sufficient to describe the surface tension variation. With this assumption the dependence of the nondimensional surface tension on the nondimensional temperature may be expressed as

$$\sigma = 1 - Ca(1+3\kappa/2)(2+k)(\Theta_s-\Theta_m)/a \qquad (10)$$

where Ca denotes the capillary number $\mu^{(2)}U'_o(T'_m)/\sigma'_m$.

The normal and tangential stress balances at the bubble surface becomes:

$$\kappa(\underline{n}\cdot\underline{\underline{\tau}}^{(1)})-(\underline{n}\cdot\underline{\underline{\tau}}^{(2)})=\frac{1}{Ca}[-\sigma\underline{n}\nabla_s\cdot\underline{n}]+\nabla_s\sigma \qquad (11)$$

where $\underline{\underline{\tau}}^{(i)}$ is the stress tensor of phase (i) non-dimensionalized by $\mu'^{(2)}U'_o/b'$ and ∇_s is the surface gradient operator. Substituting the assumed form for σ into equation (11) gives

$$\begin{aligned}&\kappa(\underline{n}\cdot\underline{\underline{\tau}}^{(1)})-(\underline{n}\cdot\underline{\underline{\tau}}^{(2)})\\&=\frac{1}{Ca}[-(1-Ca\lambda(\Theta_s-\Theta_m)/a)\underline{n}\nabla_s\cdot\underline{n}]-\lambda\nabla_s\Theta/a=\underline{F}\end{aligned} \qquad (12)$$

where $\lambda = (1+3\kappa/2)(2+k)$, $\nabla_s \Theta = (\partial\Theta/\partial s)\underline{t}$. Condition (12) provides the driving force for both the deformation and motion of the drop. The dimensionless parameters Ca, κ and k control the system. The capillary number provides a measure of the relative importance of viscous effects to surface tension effects.

In principle, steady motion is not possible because the capillary number appearing in the normal stress balance depends on time through the velocity scale $U'_o(T'_m(t))$. This complication does not arise in the case of the movement of spherical drops in tubes because the assumption of sphericity precludes use of the normal balance, and the problem becomes independent of Ca. Here we undertake the calculations and compute the steady velocity for a constant capillary number. This provides a quasi-static velocity.

The kinematic condition on the particle surface is of the form:

$$\frac{\partial H}{\partial t}(1+\frac{1}{U_o'}\frac{dU_o'}{dt'})+\underline{n}\cdot\underline{u}=0$$

where $H(\rho,z,t)=0$ locates the fluid particle interface in space, and t is nondimensionalized by (b'/U'_o). The factor $(1+(dU'_0/dt)/U'_0)$ accounts for the fact that the nondimensionalizing velocity is a function of time. At steady state, in a frame fixed to the fluid particle center of mass, the kinematic condition on the particle surface is $\underline{n}\cdot\underline{v}=0$ where $\underline{v}$ is the fluid velocity measured in the particle frame ($\underline{u}=\underline{v}+U\underline{\delta}_z$); in the tube fixed frame this condition becomes:

$$\underline{n}\cdot\underline{u}=\underline{n}\cdot U\underline{\delta}_z \tag{13}$$

This completes the formulation of the equations.

IV.3. Implementation of the Boundary Integral Technique

IV.3.1 *Formulation of Greens Functions*

We use the boundary integral technique to develop numerical solutions for the hydrodynamic and temperature field equations and boundary conditions. To use this technique, fundamental solutions of the Stokes and Laplace equations must be developed which describe hydrodynamic flow and conduction heat transfer due to point sources of momentum or energy flux. Since the fluid particle shape is axisymmetric, the fundamental solutions actually required are those for rings of momentum or heat placed axisymmetrically along the tube centerline. In addition in order to simplify the implementation of the boundary integral technique, we require these fundamental solutions to satisfy the boundary conditions of no-slip or zero radial conductive flux at the tube wall.

We begin with the development of the fundamental solutions for the flow caused by a ring of point forces of momentum placed along the tube centerline. To construct this solution, we divide this solution into two parts. The first is the Green's function due to a ring of point forces in an infinite medium. These are obtained by integrating the functions due to a point force over a ring (see Appendix A). The results are:

$$
\begin{aligned}
U_z^z &= -\frac{1}{4\pi}\frac{k}{(\rho_x\rho_y)^{1/2}}[F(k)+\frac{z^2}{d^2}E(k)] \\
U_\rho^z &= -\frac{z}{8\pi}\frac{k}{(\rho_x)^{3/2}(\rho_y)^{1/2}}[F(k)+(\rho_x^2-\rho_y^2-z^2)\frac{E(k)}{d^2}] \\
U_z^\rho &= \frac{z}{8\pi}\frac{k}{(\rho_x)^{1/2}(\rho_y)^{3/2}}[F(k)-(\rho_x^2-\rho_y^2+z^2)\frac{E(k)}{d^2}] \\
U_\rho^\rho &= -\frac{1}{8\pi}\frac{k}{(\rho_x\rho_y)^{3/2}}\{(\rho_x^2+\rho_y^2+2z^2)F(k) \\
&\quad -[2z^4+3(\rho_x^2+\rho_y^2)z^2+(\rho_x^2-\rho_y^2)^2]\frac{E(k)}{d^2}\}
\end{aligned}
\tag{14}
$$

where $z=z_x-z_y$, $k=[4\rho_x\rho_y/(z^2+(\rho_x+\rho_y)^2)]^{1/2}$, $d^2=(z_x-z_y)^2+(\rho_x-\rho_y)^2$ and F(k) and E(k) are complete elliptic integrals (Abramowitz & Stegun 1972) of first and second kinds.

The Eq.(14) are not valid on the symmetry axis. Equations below give the expressions for the velocity valid for $\rho_x \to 0$.

$$
\begin{aligned}
U_z^z &= -\frac{2z^2+\rho_y^2}{4(z^2+\rho_y^2)^{3/2}} \\
U_z^\rho &= \frac{z\rho_y}{4(z^2+\rho_y^2)^{3/2}} \\
U_z^\rho &= U_\rho^\rho = 0
\end{aligned}
$$

The velocities U_j^i have singular behaviour, but violate the no-slip boundary condition on the tube wall. To obtain a Green's function which satisfies no slip at the wall, we follow Tözeren (1984) and construct a second function V_j^i which satisfies Stokes equations without the point force, and which have surface velocities at the tube wall which are opposite to

those given by the functions in Eq.(14) when they are evaluated at $\rho_x=\rho_o$ The sum of $U_j^i+V_j^i$ is then the desired Green's function.

The general axisymmetric solution of Stokes equations in cylindrical coordinates is

$$
\begin{aligned}
V_z^z(z,\rho) &= \int_o^\infty \{A1(t)tI_0(t\rho)+B1(t)[\rho tI_1(t\rho)+2I_0(t\rho)]\}\cos(tz)dt \\
V_\rho^z(z,\rho) &= \int_o^\infty [A1(t)I_1(t\rho)+B1(t)\rho I_0(t\rho)]t\sin(tz)dt \\
V_z^\rho(z,\rho) &= \int_o^\infty \{A2(t)tI_0(t\rho)+B2(t)[\rho tI_1(t\rho)+2I_0(t\rho)]\}\sin(tz)dt \\
V_\rho^\rho(z,\rho) &= -\int_o^\infty [A2(t)I_1(t\rho)+B2(t)\rho I_0(t\rho)]t\cos(tz)dt
\end{aligned}
\qquad (15)
$$

where I_1 and I_0 are modified Bessel functions of zero and first orders. The functions A(t) and B(t) are chosen that the complementary solution V_j^i satisfies the boundary condition $V_j^i=-U_j^i$ at the tube surface $\rho_x=\rho_o$. To satisfy this condition, we first compute Fourier transforms of U_j^i evaluated at $\rho_x=\rho_o$. For those functions which are even in z_x this reduces to a cosine transform

$$U_j^i(\rho_o,z;\rho_y,0)=\int_o^\infty g_j^i(t)\cos ztdt \qquad (16a)$$

and for those which are odd in z_x this reduces to a sine transform:

$$U_j^i(\rho_o,z;\rho_y,0)=\int_o^\infty g_j^i(t)\sin ztdt \qquad (16b)$$

where

$$g_z^z = -\frac{1}{2\pi}\left[2K_0(\rho_o t)I_0(\rho_y t) - \rho_o t K_1(\rho_o t)I_0(\rho_y t) + \rho_y t K_0(\rho_o t)I_1(\rho_y t)\right]$$
$$g_\rho^z = \frac{1}{2\pi}\left[\rho_y t K_1(\rho_o t)I_1(\rho_y t) - \rho_o t K_0(\rho_o t)I_0(\rho_y t)\right]$$
$$g_z^\rho = -\frac{1}{2\pi}\left[\rho_o t K_1(\rho_o t)I_1(\rho_y t) - \rho_y t K_0(\rho_o t)I_0(\rho_y t)\right]$$
$$g_\rho^\rho = -\frac{1}{2\pi}\left[2K_1(\rho_o t)I_1(\rho_y t) + \rho_o t K_0(\rho_o t)I_1(\rho_y t) - \rho_y t K_1(\rho_o t)I_0(\rho_y t)\right] \quad (17)$$

By equating the above expressions to the general solutions (evaluated at $\rho_x=\rho_o$), the functions A1(t), A2(t), B1(t) and B2(t) can be obtained. Expressions for these constants are given in the Appendix B. With these expressions, the complementary component may be written in the symbolic form:

$$V_j^i = \int_o^\infty \begin{bmatrix} f_z^z \cos(zt) & f_z^\rho \sin(zt) \\ f_\rho^z \sin(zt) & -f_\rho^\rho \cos(zt) \end{bmatrix} dt \quad (18)$$

where $\underline{f}$ is a function of ρ_o, ρ_x, ρ_y & t. It may be note that at t tends to zero, all components of $\underline{f}$ tend to zero except for the zz-component, $f_z^z \approx -\ln((2\rho_o - \rho_x - \rho_y)t)/\pi$ which, because it is a logarithmic singularity allows Eq.(18) to be integrable. As t tends to infinity, $\underline{f}$ decays at the exponential rate $\exp[(\rho_x + \rho_y - 2\rho_o)t]/\pi$ as long as $\rho_x<\rho_o$, $\rho_y<\rho_o$.

Although the above Green's functions are well formulated, they are computationally inefficient because of the large computer time necessary evaluate the Fourier integrals in the complementary solution. To make the computation time more manageable, we consider the solution for a periodic

array of rings separated by a distance L. This solution can be obtained by first displacing z_y in the above formula by nL to obtain the velocity field for a ring located at position z_y=nL, and then summing the terms over n. For example:

$$V_z^{\rho} = \int_o^{\infty} f_z^{\rho} \sum_{n=-N}^{N} \sin[(z+nL)t]dt \tag{19}$$

The sum within the integral on the right-hand side of Eq.(19) can be computed in close form using the identity

$$\begin{aligned} H(N) &= \sum_{n=-N}^{N} \exp[i(z+nL)t] \\ &= \exp(izt)\frac{\cos(NLt)-\cos[(N+1)Lt]}{1-\cos Lt} \end{aligned} \tag{20}$$

To obtain an infinite array of rings we use the asymptotic expression Lighthill 1958) at the limit as N tends to infinity

$$H(\infty) = \frac{2\pi}{L}\exp(izt) \sum_{m=-\infty}^{\infty} \delta(t-2\pi m/L) \tag{21}$$

where δ is the one-dimensional delta function. Substituting Eq.(21) into Eq.(20), considering that $f_z^{\rho}(t=0)=0$, and adding the contribution form the rings the periodic Green's function are obtained

$$G^{A}{}_{\rho}^{z} = \frac{2\pi}{L}\sum_{m=1}^{\infty} f_z^{\rho}(t_m)\sin(t_m z) + \sum_{n=-\infty}^{\infty} U_z^{\rho}(z+nL) \tag{22}$$

where $t_m=2\pi m/L$, the superscript A stands for array. The two sums on the right-hand of Eq.(22) converge at rates that are respectively exponential and algebraic. Similarly, considering $f_{\rho}^{z}(t=0) = f_{\rho}^{\rho}(t=0)$, we derive expressions similar to Eq.(18) for $G^{A\rho}{}_{z}$ and $G^{A\rho}{}_{\rho}$.

The last Green's function $V_z^z + U_z^z$ presents a problem because f_z^z in the definition of V_z^z is logrithmically singular as t→0. We therefore follow Pozrikidis (1992) and regularize the behavior of f_z^z by using the function $K_0[(2\rho_o - \rho_x - \rho_y)t]/\pi$. This function is asymptotically equal to f_z^z as $t \to 0$, exponentially decays to zero as t→∞, and its cosine transform is integrable (Happel & Brenner 1973)

$$\int_o^{\infty} K_0[(2\rho_o - \rho_x - \rho_y)t]\cos(zt)dt = \frac{\pi}{2[Z^2 + (2\rho_o - \rho_x - \rho_y)^2]^{1/2}}$$

We therefore define a function f'^{z}_{z} by $f'^{z}_{z} = f_z^z - K_0[(2\rho_o - \rho_x - \rho_y)t]/\pi$ and we write V_z^z as:

$$V_z^z = \int_o^{\infty} f'^{z}_{z}\cos(zt)dt + \frac{1}{2[z^2 + (2\rho_o - \rho_x - \rho_y)^2]^{1/2}} \tag{23}$$

The integrand is bounded as t→0, and we can now construct the periodic Green's function in the following form:

$$G^{A}{}_{z}^{z} = \frac{2\pi}{L}\left[\frac{1}{2}f'{}_{z}^{z}(t=0) + \sum_{m=1}^{N} f'{}_{z}^{z}(t_m)\cos(t_m z)\right] + \sum_{n=-\infty}^{\infty}\left[U_z^z(z+nL) + \frac{1}{2[(z+nL)^2 + (2\rho_o - \rho_x - \rho_y)^2]^{1/2}}\right] \quad (24)$$

The first sum on the right-hand side of Eq.(24) decays at an exponential rate. To demonstrate that the second sum is convergent, U_z^z is expanded in an asympototic series for large nL,

$$U_z^z(z+nL) = -\frac{1}{4[(z+nL)^2 + (\rho_x + \rho_y)^2]^{1/2}}\left[2 - \frac{(\rho_x - \rho_y)^2}{(z+nL)^2 + (\rho_x - \rho_y)^2}\right] + \cdots$$

Comparing Eq.(24) with the above equation we note that the terms in second series on the right-hand side of Eq.(24) decay as $(nL)^{-3}$ and thus the corresponding sum is convergent. In this paper, in order to compute $G^{A}{}_{j}^{i}$, the first infinite sum in Eq.(24) is truncated at a value of m such that $(2\rho_o - \rho_x - \rho_y)t=25$, and second value n=40.

The above considerations are for the calculation of the velocity Green's function for a ring of point forces. For the computation of the temperature distribution by a boundary integral equation, the temperature distribution arising from a ring of point sources of energy placed axisymmetrically in the tube, and subject to zero flux at the tube wall is necessary. Again we divide this Green's function into two terms. The first is the temperature field due to the ring of point sources in an infinite medium. This function follows by integrating the point source solution around a ring; the result is:

$$\Phi^i(\underline{x},\underline{y}) = -\frac{1}{2\pi}\frac{k}{(\rho_x\rho_y)^{1/2}}F(k) \tag{25}$$

where $\Phi^i(\underline{x},\underline{y})$ is the temperature at position $\underline{x}$ due to the ring of point sources of radius ρ_y and is located along the plane z_y. The second is the temperature field (without any sources) due to the heat flux $\partial\Phi^i/\partial\rho_x$ evaluated at the wall. The general solution for axisymmetric conduction in the tube which is an even function of z_x-z_y is given by:

$$\Phi^t(\underline{x},\underline{y}) = \frac{1}{\pi}\int_o^\infty C(t)I_0(\rho_x t)t\cos(zt)dt \tag{26}$$

At the tube wall $\rho_x=\rho_o$, $\partial\Phi^i/\partial\rho_x=-\partial\Phi^t/\partial\rho_x$. Expressing $\partial\Phi^i/\partial\rho_x$ in terms of a Fourier series,

$$\frac{\partial\Phi^i}{\partial\rho_x}(\rho_x=\rho_o) = \int_o^\infty g(t)\sin ztdt \tag{27}$$

where $g(t) = t\,K_1(\rho_o t)I_0(\rho_y t)/\pi$, we easily find C(t) to be equal to $-K_1(\rho_o t)I_0(\rho_y t)/I_1(r_o t)$.

IV.3.2. *Construction of the Boundary Integral Equations.*

To formulate boundary integral equations for the velocity and temperature on the drop interface, we consider two domains. The first is the interior domain (V_p) of the closed fluid particle with bounding surface S_b.

Considering first the hydrodynamic equations, Ladyzhensakaya (1963) derives the following equation for the velocity at a particular position $\underline{x}$ within the volume ($\underline{x} \in V_p$) in terms of the velocities $u_i^{(1)}$ and stresses $f_i^{(1)}$ (evaluated from the inside) along the surface. Simplifying this equation for axisymmetric motion, and noting the periodicity of the flow, the following equation results:

$$C_{ji}u_i^{(1)}(\underline{x}) = \int_{S_b} u_i^{(1)}(\underline{y}) T^{A^i}_{jk}(\underline{x},\underline{y}) n_k(\underline{y}) ds(\underline{y}) - \frac{1}{\kappa}\int_{S_b} G^{A^i}_{j}(\underline{x},\underline{y}) f_i^{(1)}(u_i(\underline{y})) ds(\underline{y}) \tag{28}$$

In the above all indices take on the value ρ or z and the summations indicated by repeated indices are over ρ and z. The matrix C_{ji} is diagonal, and the diagonal elements are equal to -1 when $\underline{x} \in V_p$ and equal to -1/2 when $\underline{x} \in S_b$. Further, in Eq.(28), n_k is the outward normal to the surface, $f_i^{(1)}$ is the fluid stress due to the inside flow field $u_j^{(1)}$ exerted on the surface ($f_i(u_i(\underline{y})) = \tau_{ki} n_k$).

We next write a similar equation to Eq.(28) for the closed domain bounded by the particle, the tube wall, and two identical surfaces which span the continuous phase and are located one period L apart.

$$C_{ji}u_i^{(2)}(\underline{x}) = -\int_{S_\tau} u_i^{(2)}(\underline{y}) T^{A^i}_{jk}(\underline{x},\underline{y}) n_k(\underline{y}) ds(\underline{y}) + \int_{S_\tau} G^{A^i}_{j}(\underline{x},\underline{y}) f_i^{(2)}(u_i(\underline{y})) ds(\underline{y}) \tag{29}$$

where the surface integrals are over the total surface (S_T) area bounding the closed region, and the normal points into the domain from the bounding surfaces. Since the velocity along the tube surface is equal to zero, and the Green's functions satisfy no slip along the tube surface, the integrals along the tube surface in Eq.(29) are equal to zero. Due to the periodicity of the flow and the Green's functions, the integrals along the cross sections are equal and opposite and cancel. This leaves only the integral along the fluid particle surface in Eq.(29).

Multiplying equation (28) by κ, adding the result to Eq.(29) and using the boundary conditions of continuity of velocity and the balance of stress results in the following equation:

$$u_j(\underline{x}) - \frac{2(1-\kappa)}{(1+\kappa)}\int_S u_i(\underline{y}) T^{A^i}_{jk}(\underline{x},\underline{y}) n_k(\underline{y}) ds(\underline{y}) = -\frac{2}{(1+\kappa)}\int_S G^{A^i}_j(\underline{x},\underline{y}) F_i(u_i(\underline{y})) ds(\underline{y}) \tag{30}$$

Note importantly that when κ=1, only the F_i integral remains, and the result becomes:

$$u_j(\underline{x}) = -\frac{2}{(1+\kappa)}\int_S G^{A^i}_j(\underline{x},\underline{y}) F_i(u_i(\underline{y})) ds(\underline{y}) \tag{31}$$

A boundary integral equation for the temperature can be formulated using the same procedure. However, we choose not to use a periodic formulation for the temperature field but instead consider only a single

particle placed in a linear temperature gradient. The analogue of Eq.(28) is straightforward and is given by:

$$\frac{1}{2}\Theta^{(1)}(\underline{x}) = -\frac{1}{k}\int_{S_b}\Big[\Theta^{(1)}(\underline{y})\underline{n}(\underline{y})\cdot\nabla\Phi(\underline{x},\underline{y}) - \Phi(\underline{y})\underline{n}(\underline{y})\cdot\nabla\Theta^{(1)}(\underline{x},\underline{y})\Big]ds(\underline{y}) \tag{32}$$

where $\underline{x}$ lies on the surface. In this case the analogue of equation (29) for the domain bounded by the particle surface, the tube wall and the surfaces spanning the cross section is of the form:

$$\frac{1}{2}\Theta^{(2)}(\underline{x}) = \int_{S}\Big[\Theta^{(2)}(\underline{y})\underline{n}(\underline{y})\cdot\nabla\Phi(\underline{x},\underline{y}) - \Phi(\underline{y})\underline{n}(\underline{y})\cdot\nabla\Theta^{(2)}(\underline{x},\underline{y})\Big]ds(\underline{y}) \tag{33}$$

where again S_T includes the tube wall, the cross sectional areas and the particle surface. Since the wall is insulated and the Green's function satisfies zero radial flux at the tube wall, the contribution to $\Theta^{(2)}(\underline{x})$ from the tube wall integral is zero. Next, the above equation is written for the temperature field at infinity ($\Theta_\infty = z_x$). Subtracting this equation from Eq.(33) results in:

$$\begin{aligned}\frac{1}{2}\Big[\Theta^{(2)}(\underline{x}) - \Theta_\infty(\underline{x})\Big] &= \int_{S_b+S_i+S_o}\Big[(\Theta^{(2)}(\underline{x},\underline{y}) - \Theta_\infty(\underline{x}))\underline{n}(\underline{y})\cdot\nabla\Phi(\underline{x},\underline{y})\\ \frac{1}{2}\Big[\Theta^{(2)}(\underline{x}) - \Theta_\infty(\underline{x})\Big] &= \int_{S_b+S_i+S_o}\Big[(\Theta^{(2)}(\underline{x},\underline{y}) - \Theta_\infty(\underline{x}))\underline{n}(\underline{y})\cdot\nabla\Phi(\underline{x},\underline{y})\\ &\quad -\Phi(\underline{y})\underline{n}(\underline{y})\cdot\nabla(\Theta^{(2)}(\underline{x},\underline{y}) - \Theta_\infty(\underline{x}))\Big]ds(\underline{y})\end{aligned} \tag{34}$$

If the cross sectional areas are taken far enough away from the particle where the temperature field is close to the far field, the integrals along S_o and S_i disappear, and the following integral equation involving only a contribution along the bubble surface results:

$$\frac{1}{2}\left[\Theta^{(2)}(\underline{x})-\Theta_\infty(\underline{x})\right]=\int_{S_b}\left[(\Theta^{(2)}(\underline{x},\underline{y})-\Theta_\infty(\underline{x}))\underline{n}(\underline{y})\cdot\nabla\Phi(\underline{x},\underline{y})\right.$$
$$\left.-\Phi(\underline{y})\underline{n}(\underline{y})\cdot\nabla(\Theta^{(2)}(\underline{x},\underline{y})-\Theta_\infty(\underline{x}))\right]ds(\underline{y}) \qquad (35)$$

By writing equation (33) for Θ_∞ and subtracting from the above, we arrive at a final equation for $\Theta^{(2)}$:

$$\frac{1}{2}\Theta^{(2)}(\underline{x})=\Theta_\infty(\underline{x})+\int_{S_b}\left[\Theta^{(2)}(\underline{x},\underline{y})\underline{n}(\underline{y})\cdot\nabla\Phi(\underline{x},\underline{y})\right.$$
$$\left.-\Phi(\underline{y})\underline{n}(\underline{y})\cdot\nabla\Theta^{(2)}(\underline{x},\underline{y})\right]ds(\underline{y}) \qquad (36)$$

Finally subtracting Eq.(36) from Eq.(32) and using the thermal boundary conditions results in a final equation for the surface temperature:

$$\Theta(\underline{x})=\frac{2z_{\underline{x}}}{1+k}+\frac{2(k-1)}{1+k}\int_{S_b}\Theta(\underline{y})n(\underline{y})\cdot\nabla\Phi(\underline{x},\underline{y})ds(\underline{y}) \qquad (37)$$

Where kernel $\underline{n}(\underline{y})\cdot\nabla\Phi(\underline{x},\underline{y})$ are given in the Appendix C.

As we have already remarked, the bubble surface is specified by using the arc length s (measured from the leading edge) and the paramertization $\rho(s)$ and $z(s)$. Therefore Eqs.(31) and (37) may be expressed in the following form:

$$\begin{bmatrix} u_\rho \\ u_z \end{bmatrix} = -\frac{2}{(1+\kappa)} \int_o^{s_t} \begin{bmatrix} F_\rho G^{A\rho}_{\ \rho} & +F_z G^{Az}_{\ \rho} \\ F_\rho G^{A\rho}_{\ z} & +F_z G^{Az}_{\ z} \end{bmatrix} \rho_y ds_y \tag{38}$$

and

$$\Theta(\underline{x}) = \frac{2z_x}{1+k} + \frac{2(k-1)}{1+k} \int_o^{s_t} \underline{n}(\underline{y}) \cdot \nabla\Phi(\underline{x},\underline{y}) \Theta(\underline{y}) \rho_y ds_y \tag{39}$$

IV.3.3 *Numerical Solution Procedure*

Equations (38) & (39) can be used to determine the surface temperature and velocity once the shape of the surface is specified. However, the shape is unknown, and we therefore construct an initial value problem starting from a known shape in order to proceed to the steady solution shape. We start with one of two initial shapes. For compact fluid particles (a'<b'), computations are begun using a spherical shape. Once these analytical initial shapes are prescribed, N node points are selected on the interface contour, and are parameterized by their arc lengths as measured from the leading pole ($\rho_s(s)$,$Z_s(s)$), s∝[0,S_t]). The N-1 arcs between the node points have arc lengths identified as s_i (i=1,2,... N-1). For this initial shape, the N-1 arcs are all equal. The positions of these N points are used to construct a cubic spline fit of the shape with the arc length as the spline parameter. From this fit, numerical values for the normal and tangent vectors and the curvature can be obtained by differentiation. We then compute the initial surface temperature at the node points by using Eq.(39). This computation is undertaken as follows. The integral in Eq.(39)

is broken up into contributions from each arc. Over each arc, we define a new local ξ as:

$$\xi = \frac{s - s_i}{s_{i+1} - s_i}$$

where $0 \leq \xi \leq 1$ and i=1 to N-1. The temperature is assumed to vary linearly within each arc, and we write this variation in terms of the temperature at the node ends (θi, j=1,N-1)

$$\Theta(\xi) = \Theta^j \Psi_1(\xi) + \Theta^{j+1} \Psi_2(\xi) \tag{40}$$

where the linear shape functions are defined as:

$$\Psi_1(\xi) = 1\text{-}\xi \qquad \Psi_2(\xi) = \xi$$

Equation (39) may then be recast as:

$$\Theta(\underline{x}) = \frac{2z_x}{1+k} + \frac{2(k-1)}{1+k} \sum_{j=1}^{N-1} \left[\left[\int_{\Delta s_j} \underline{n}(\underline{y}) \cdot \nabla \Phi(\underline{x}, \underline{y}) \Psi_1(\underline{y}) \rho_y ds_y \right] \Theta^j(\underline{y}) + \left[\int_{\Delta s_{j+1}} \underline{n}(\underline{y}) \cdot \nabla \Phi(\underline{x}, \underline{y}) \Psi_2(\underline{y}) \rho_y ds_y \right] \Theta^{j+1}(\underline{y}) \right] \tag{41}$$

Each of the integrals along the arc segments is numerically evaluated using Gaussian quadrature with the Green's functions evaluated at each of these subdivisions of the quadrature by using the cubic spline representation to

locate ρ_y and z_y. When $\underline{x}$ is not equal to $\underline{y}$, five quadrature points are used. When $\underline{x} = \underline{y}$, the integrand is singular (though integrable) and the following and the following procedure is used. The limits of integration are taken a small distance away from the node point, and eight quadrature points are used. The integral around the node point is approximated by using an analytical form for the Green's function as $\underline{x} \rightarrow \underline{y}$. Evaluating Eq.(41) at the N node points leads to an N×N matrix for the unknown node point temperatures. This matrix can then be inverted to obtain the surface tempratures.

A cubic spline fit of the node point temperatures, with s as the spline parameter, is then computed and differentiated to obtain $\partial\Theta/\partial s$ at the node points. Frcm the latter calculation, and the cubic spline calculated curvature, the force F_i as given in Eq.(12) can be computed at the node points. We now compute the surface velocity using Eq.(38). Again the boundary integral is divided into the contributions of N-1 arcs, and F_i is assumed to vary linearly along each segment:

$$F_\rho(\xi) = F_\rho^j \Psi_1(\xi) + F_\rho^{j+1} \Psi_2(\xi)$$
$$F_z(\xi) = F_z^j \Psi_1(\xi) + F_z^{j+1} \Psi_2(\xi) \tag{42}$$

$$\begin{bmatrix} u_\rho \\ u_z \end{bmatrix} \approx -\frac{2}{(1+\kappa)} \sum_{j=1}^{N-1} \left\{ \left[\int_{\Delta s_j} \begin{bmatrix} G^{A\rho}_{\rho} & G^{Az}_{\rho} \\ G^{A\rho}_{z} & G^{Az}_{z} \end{bmatrix} \Psi_1(\underline{y}) \rho_y ds_y \right] \cdot \begin{bmatrix} F_\rho^j \\ F_z^j \end{bmatrix} \right.$$
$$\left. + \left[\int_{\Delta s_{j+1}} \begin{bmatrix} G^{A\rho}_{\rho} & G^{Az}_{\rho} \\ G^{A\rho}_{z} & G^{Az}_{z} \end{bmatrix} \Psi_2(\underline{y}) \rho_y ds_y \right] \cdot \begin{bmatrix} F_\rho^{j+1} \\ F_z^{j+1} \end{bmatrix} \right\} \tag{43}$$

As before, each of the integrals along the arc segments is numerically evaluated using Gaussian quadrature.

To efficiently compute elliptic integrals in the Green's functions, we use the recursive formulae (Davis 1962)

$$F(k) = [\pi(1+K_1)(1 + K_2)(1 +K_3)\cdots]^{1/2}$$
$$E(k) = F(k)(1-k^2\, p/2) \qquad (44)$$

where $K_0=k$, $K_p = (1-C)/(1+C)$, $C = (1-K^2_{p-1})^{1/2}$

and
$$p = 1+\frac{K_1}{2}\left[1+\frac{K_2}{2}\left[1+\frac{K_3}{2}[\cdots]\cdots\right]\right.$$

With the surface velocity calculated, we use the kinematic condition to construct the surface locus at the next time step, Δt.

$$\frac{\partial \rho_s}{\partial t}(1+\frac{1}{U_o'}\frac{dU_o'}{dt}) = u_\rho(\rho_s, z_s)$$
$$\frac{\partial z_s}{\partial t}(1+\frac{1}{U_o'}\frac{dU_o'}{dt}) = u_z(\rho_s, z_s) \qquad (45)$$

We use a second order Runga-Kutta method to compute ρ_s and z_s at $t+\Delta t$. Since we are only interested in the steady state for which $\underline{n}\cdot\underline{u}=Un_z$, we do not include the factor $(1+(dU'_0/dt)/U'_0)$ in the computations. As the particle deforms and the node points become repositioned at time $t+\Delta t$ to $\rho_s(t+\Delta t)$ and $z_s(t+\Delta t)$, the arc lengths of the node points for the deformed

figure are obtained by approximating the arc lengths of individual segments by $(\rho_{i+1}-\rho_i)^2+(z_{i+1}-z_i)^2$. The arc lengths are now no longer equal, as the node points convect to one end of the particle. After several steps, when the distance between node points at the back end becomes too small, the arc is redivided into equal segments.

Once the node points of new shape are obtained, the node positions are fit with a cubic spline with the newly computed arc length as the parameter. The algorithim is repeated with Eq.(39) used to compute the surface temperature on the $t+\Delta t$ shape, and then Eq.(38) is used to compute the surface velocity from which by Eq.(45) the shape at a new time step can be computed.

To determine when the fluid particle has ceased deform and has reached steady state, we compute at each step $(\underline{u}_S\cdot\underline{n})/n_z$. Recall that at steady state this quantity is constant along the interface and is equal to he nondimensional velocity U. We terminate the computations when the values of $(\underline{u}_S\cdot\underline{n})/n_z$ at each of the node points are within five percent of each other. The step size Δt and the number of steps required to obtain numerically accurate, converged steady solutions depends on the size of the particle relative to the tube radius (i.e. a'/b'). Some general trends we have observed are as follows: The larger the capillary number, the more deformable is the surface, and larger time steps can be used although more steps are necessary to reach steady state. Similarly, the larger a'/b' is, the greater is the hydrodynamic force arising from the interaction of the particle surface with the wall. This force tends to deform the drop, and consequently as a'/b' increases larger steps can be used. Again more steps will be

required to reach steady state. Time steps are dependent on the value of a'/b' and the capillary number. In all cases, the change in the volume of a drop was less than 0.5% through the computation, and this is an index of the accuracy of the calculations. All calculations were performed on 2100, 3100 and 5000 DEC. stations and a SUN-2 Sparc Station.

IV.4. Results for Buoyancy Driven Motion as Verification of Boundary Integral Calculation

In order to verify our solution method, we first solve for the case of buoyancy driven motion in a vertical tube. The equations presented in Section 2. can easily be recast for buoyancy driven motion: For this case, velocities are nondimensionalized by the Hadamard-Rybicynski terminal velocity ($U'_o=\Delta\rho' g a'^2 (1+\kappa)/(3\mu'^{(2)}(1+3\kappa/2))$, were $\Delta\rho'$ is the density difference and g is the acceleration of gravity). In addition, tangential stresses match at the interface, and the force F_i is equal to:

$$F_i = n_i[(\nabla_s \cdot n_i)/Ca - 3z_x(b'/a')^2(1+1.5\kappa)/(1+\kappa)] \qquad (46)$$

were Ca is, as before, $\mu^{(2)}U'_o/\sigma'$, where σ' denotes the constant surface tension.

We first examine isolated drops. We found that, in agreement with Pozrikidis (1992), interactions between drops ceased for L'/a' equal to or greater than 6, and therefore the isolated drop simulations use L'/a'=6. The node number was 48, and the time step was 0.005-0.01. Simulations were

undertaken for two values of Ca (0.5 and 1.5) and four values of a'/b', all corresponding to compact fluid particles (a'/b'=0.4,0.5,0.6, and 0.8). In Fig.1, the non-dimensional steady velocity (U'/U'_o) is plotted as a function of a'/b' for the two different values of the capillary number. Also plotted, as the continuous line, are the results for U'/U'_o assuming the particle has a spherical shape. This curve was obtained using the collocation method as described in the previous chapter. Note that for Ca=0.5 and a'/b'=0.4,0.5 and 0.6, the terminal velocity of the deformable particle is equal to that of the undeformable spherical particle. The reason for this is a combination of two effects: First, the capillary number is small, and surface tension forces tend to dominate and keep the particle spherical. Second, the value of a'/b is small enough that the hydrodynamic interaction of the particle with the wall - an interaction which causes the particle to elongate - is not strong enough to deform the particle. This is confirmed by the examination of the particle shapes which are essentially spheres. For Ca=0.5, only as a'/b' reaches a value of 0.8 do we see the particle-wall interaction becoming large enough to distend the particle. In Fig.4, the sequence of shapes starting from a sphere and leading to the steady, deformed shape is shown for Ca=0.5 and a'/b'=0.8, and the elongation is evident. Note that the velocity for this case is larger than the sphere velocity as the elongation of the drop moves the interface away from the wall and reduces the hydrodynamic interaction. For Ca=1.5, surface tension forces are not as strong, and for all four values of a'/b', the velocity is higher than the corresponding spherical ones, with elongation increasing with a'/b'. The significant deformation for Ca=1.5 and a'/b'=0.6 and 0.8 is given in Figs.5(a)

and 5(b), shown again as a sequence of deformations from a spherical initial state. All these results are in agreement with the those of Pozrikidis (1992) for isolated drops.

We next examine the effect of hydrodynamic interaction between the drops by reducing L'/a' from 6 to 3.0 and finally to 2.5. Steady shapes of interacting drops are presented for a'/b'=0.8, and Ca=0.5 and Ca=1.5 for L'/a'=3 in Figs.6(a) and (b) and L'/a'=2.5 in Figs.7(a) and (b). As expected the deformation is greater for the higher capillary number since surface tension forces are reduced relative to viscous forces for increasing Ca. More interesting are the velocity results: We find that for this large value of a'/b', the velocity only increases slightly with L'/a' for fixed Ca. For Ca=0.5, the relative velocity is 0.033 for L'/a'=3 (Fig.6(a)) and 0.034 for L'/a'=2.5 (Fig.7(a)), as compared to the noninteracting velocity of 0.032 for L'/a'=6. Similarly, for Ca=1.5, the velocity for L'/a'=3 is equal to 0.066 (Fig.6(b)) and for L'/a'=2.5 is 0.068 (Fig.7(b)), and for the noninteracting case it is 0.061. From these results it appears that the increase in velocity with L'/a' is greater the greater the capillary number. Similar conclusions have also been obtained in other studies: Hyman and Skalak (1972 (a) and 1972 (b)) studied the movement of a train of compact fluid spheres (i.e. zero capillary number) in tubes; they find that as L'/a' decreases, the velocity increases. They also find that this increase with interaction is most pronounced for small drops, and gradually diminishes as a'/b' increases. For a'/b'>0.5, the increase is only a few percent. (These results were also obtained by Wang and Skalak (1969) for solid spheres.) Hyman and Skalak (1972 (b)) and Pozrikidis (1992) studied the movement of deformable fluid particles in

tubes. Pozrikidis (1992) obtained results for a wide range of a'/b', and found that the train velocities of deformable particles, at fixed Ca, has the same behavior on L'/a' and a'/b' as was found for spherical particles. Hyman and Skalak (1972 (b)) only studied compact drops for a'/b' equal to 0.5 and 0.7, and found only a slight increase in velocity as L'/a' decreases. Pozrikidis (1992) also found that the difference between the velocity of a deformable drop and a sphere (with the same value of a'/b') increases as L'/a' decreases, and this increase becomes more pronounced as a'/b' decreases.

Now we discuss the shape of the deformed fluid particle. The difference between the values of the normal component of the total stress (σ_{rr}) at the surface of the sphere as approached from the outer and inner sides is of the form

$$\left(\sigma_{rr}^{(2)}-\sigma_{rr}^{(1)}\right)\Big|_{\rho=a'}= p_0^{(1)}-p_0^{(2)}-ga'\cos\theta(\rho^{(2)}-\rho^{(1)})$$
$$+\left[-p^{(2)}+\tau_{rr}^{(2)}+p^{(1)}-\tau_{rr}^{(1)}\right]\Big|_{\rho=a'}$$

where the term in the bracket is the hydrodynamic force due to a particle moving with velocity U'_0. When the sphere is moving steadily in an infinite medium, with the velocity of translation then being given by $U'_0=(\rho^{(1)}-\rho^{(2)})ga'^2\,(1+\kappa)/(3\mu'^{(2)}(1+3\kappa/2)$, it is easy to show that the hydrodynamic part of the normal stress $\left[-p^{(2)}+\tau_{rr}^{(2)}+p^{(1)}-\tau_{rr}^{(1)}\right]\Big|_{\rho=a'}=3\mu^{(2)}\cos\theta U_0'(1+3\kappa/2)/a'(1+\kappa)$ is balances by the gravity term, and the normal components of the total stress differ only by

a constant quantity $p_0^{(1)} - p_0^{(2)}$. Thus there is no tendency for the stresses at the interface to deform the sphere and it is not in fact necessary to suppose that the effect of surface tension is so strong as to keep the fluid particles spherical; surface tension enters only through the relation $p_0^{(1)} - p_0^{(2)} = 2\sigma / a$ determining $p_0^{(1)}$. But, when a fluid particle is in a tube, the normal components of stress difference is not constant any more. Because the particle velocity decreases, the magnitude of $\left[-p^{(2)} + \tau_{rr}^{(2)} + p^{(1)} - \tau_{rr}^{(1)}\right]_{\rho=a'}$ decreases and the total normal stress difference $\left[\sigma_{rr}^{(2)} - \sigma_{rr}^{(1)}\right]_{\rho=a'}$ becomes smaller at the leading edge, and larger at the back. This force tends to distend and elongate the particle. The hydrodynamic force decreases from the interaction of the particle surface with the wall. The normal components of stress difference at the front of the particle is less than one at the back of the particle, therefore the front end of the particle is squeezed into the tube center most and the radius of curvature at the front of the of the particle has become smaller.

IV. 5 Thermocapillary Results

We begin our investigation of the effect of interfacial deformability on thermocapillary migration in tubes by examining compact drops and two values of the conductivity ratio, k=0 and k=1. Recall from our discussion in Sec.IV.2 that in thermocapillarity, the capillary number represents the characteristic change in surface tension on the drop surface relative to the mean tension $\sigma_m'(\Delta\sigma' / \sigma_m' = a' \nabla' T_\infty' (\partial\sigma' / \partial T')|_{T_\infty'} / \sigma_m')$ divided by the factor

$(1+3\kappa/2)(2+k)$. To be consistent with the assumption that the temperature dependence of the surface tension can be described by only a linear term, $\Delta\sigma'/\sigma'_m$ must be less than one. Since $Ca=(\Delta\sigma'/\sigma'_m)/((1+3\kappa/2)(2+k))$, $\Delta\sigma'/\sigma'_m=Ca(1+3\kappa/2)(2+k)$ and therefore values of Ca selected must be small enough that when multiplied by $(1+3\kappa/2)(2+k)$ the product is less than one. We choose a value for Ca of 0.05 which results in a 0.375 relative change in tension for k=1, and a 0.25 relative change for k=0.

Consider first the case of k=1. Listed in table 1 are values for the relative velocity for a'/b'=0.1 to 0.8 in increments of 0.1; also given are the relative velocities for this range of a'/b' for undeformable particles (Ca=0 obtained by collocation in Chapter III). We note from the table that only for the largest particle (a'/b'=0.8) is the deformable velocity different from the undeformable one. This result is clearly a consequence of the fact that the capillary number is very small, and surface tension forces causes the particle to remain a sphere. Only for the largest value of a'/b' are the hydrodynamic stresses caused by the close proximity of the particle to the wall large enough to deform the particle and change the velocity. The interface contour for a'/b'=0.8 and k=1 is given in Fig 8(a) and the results indicate that the drop is squeezed in the front end. We shall discuss the reasons for this deformation in the following paragraph. We note here that because of the increase in the gap thickness, the hydrodynamic resistance is decreased and this is the reason why the velocity has increased from the spherical value (see table 1). The velocities for the deformed particles (Ca=0.05) are plotted alongside the Ca=0 (undeformable) particles in Fig.9(a) and compared to the buoyancy results of the previous section. We

note that the increase in velocity with capillary number is larger for thermocapillary motion than it is for buoyancy.

We now discuss the shape of the deformed fluid particle. The normal stress difference is given by

$$\left(\sigma_{rr}^{(2)}-\sigma_{rr}^{(1)}\right)\Big|_{\rho=a'}= p_0^{(1)}-p_0^{(2)}+\left[-p^{(2)}+\tau_{rr}^{(2)}+p^{(1)}-\tau_{rr}^{(1)}\right]\Big|_{\rho=a'}$$

From our discussion in Chapter 3, we note that conceptually the term in square bracket consists two parts, one is the thermocapillary surface tension stress $\tau_{rr}(\partial\sigma/\partial T)$ without hydrodynamic flow at infinity, and other is the hydrodynamic stress $\tau_{rr}(U_0')$ due to a particle moving with velocity U'_0 without thermocapillary migration. In an infinite medium, the hydrodynamic force just balances the variation in the surface tension force. When a fluid particle is in the tube, the hydrodynamic interaction of the particle with the wall reduces the velocity and therefore the magnitude hydrodynamic part of the normal stress decreases. The magnitude surface tension part of the normal stress increases, since the pressure required to drive the recirculation flow increases. Thus the total normal stress difference $\left[\sigma_{rr}^{(2)}-\sigma_{rr}^{(1)}\right]\Big|_{\rho=a'}$ at the front of the particle is smaller and at the back is larger, and the front end of the particle is squeezed and the back end is rounded, and the radius of curvature at the front of the particle has become smaller.

Consider next the case for k=0. Here we have an additional effect in that the surface tension force $\tau_{rr}(\partial\sigma/\partial T)$ is larger because the temperature gradient is larger, and this causes a larger pressure gradient and a greater

value for the magnitude component $\tau_{rr}(\partial\sigma/\partial T)$ of the normal stress. Therefore we expect the particle to be more deformed. Fig.8(b) gives the deformation for k=0, and a'/b'=0.8 and we note that it is larger than the k=1 case, in the sense that the radius of curvature at the front (leading end) of the particle has become smaller and at the back has become larger. Because of the change in shape the particle velocity is again larger than the sphere case (Table 2), we expect the temperature gradient along the surface to be reduced in the front region and increased in the back region relative to the sphere values. Fig.10 plots the temperature gradient along the particle surface (for Ca=0.05 and Ca=0) as a function of the arc length, and the changes in gradient at the front and back ends are evident. We note that since the particle is squeezed the most for the k=0 case, the particle velocity relative to the sphere value should be larger for the k=0 case, since the hydrodynamic interaction is also reduced. In Fig.9(b) we plot the velocity for k=0 for both thermocapillary and buoyancy driven motion, and we see that the deformable particle moves faster. Thus the reduction in the wall hydrodynamic interaction predominates.

IV.6 Conclusions

In this chapter we have studied the effect of deformation on the thermocapillary migration of particles. Because of the use of a linear relationship between the temperature and the surface tension, the range of capillary numbers allowed must be small, and we undertook calculations for Ca=0.05. For this value, only for large particles (a'/b'>0.8) is deformation

significant. For these values of a'/b', hydrodynamic stresses squeeze the particle, reduce the interaction of the particle with the wall and thereby increases the terminal velocity. For small particles a'/b'<0.8 and Ca=0.05 the fluid particles translate as spheres, due to the fact that the fluid particle is too far away from the wall to be subject to distending hydrodynamic stresses.

Future research on deformation should consider fluid slugs (a'/b'>1). Although we have undertaken some boundary integral calculations for this case, the results are not encouraging. In these slug calculations an initial shape consisting of a cylinder with two hemispherical ends with radii 0.7(of the tube radius) were used. However after a few thousand steps, the solution had not yet converged, although the results were converging and the numerical scheme was stable. The problem is that the initial shape is too far from the solution shape, thereby necessitating a large number of steps. One solution is to develop asymptotic solutions for the shape of a slug in a tube moving under thermocapillary force at low Ca, and then use this solution as the initial guess.

Another future direction of research in the inclusion of nonlinear equations for the dependence of surface tension on temperature. Such a formulation would allow large capillary numbers, and thereby enhance the deformation.

Appendix A

Derivation of the Green's Function For a Ring in an Infinite Medium

Ladyzhenskaya (1969) gives the following Cartesian solution for the velocity component in the j direction at the point with vector position $\underline{x}$ due to a point force applied in the i direction at a particular position $\underline{y}$ in an infinite medium:

$$u_j^i(\underline{x},\underline{y}) = -\frac{1}{8\pi}\left[\frac{\delta_{ij}}{|\underline{x}-\underline{y}|} + \frac{(x_i - y_i)(x_j - y_j)}{|\underline{x}-\underline{y}|^3}\right] \qquad \text{(A.1)}$$

where $|\underline{x}-\underline{y}|$ is the distance between the points $\underline{x}$ and $\underline{y}$. From this expressions we can obtain the relation for the velocity at the field point $\underline{x}$ due to a ring of point forces by integrating about the ring the velocities generated at $\underline{x}$ by each point force on the ring. Using cylindrical coordinates (z_x,ρ_x,ω_x) to locate the field point and cylindrical coordinates (z_y,ρ_y,ω_y) to locate a point force on the ring, the velocity at $\underline{x}$ due to the ring assembly are (Fig.11):

$$\begin{aligned} U_z^z &= \int_o^{2\pi} u_3^3 d\omega_y \\ &= -\frac{1}{8\pi}\int_o^{2\pi} \frac{1}{\rho_{xy}^3}\left[\rho_x^2 + \rho_y^2 - 2\rho_x\rho_y\cos(\omega_x - \omega_y) + 2z^2\right] d\omega_y \\ &= -\frac{1}{4\pi}\frac{k}{(\rho_x\rho_y)^{1/2}}\left[F(k) + \frac{z^2}{d^2}E(k)\right] \end{aligned}$$

$$U_{\rho}^{z} = \int_o^{2\pi} (u_1^3 \cos\omega_x + u_2^3 \sin\omega_x) d\omega_y$$
$$= -\frac{1}{8\pi}\int_o^{2\pi} \frac{z}{\rho_{xy}^3}\left[\rho_x - \rho_y \cos(\omega_x - \omega_y)\right] d\omega_y$$
$$= -\frac{z}{8\pi}\frac{k}{(\rho_x)^{3/2}(\rho_y)^{1/2}}\left[F(k) + (\rho_x^2 - \rho_y^2 - z^2)\frac{E(k)}{d^2}\right]_]$$

$$U_{z}^{\rho} = \int_o^{2\pi} (u_3^1 \cos\omega_y + u_3^2 \sin\omega_y) d\omega_y$$
$$= -\frac{1}{8\pi}\int_o^{2\pi} \frac{z}{\rho_{xy}^3}\left[\rho_x \cos(\omega_x - \omega_y) - \rho_y\right] d\omega_y$$
$$= \frac{z}{8\pi}\frac{k}{(\rho_x)^{1/2}(\rho_y)^{3/2}}\left[F(k) - (\rho_x^2 - \rho_y^2 + z^2)\frac{E(k)}{d^2}\right]$$

$$U_{\rho}^{\rho} = \int_o^{2\pi}\left[(u_1^1 \cos\omega_y + u_1^2 \sin\omega_y)\cos\omega_x + (u_2^1 \cos\omega_y + u_2^2 \sin\omega_y)\sin\omega_x\right] d\omega_y$$
$$= -\frac{1}{8\pi}\int_o^{2\pi}\left\{\frac{1}{\rho_{xy}}\cos(\omega_x - \omega_y) - \frac{1}{\rho_{xy}^3}\left[\left(\rho_x^2 + \rho_y^2\right)\cos(\omega_x - \omega_y)\right.\right.$$
$$\left.\left.-\rho_x\rho_y(1 + \cos^2(\omega_x - \omega_y))\right]\right\} d\omega_y$$
$$= -\frac{1}{8\pi}\frac{k}{(\rho_x\rho_y)^{3/2}}\left\{(\rho_x^2 + \rho_y^2 + 2z^2)F(k)\right.$$
$$\left.-\left[2z^4 + 3(\rho_x^2 + \rho_y^2)z^2 + (\rho_x^2 - \rho_y^2)^2\right]\frac{E(k)}{d^2}\right\} \qquad \text{(A.2)}$$

where $z=z_x-z_y$, $k=[4\rho_x\rho_y/(z^2+(\rho_x+\rho_y)^2)]^{1/2}$, $d^2=(z_x-z_y)^2+(\rho_x-\rho_y)^2$ and F(k) and E(k) are complete elliptic integrals (Abramowitz & Stegun 1972) of first and second kinds, respectively. In the above, the superscript denotes the direction of the force at the ring (source) point and the subscript denotes the direction of the velocity component at the field point, $\underline{x}$. We note that these Green's functions are axisymmetric as they do not depend on ω_x.

Appendix B

Derivation of Complementary Green's Function
to Satisfy No-Slip Tube Wall Condition

The complementary component of the tube Green's function satisfies zero force everywhere in the tube. The general axisymmetric solution, as a Fourier integral, is given by Eq.(15) in the text in terms of unknown functions A1(t), B1(t), A2(t) and B2(t). These solutions in Eq.(15), evaluated at the tube wall, must match the values for the velocities at the wall as given by the solutions for the velocities due to a ring in an infinite medium (Eq.(14)). By expressing these velocities as Fourier integrals (Eqs.(16a, b) and (17) of the text), and equating these Fourier representations to the Fourier solutions, the undetermined functions in Eq.(15) can be obtained.

$$
\begin{aligned}
&A1(t)tI_0(t\rho_o)+B1(t)[\rho_o tI_1(t\rho_o)+2I_0(t\rho_o)]=-g_z^z\\
&A1(t)tI_1(t\rho_o)+B1(t)\rho_o tI_0(t\rho_o)=-g_\rho^z\\
&A2(t)tI_0(t\rho_o)+B2(t)[\rho_o tI_1(t\rho_o)+2I_0(t\rho_o)]=-g_z^\rho\\
&-A2(t)tI_1(t\rho_o)-B2(t)\rho_o tI_0(t\rho_o)=-g_\rho^\rho
\end{aligned}
\qquad \text{(B.1)}
$$

The function A1(t), A2(t), B1(t) and B2(t) are given below by solving from these equations,

$$A1(t)=\frac{1}{2\pi C1}\Big[-\rho_o^2 tI_0(\rho_y t)(I_0K_1+I_1K_0)$$
$$+\rho_y I_1(\rho_y t)[\rho_o t(I_0K_0+I_1K_1)+2I_0K_1]\Big]$$
$$B1(t)=\frac{1}{2\pi C1}\Big[-\rho_y tI_1(\rho_y t)(I_0K_1+I_1K_0)+I_0(\rho_y t)[\rho_o t(I_0K_0+I_1K_1)-2I_1K_0]\Big]$$
$$A2(t)=\frac{1}{2\pi C2}\Big[I_1(\rho_y t)[-(4+\rho_o^2t^2)I_0K_1-2\rho_0 t(I_0K_0+I_1K_1)-\rho_o^2t^2I_1K_0]$$
$$+\rho_y tI_0(\rho_y t)[\rho_o t(I_0K_0+I_1K_1)+2I_0K_1]\Big]$$
$$B2(t)=\frac{1}{2\pi C3}\Big[I_1(\rho_y t)[\rho_o t(I_0K_0+I_1K_1)+2I_0K_1]-\rho_y tI_0(\rho_y t)(I_0K_1+I_1K_0)\Big] \tag{B.2}$$

where $C1=\rho_o tI_0^2-\rho_o tI_1^2-2I_0I_1$, C2=-tC1 and C3=-C1; $I_0=I_0(\rho_0 t)$, $I_1=I_1(\rho_0 t)$, $K_0=K_0(\rho_0 t)$, and $K_1=K_1(\rho_0 t)$

With the constants known, we can express the complementary solution in the form given by Eq.(18) of the text, where f_j^i appearing in Eq.(18) are defined below.

$$f_z^z=A1(t)tI_0(t\rho)+B1(t)[\rho tI_1(t\rho)+2I_0(t\rho)]$$
$$f_\rho^z=A1(t)tI_1(t\rho)+B1(t)\rho tI_0(t\rho)$$
$$f_z^\rho=A2(t)tI_0(t\rho)+B2(t)[\rho tI_1(t\rho)+2I_0(t\rho)]$$
$$f_\rho^\rho=A2(t)tI_1(t\rho)+B2(t)\rho tI_0(t\rho) \tag{B.3}$$

Appendix C

Expressions for the Green's Function gradient Appearing in the Temperature Boundary Integral Equation

The kernel appearing in the integral of Eq.(37) is divided into complementary (Φ^t) and infinite fluid (Φ^i) parts:

$$\underline{n}(\underline{y})\cdot\nabla\Phi(\underline{x},\underline{y}) = \underline{n}(\underline{y})\cdot\nabla\Phi^i(\underline{x},\underline{y}) + \underline{n}(\underline{y})\cdot\nabla\Phi^t(\underline{x},\underline{y})$$

The infinite fluid part is given by Eq.(25); upon differentiating, the following expression obtains for the kernel:

$$\underline{n}(\underline{y})\cdot\nabla\Phi^i(\underline{x},\underline{y}) = \left[\frac{k}{4\pi(\rho_x)^{1/2}(\rho_y)^{3/2}}[F(k)-(\rho_x^2-\rho_y^2+z^2)\frac{E(k)}{d^2}\right]n_r - \left[\frac{zE(k)}{2\pi(\rho_x\rho_y)^{1/2}d^2}\right]n_z \qquad \text{(C.1)}$$

where $z=z_x-z_y$, $L^2=(z_x-z_y)^2+(\rho_x+\rho_y)^2$, $d^2=(z_x-z_y)^2+(\rho_x-\rho_y)^2$ and $k^2=4\rho_x\rho_y/L^2$.

For computational purposes, we need an expression for the kernel as $\rho_x\to 0$; taking this limit of Eq.(C.1) we obtain:

$$\underline{n}(\underline{y})\cdot\nabla\Phi^i(\underline{x},\underline{y}) = -\frac{\rho_y}{2(z^2+\rho_y^2)^{3/2}}n_\rho + \frac{z}{2(z^2+\rho_y^2)^{3/2}}n_z \qquad \text{(C.2)}$$

The second component of the kernel is obtained by differentiating Eq.(26):

$$\underline{n}(\underline{y})\cdot\nabla\Phi^{t}(\underline{x},\underline{y}) = -\left\{\frac{1}{\pi}\int_{o}^{\infty}\left[tI_1(\rho_y t)I_0(\rho_x t)K_1(\rho_o t)/I_1(\rho_o t)\right]\cos(tz)dt\right\}n_r$$
$$-\left\{\frac{1}{\pi}\int_{o}^{\infty}\left[tI_0(\rho_y t)I_0(\rho_x t)K_1(\rho_o t)/I_1(\rho_o t)\right]\sin(tz)dt\right\}n_z \qquad \text{(C.3)}$$

We note that as t tends to infinity, and as long as $\rho_x<\rho_o$, $\rho_y<\rho_o$, the integrands in Eq.(C.3) decay at the exponential rate $\exp((\rho_x+\rho_y-2\rho_o)t)$. Also as $t\rightarrow 0$ the integrands are bounded. Therefore the Fourier integrals in Eq.(C.3) exist.

Table 1

Comparisons, for compact particles, between velocities for deformable particles for Ca=0.05 (obtained by the boundary integral technique) and spherical particles (obtained by the collocation technique) (κ=k=1).

a'/b'	Boundary integral method U'/U'_0	Collocation method(Ca=0) U'/U'_0
0.1	1.00	0.99795
0.2	0.98	0.98365
0.3	0.95	0.94635
0.4	0.88	0.87773
0.5	0.77	0.77291
0.6	0.63	0.63158
0.7	0.46	0.45945
0.8	0.32	0.2708

Table 2

Comparisons, for compact, nonconductiong (k=0) particles, between velocities for deformable particles for Ca=0.05 (obtained by the boundary integral technique) and spherical particles (obtained by the collocation technique) (κ=1).

a'/b'	Boundary integral method U'/U'_0	Collocation method(Ca=0) U'/U'_0
0.1	1.00	0.9988
0.2	0.99	0.9900
0.3	0.96	0.9672
0.4	0.93	0.9250
0.5	0.86	0.8580
0.6	0.76	0.7601
0.7	0.63	0.6307
0.8	0.52	0.4724

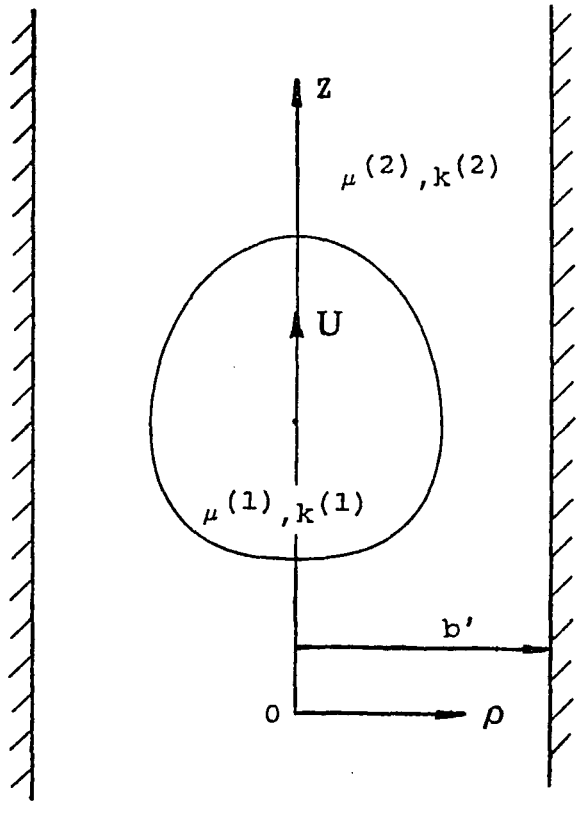

Fig.1

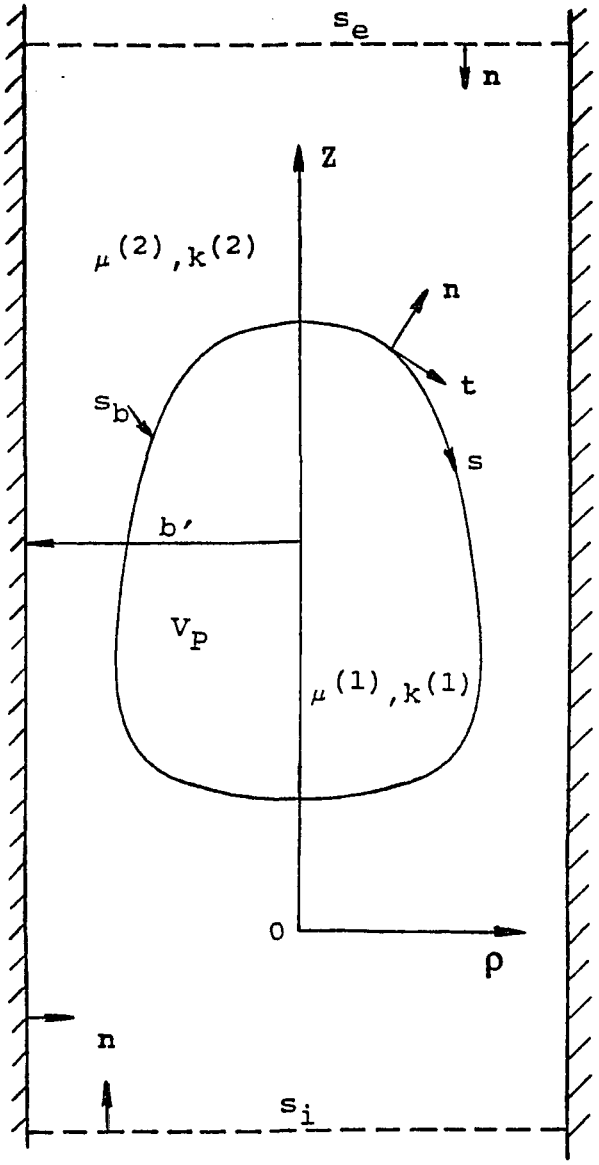

Fig.2

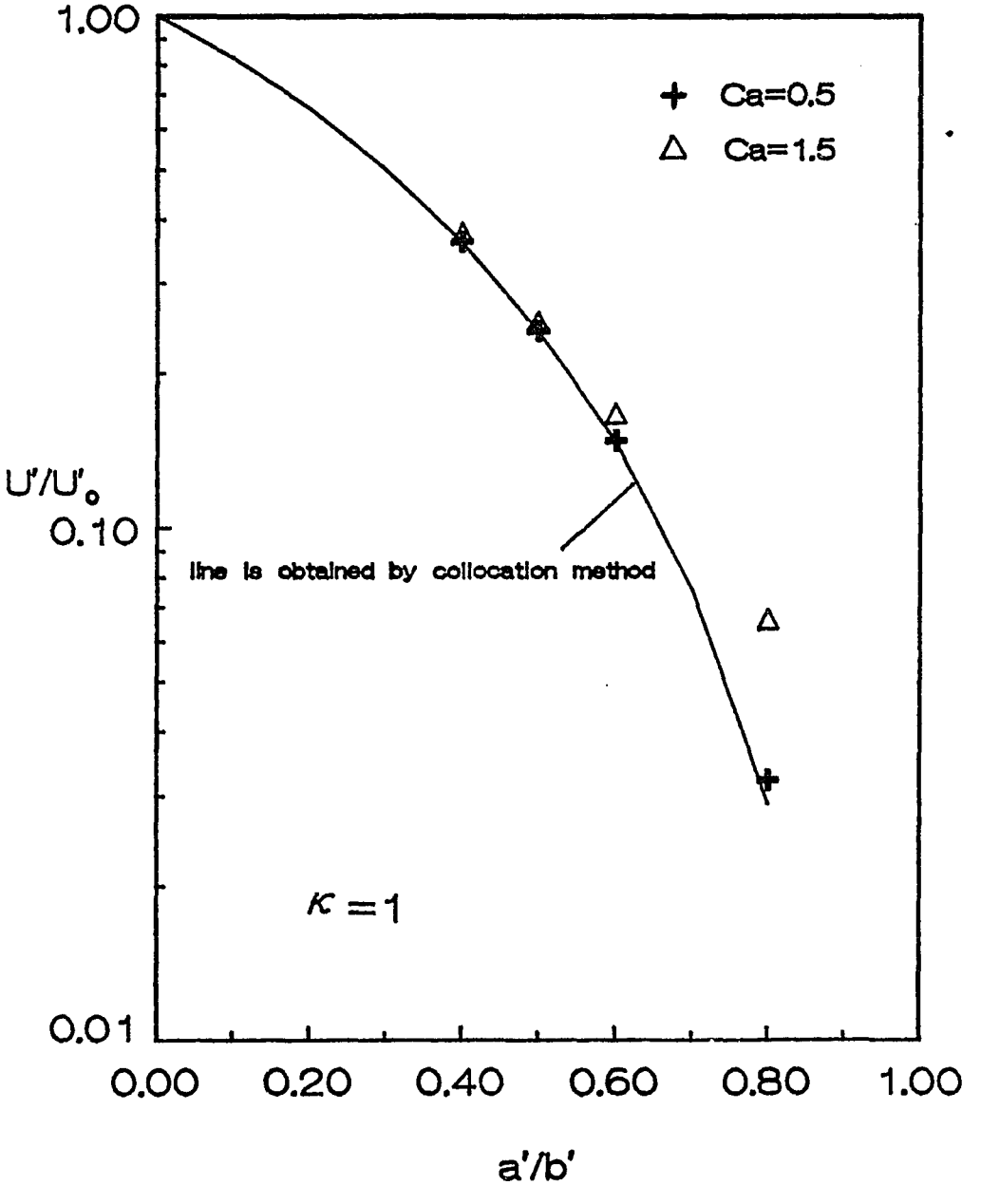
1.00
0.10
0.01
U'/U'o
Ca=0.5
Ca=1.5
line is obtained by collocation method
κ=1
0.00
0.20
0.40
0.60
0.80
1.00
a'/b'

Fig.3

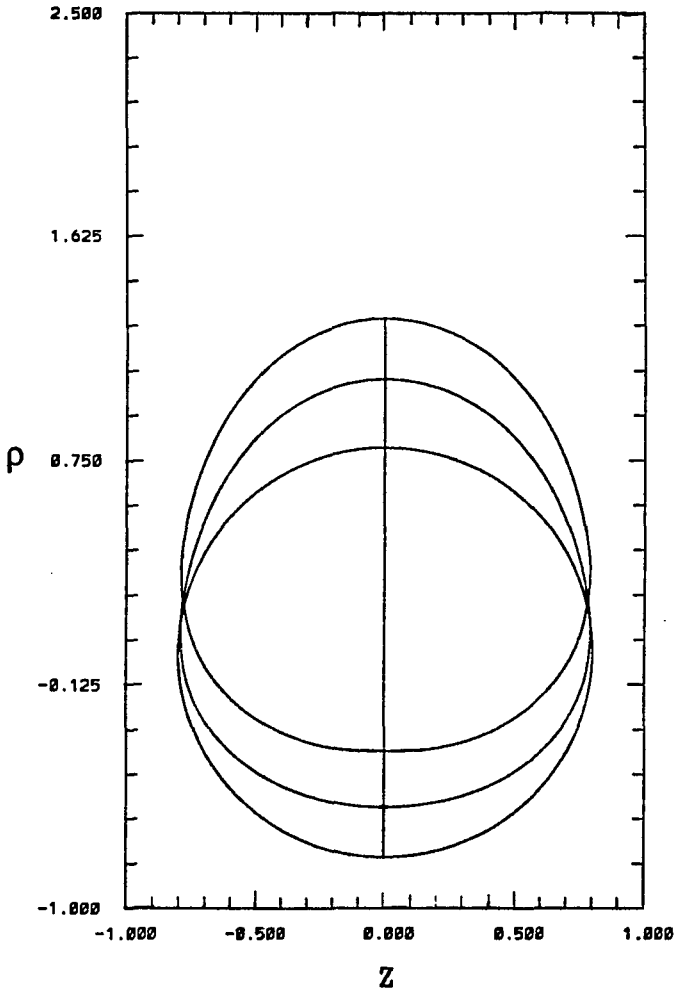

Fig.4 a'/b'=0.8, Ca=0.5, t=0, 5.5 , 12.27, L'/a'=6

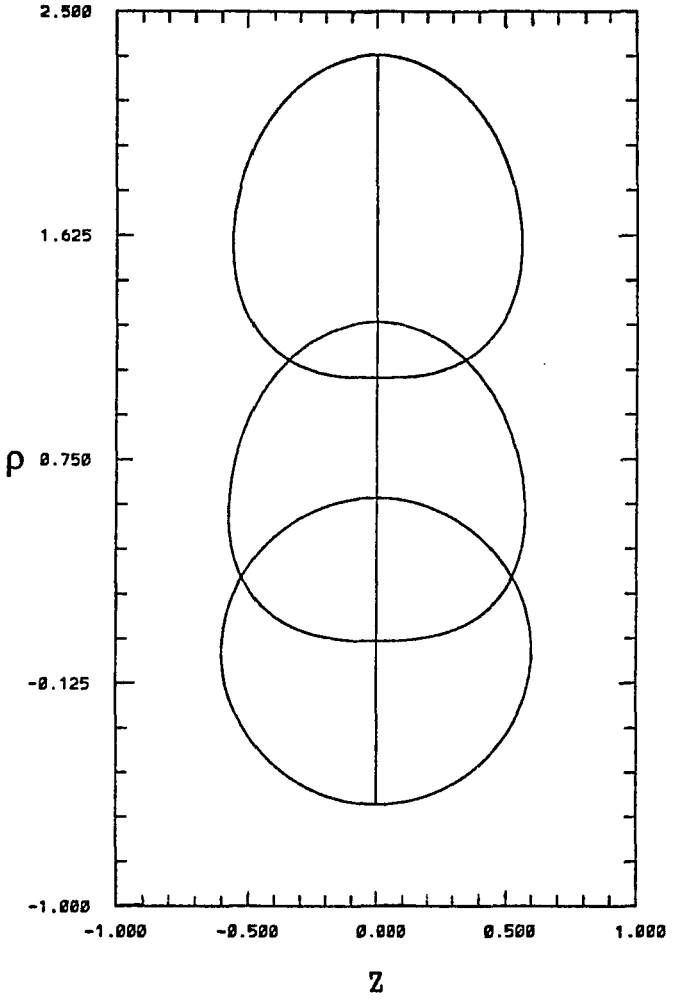

Fig.5(a) a'/b'=0.6, Ca=1.5, t=0, 4.02, 9.02, L'/a'=6

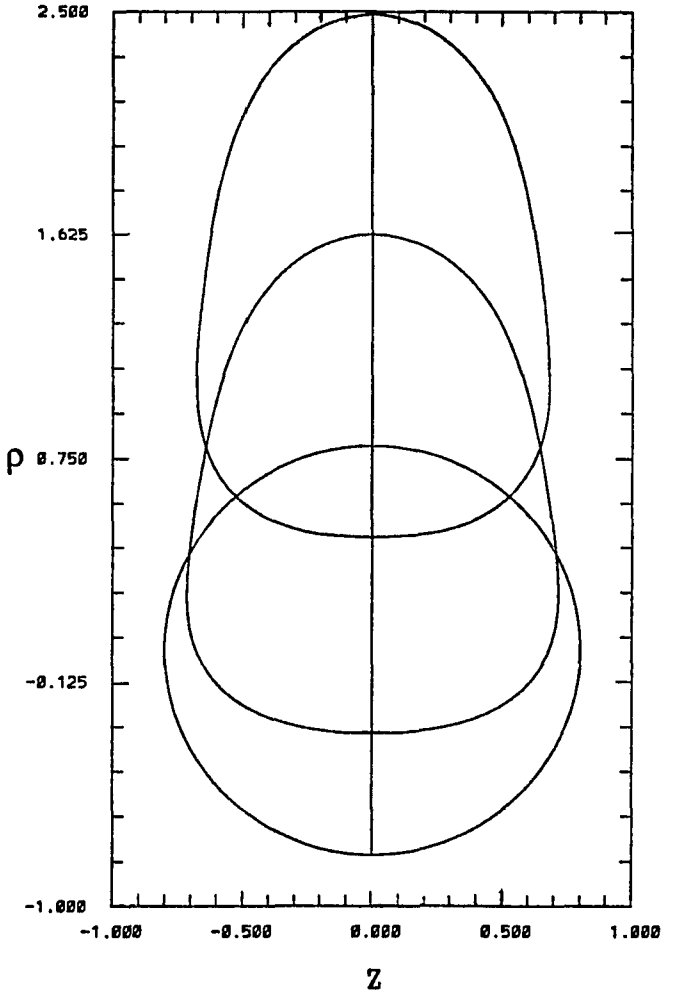

Fig.5(b) a'/b'=0.8, Ca=1.5, t=0, 12.275, 24.875, L'/a'=6

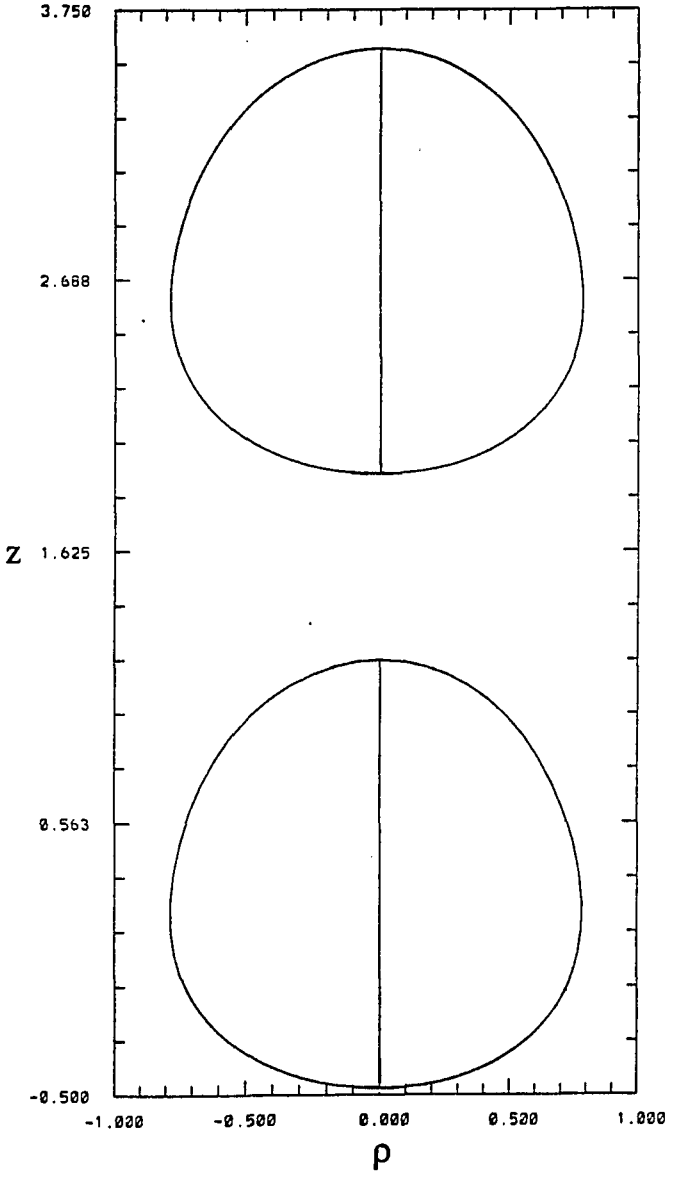

Fig. 6(a) a'/b'=0.8, Ca=0.5, L'/a'=3.0

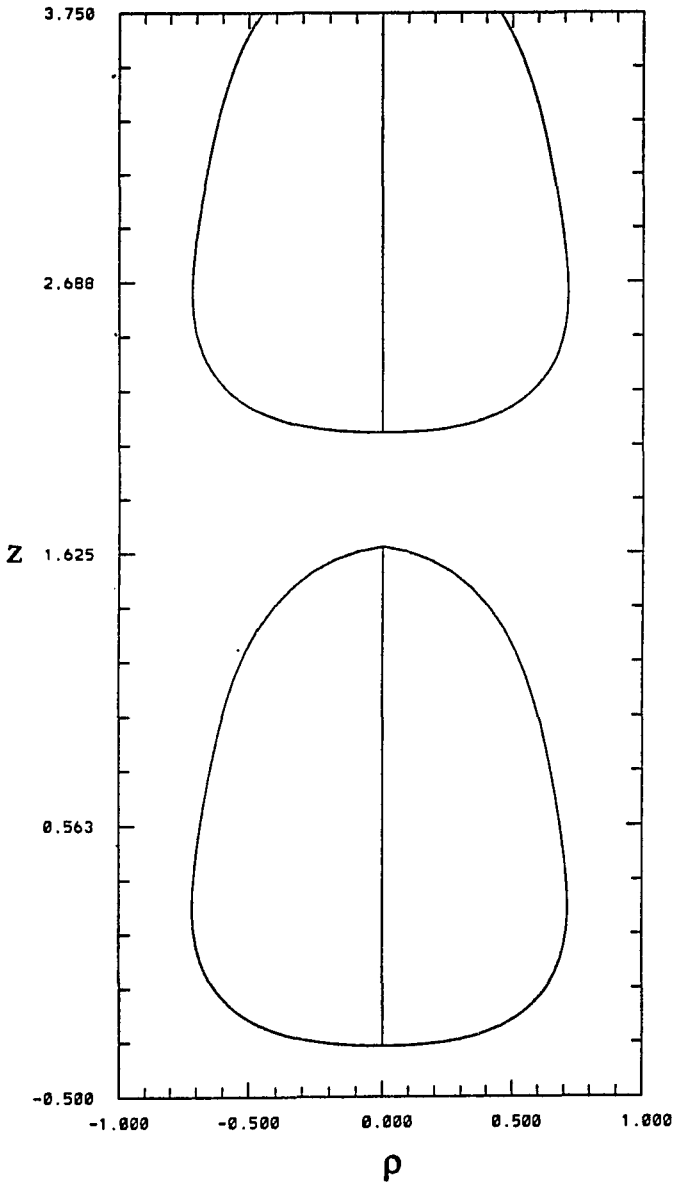

Fig. 6(b) a'/b'=0.8, Ca=1.5, L'/a'=3.0

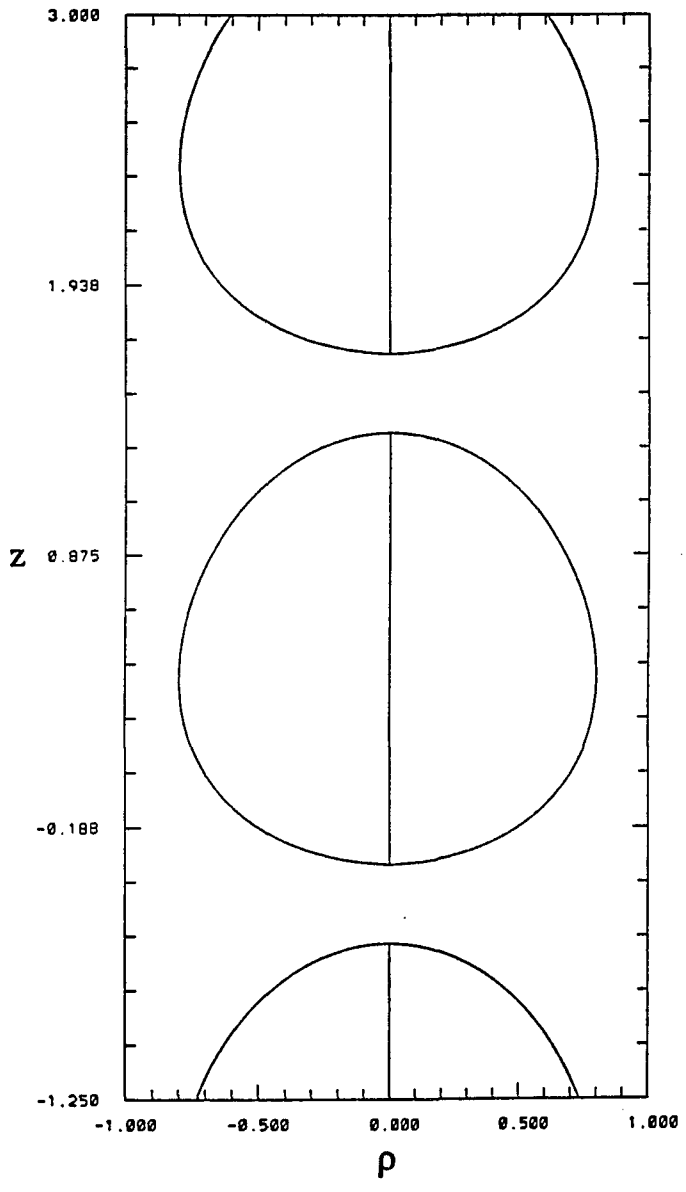

Fig. 7(a) a'/b'=0.8, Ca=0.5, L'/a'=2.5

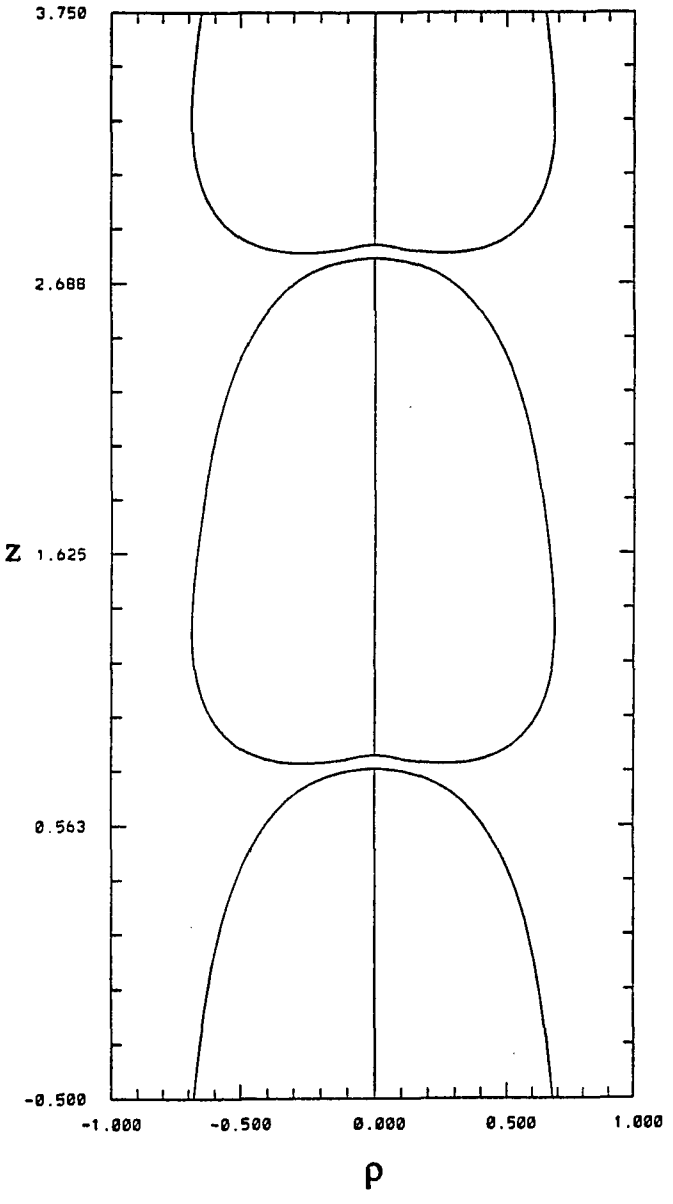

Fig. 7(b) a'/b'=0.8, Ca=1.5, L'/a'=2.5

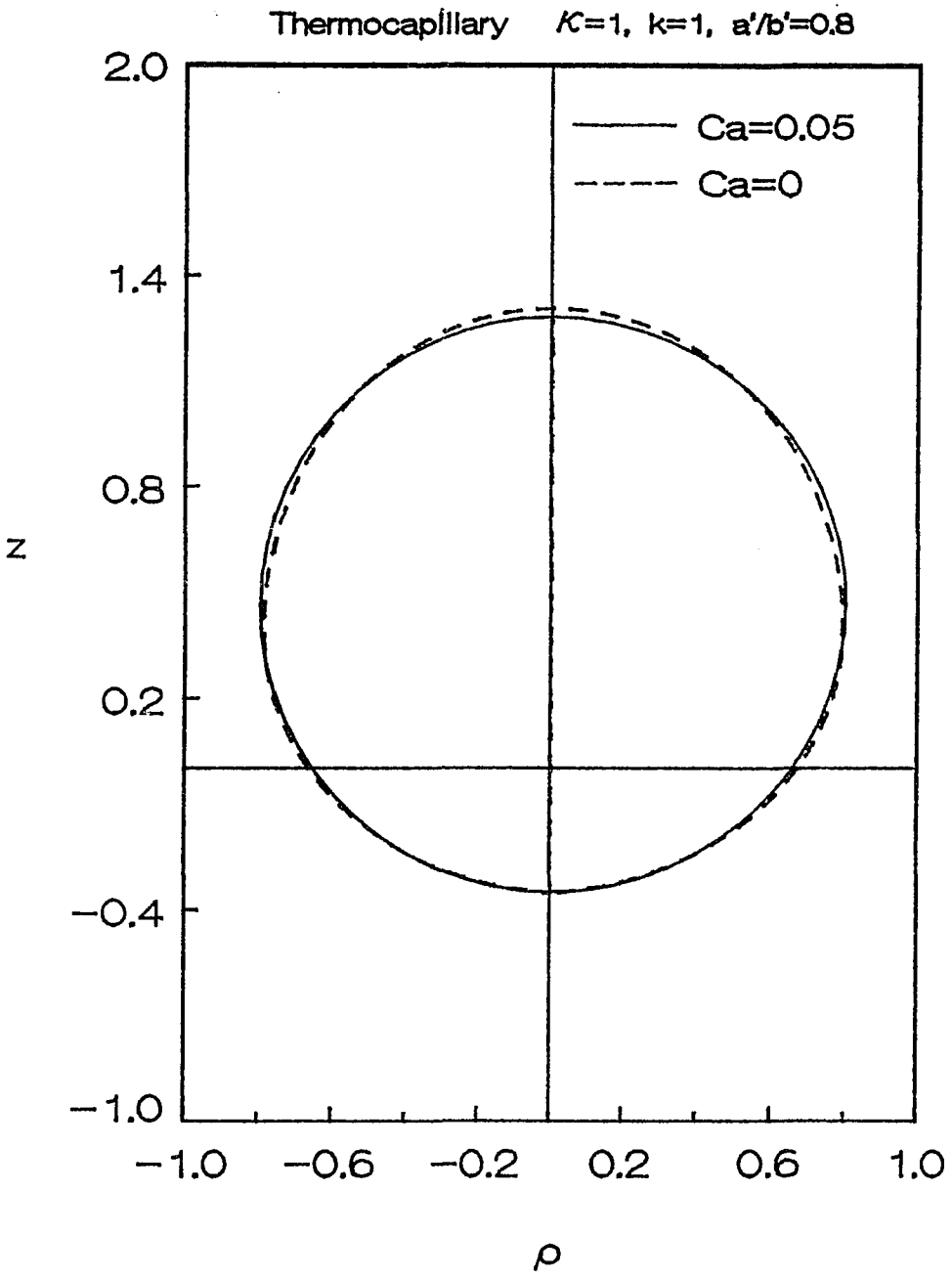
Thermocapillary Ma=1, k=1, a'/b'=0.8
Ca=0.05
Ca=0
2.0
1.4
0.8
0.2
−0.4
−1.0
z
−1.0
−0.6
−0.2
0.2
0.6
1.0
ρ

Fig.8(a)

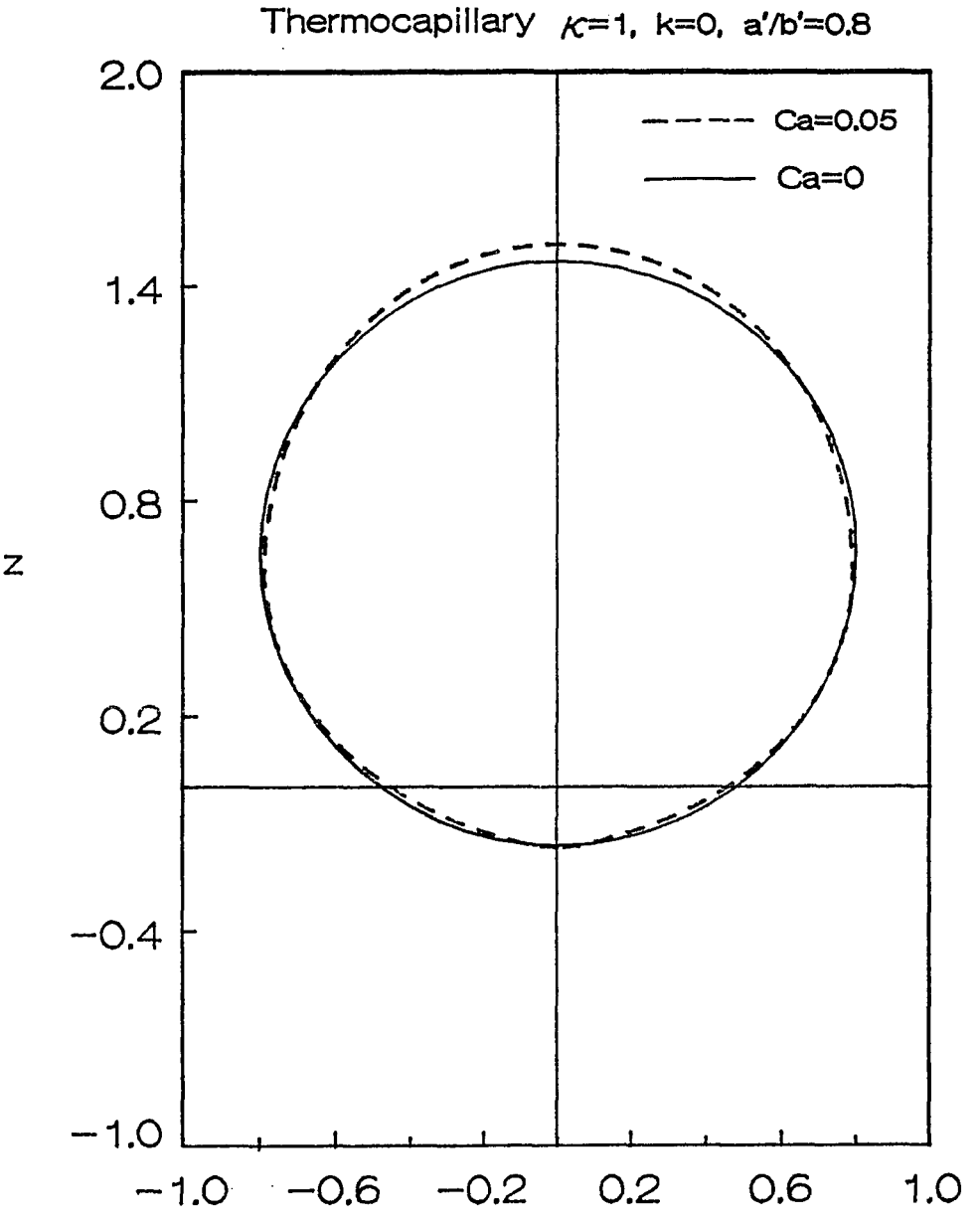
Thermocapillary κ=1, k=0, a'/b'=0.8
Ca=0.05
Ca=0
2.0
1.4
0.8
0.2
−0.4
−1.0
z
−1.0
−0.6
−0.2
0.2
0.6
1.0
ρ

Fig.8(b)

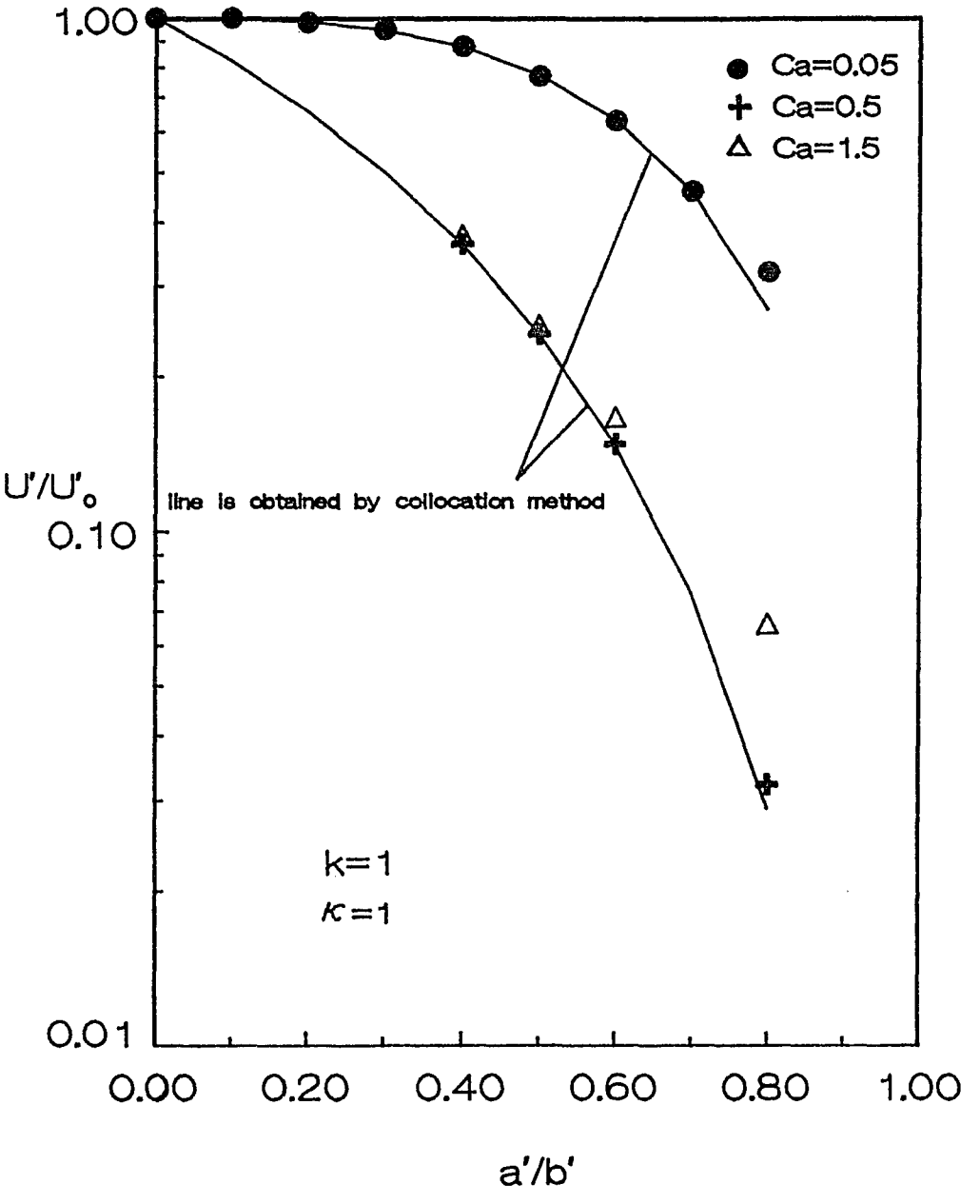
1.00
0.10
0.01
U'/U'o
Ca=0.05
Ca=0.5
Ca=1.5
line is obtained by collocation method
k=1
κ=1
0.00
0.20
0.40
0.60
0.80
1.00
a'/b'

Fig.9(a)

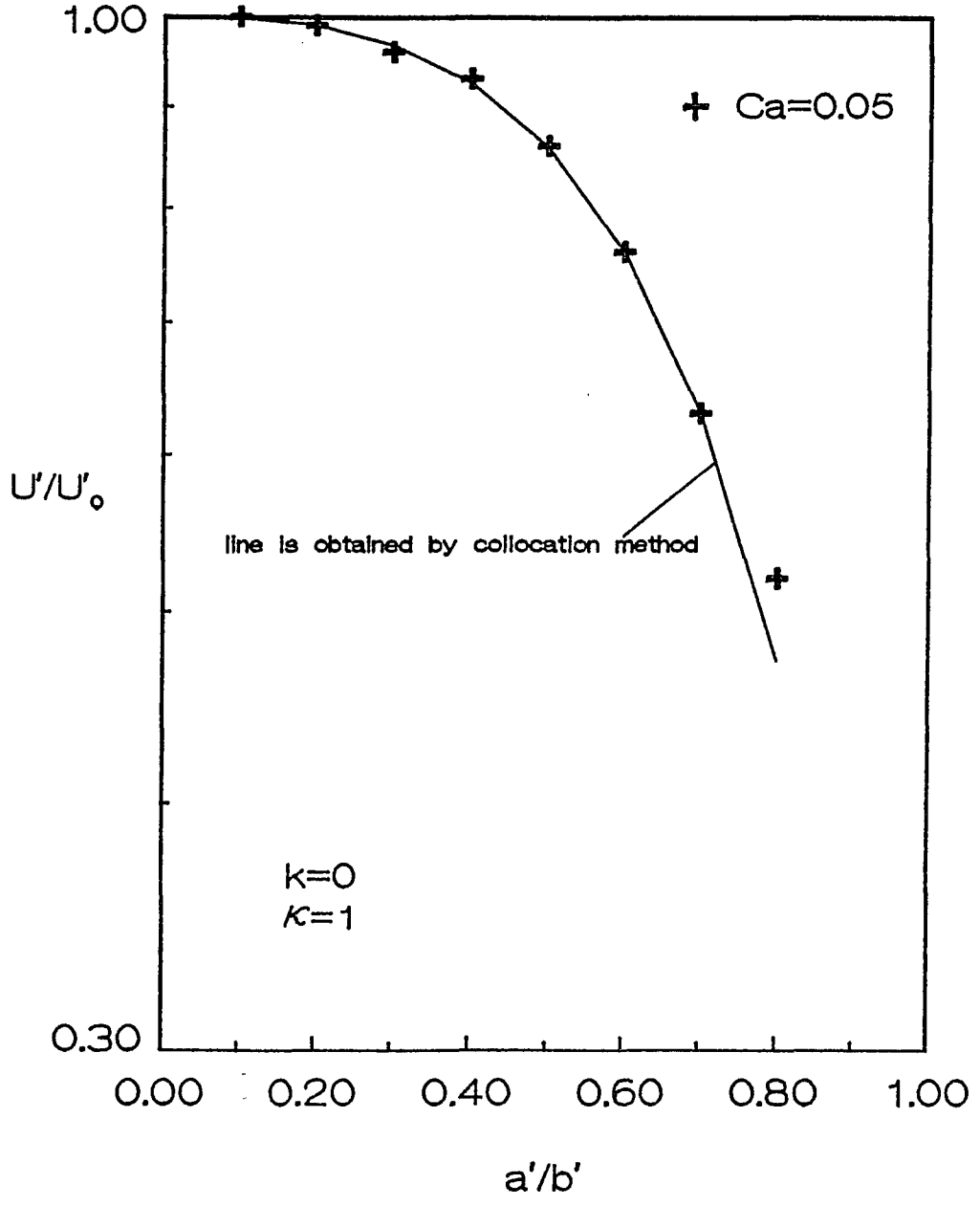
1.00
0.30
U'/U'o
Ca=0.05
line is obtained by collocation method
k=0
κ=1
0.00
0.20
0.40
0.60
0.80
1.00
a'/b'

Fig.9(b)

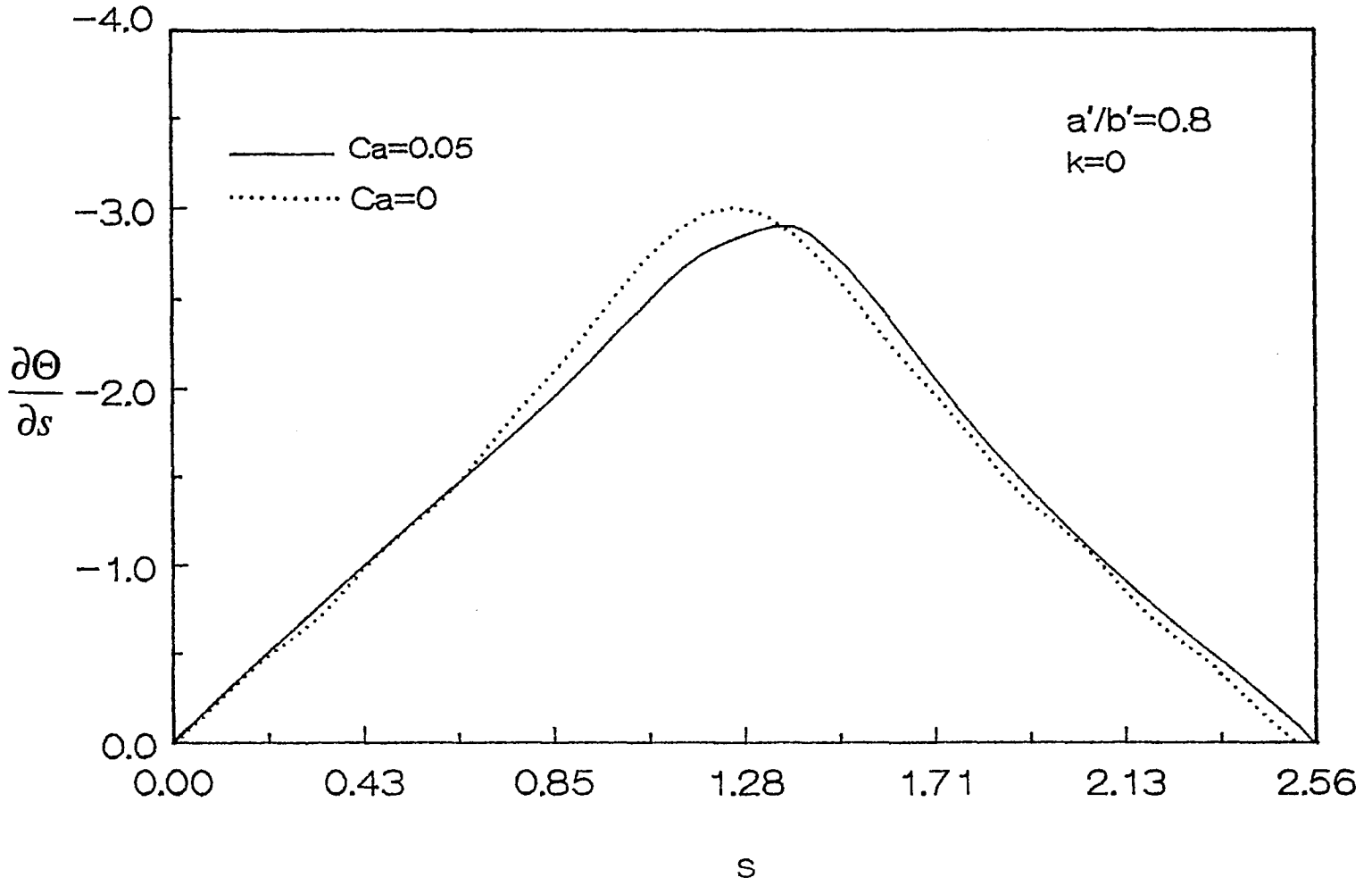

Fig.10

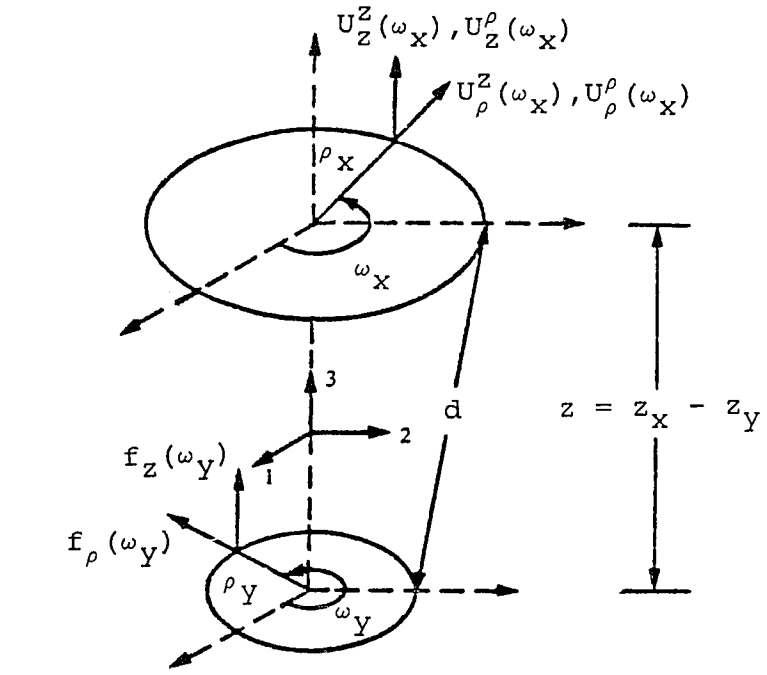

$f_\rho(\omega_y) = \cos\omega_y e1 + \sin\omega_y e2$

Fig.11

REFERENCES

1. Abramowitz, M. & Stegun, I.A. 1972 *Handbook of Mathematical functions.* Dover Publications, Inc., New York.

2. Anderson, J.L. 1985 Droplet interactions in thermocapillary motion. *Int. J. Multiphase Flow* **11**, 813.

3. Annamalai, P., Shankar, R., Cole, R. & Subramanian, R.S. 1982 Bubble migration inside a liquid drop in a space laboratory. *Applied Scientific Research* **38**, 179.

4. Ascoli, E.P. & Leal, L.G. 1990 Thermocapillary motion of deformable drop toward a planar wall. *J. Colloid Interface Sci* **138**, 220.

5. Balasubramaniam, R. & Chai, A.-T. 1987 Thermocapillary migration of droplets: An exact solution for small Marangoni numbers. *J. Colloid Interface Sci.* **119**, 531.

6. Balasubramaniam, R. & Lavery, J.E. 1989 Numerical simulation of thermocapillary bubble migration under microgravity for large Reynolds and Marangoni numbers. *Numer. Heat Transfer.* A **16**,175.

7. Barton, D. & Subramanian, R.S. 1990 Thermocapillary migration of a liquid drop normal to a plane surface. *J. Colloid Interface Sci.* **137**, 170.

8. Bergman, A., Carlberg, T., Fredriksson, H. & Stjerndahl, J. 1982 The influence of gravity on the solidification of monotectic & near monotectic Cu- Pb Alloys *In Materials Processing in the Reduced Gravity Environment of Space.* G.E. Rindone, ed.

9. Borhan, A. & Mao C.F. 1992 Effects of surfactants on the motion of a drops through circular tubes. *Phys. Fluid A.* **4**, No.12, 2628.

10. Bratukhin, Y .K. 1976 Thermocapillary drift of a viscous fluid droplet. *NASA Tech. Trans. NASA TT F* 17093

11. Chen, J.N., Dagan, Z. & Maldarelli, C. 1991 The axisymmetric thermocapillary motion of a fluid particle in tube. *J. Fluid Mech.* ***233,*** 405.

12. Chen, S.H. & Keh, H.J. 1990 Thermocapillary motion of a fluid droplet normal to a plane surface. *J. Colloid Interface Sci.* **137**, 550.

13. Davis, H. T. 1962 *Introduction to nonlinear differential and integral equations.* Dover Publications, Inc., New York.

14. Feuillebois, F. 1989 Thmocapillary migration of two equal bubbles parallel to their line of centers. *J. Colloid Interface Sci.* **131**, 267.

15. Haberman, W.L. and Sayre, R.M. 1958 Motion of rigid and fluid spheres in stationary and moving liquids inside cylindrical tubes. *David W. Taylor Model Basin Report.* No. 1143, U.S. Navy Dept.

16. Happel, H. & Brenner, H. 1973 *Low Reynolds number hydrodynamics.* Noordhoof International Pub., Leyden.

17. Hariri, H.H. Nadim, A. & Borhan, A. 1990 Effect of inertia on the thermocapillary velocity of a drop. *J. Colloid Interface Sci.* **140**, 277.

18. Hasan, M .M. & Balasubramaniam, R. 1989 Thermocapillary migration of a large gas slug in a tube. *J. Thermophysics* **3**, 87.

19. He, Z., Dagan, Z. & Maldarelli, C. 1991 The influence of surfactant adsorption on the motion of a fluid sphere in a tube. Part 1. Uniform retardation controlled by sorption kinetics. *J. Fluid Mech.* ***222,*** 1.

20. Hyman, W A. & Skalak, R. 1972a Viscous flow of a suspension of liquid dropes in a cylindrical tube. *Appl. Sci. Res.* **26**, 27.

21. Hyman, W.A. & Skalak, R. 1972b Non-Newtonian behavior of a suspension of liquid drops in tube flow. *AIChE J.* **18**, 149.

22. Keh, H.J. & Chen, S.H. 1990 The thermocapillary motion of two droplets along their line of centers. *Int. J. Multiphase Flow.* **16**, 515.

23. Kim, H.S. & Subramanian, R.S. 1989a Thermocapillary migration of a droplet with insoluble surfactant. *J. Colloid Interface Sci.* **127**, 417.

24. Kim, H.S. & Subramanian, R.S. 1989b The thermocapillary migration of a droplet with insoluble surfactant. *J. Colloid Interface Sci.* **130**, 112.

25. Ladyzhenskaya, O.A. 1963 *The mathematical theory of viscous incompressible flow.* Gordon & Breach.

26. Leichtberg, S., Pfeffer, R . & Weinbaum, S. 1976 Stokes flow past finite coaxil clusters of spheres in a circular cylinder. *Int. J. Multiphase Flow.* **3.** 147.

27. Lighthill, M. J. 1958 An introduction to Fourier analysis and generalized functions. Cambridge University Press.

28. Martinez, M.J. & Udell, K.S. 1989 Boundary integral analysis of the creeping flow of long bubbles in capillaries. TRANS. ASME E: *J. Appl. Mech.* **56**, 211.

29. Martinez, M.J. & Udell, K.S. 1990 Axisymmetric creeping motion of drops through circular tubes. *J. Fluid Mech.* **210**, 565.

30. Meyyappan, M. & Subramanian, R.S. 1984 Thermocapillary migration of two bubbles oriented arbitrary relative to a thermal gradient. *J. Colloid and Interface Sci.* **97**, *291.*

31. Meyyappan, M. & Subramanian, R.S. 1987 Thermocapillary migration of a gas bubble in an arbitrary direction with respect to a plane surface. *J. Colloid and Interface Sci.* **115**, 206.

32. Meyyappan, M., Wilcox, W.R. & Subramanian. R.S. 1981 Thermocapillary migration of a bubble normal to a plane surface. *J. Colloid Interface Sci.* **83**, 199.

33. Meyyappan, M., Wilcox, W.R. & Subramanian, R.S. 1983 The slow axisymmetric motion of two bubbles in a thermal gradient. *J. Colloid Interface Sci.* **94**, 243.

34. Morton, D.S., Subramanian, R.S. & Balasubramaniam, R. 1990 The migration of a compound drop due to thermocapillacity. *Phys. Fluids* **2**, 2119.

35. Nadim, A. & Borhan, A. 1989 The effects of surfactant on the motion and deformation of a droplet in thermocapillary migration. *PhysicoChem. Hydrodynamics* **11**, 753.

36. Pozrikidis, C. 1992 The buoyancy-driven motion of a train of viscous drops within a cylindrical tube. *J. Fluid Mech.* **237**, 627.

37. Reinelt, D. & Saffman, P. 1985 The penetration of a finger into a viscous liquid in a channel and tube. SIAM *J. Sci. Statist. Comput.* **6**, 542.

38. Reinelt, D. A. 1987 The rate at which a long bubble rises in a vertical tube. *J. Fluid Mech.* **175**, 557.

39. Satrape,J.V. 1992 Interactions and collisions of bubbles in thermocapillary bubble motion. *Phys. Fluids A.* **4**,1883.

40. Shankar, N., Cole, R. and Subramanian, R.S. 1981 Thermocapillary migration of a fluid droplet inside a drop in space laboratory. *Int. J. Multiphase Flow* **7**, 581.

41. Shankar, N. & Subramanian, R. S. 1983 The slow axisymmetric thermocapillary migration of an eccentrically placed bubble inside a drop in zero gravity. *J. Colloid and Interface Sci.* **94**, 258.

42. Shankar, N. & Subramanian, R.S. 1988 The Stokes motion of a gas bubble due to interfacial tension gradients at low to moderate Marangoni numbers. *J. Colloid Interface Sci.* **123**, 512.

43. Shen, E.I. & Udell, K.S. 1985 A finite element study of low Reynolds number two-phase flow in cylindrical tubes. TRANS. ASME E: *J. Appl. Mech.* **52**, 253.

44. Subramanian, R.S. 1981 Slow migration of a gas bubble in a thermal gradient. *AIChE Journal* **27**, 646.

45. Subramanian, R.S. 1983 Thermocapillary migration of bubbles and droplets. *Adv. Space Res.* **3**, No. 5, 145.

46. Thompson, R.L., DeWitt, K.J. & Labus, T.L. 1980 Marangoni bubble motion phenomenon in zero gravity. *Chem. Eng. Commun. 5,* 299.

47. Tözeren, A. & Skalak, R. 1977 Stress in a suspension near rigid boundaries. *J. Fluid Mech.* **82**, 289.

48. Tözeren, H. 1984 Boundary integral equation method for some Stokes flow problem. *Intl. J. Numer. Meth. Fluids.* **4**, 159.

49. Wang, H. & Skalak, R. 1969 Viscous flow in a cylindrical tube containing a line of spherical particles. *J. Fluid Mech.* **38**, 75.

50. Weinberg, M.C. 1978 Glass processing in space. *Glass Industry.* **59**, 22.

51. Wei, H & Subramanian, R.S. 1993 Thermocapillary migration of a small chain of bubbles. *Phys. Fluid A. 5*, No.7, 1583.

52. Westborg, H & Hassager, O. 1989 Creeping motion of long bubbles and drops in capillary tubes. *J. Colloid Interface Sci.* **133**, 135.

53. Youngren, G.K. & Acrivos, A. 1975 Stokes flow past a particle of arbitrary shape: a numerical method of solution. *J. Fluid Mech.* **69**,377.

54. Young, N.O., Goldstein, J.S. & Block, M.J. 1959 The motion of bubbles in a vertical temperature gradient. *J. Fluid Mech.* **6**, 350.